



## Characterization of the Microstructure and Photoelectrical Properties of TiO<sub>2</sub>-SrTiO<sub>3</sub> and TiO<sub>2</sub>-CeO<sub>2</sub> Nanocomposites

CHUN-HSIEN CHEN<sup>1</sup>, JAY SHIEH<sup>1,\*</sup> and JING-JONG SHYUE<sup>1,2</sup>

<sup>1</sup>Department of Materials Science and Engineering, National Taiwan University, 1 Roosevelt Road, Sec. 4, Taipei 106, Taiwan

<sup>2</sup>Research Center for Applied Sciences, Academia Sinica, 128 Academia Road, Sec. 2, Taipei 115, Taiwan

### KEYWORDS

titania  
strontium titanate  
ceria  
nanocomposites  
heterojunction  
photocatalysis

### ABSTRACT

The microstructure, optical absorption and photocurrent response of TiO<sub>2</sub>-SrTiO<sub>3</sub> and TiO<sub>2</sub>-CeO<sub>2</sub> nanostructured composites based on the design of coating the surfaces of anodized TiO<sub>2</sub> nanotube arrays with large band gap SrTiO<sub>3</sub> or small band gap CeO<sub>2</sub> nanoparticles have been investigated in this study. The nanocomposites were fabricated by a combination of anodization, hydrothermal and post-annealing methods. The UV-visible and ultraviolet photoelectron spectra of the structural components were measured in order to determine the electronic band structures of the TiO<sub>2</sub>-SrTiO<sub>3</sub> and TiO<sub>2</sub>-CeO<sub>2</sub> heterojunctions. These heterojunctions are designed to promote the separation of photoinduced charge carriers when the nanocomposites are adopted in photocatalytic or photoelectrode applications. The TiO<sub>2</sub>-SrTiO<sub>3</sub> and TiO<sub>2</sub>-CeO<sub>2</sub> heterojunctions were confirmed to possess large conduction and valence band offsets, promoting the separation of photoinduced electron and hole (e<sup>-</sup>/h<sup>+</sup>) pairs. The photocurrent densities of the TiO<sub>2</sub>-SrTiO<sub>3</sub> and TiO<sub>2</sub>-CeO<sub>2</sub> nanocomposites were about 15–40% larger than that of the anatase TiO<sub>2</sub> nanotube arrays. The size and crystallinity of the SrTiO<sub>3</sub> and CeO<sub>2</sub> nanoparticles, which could be controlled by the hydrothermal and annealing conditions, and the concentration of oxygen vacancies within the TiO<sub>2</sub> nanotube arrays were identified to be the key factors influencing the photocurrent response of the nanocomposites.

© 2014 DEStech Publications, Inc. All rights reserved.

### 1. INTRODUCTION

For solar energy applications, photocatalytic decomposition of molecules (e.g. water splitting and pollutant breakdown) is one of the main topics of interest and research. In photocatalytic water splitting, how to choose suitable semiconductor materials for photoelectrode applications is undoubtedly the most critical issue [1,2]. Since splitting of water into H<sub>2</sub> and O<sub>2</sub> on titania (TiO<sub>2</sub>) photoelectrode was demonstrated by Fujishima and Honda in the early 1970s [3], there have been many studies focusing on improving the photocatalytic properties of TiO<sub>2</sub> [4–7]. However, there are some difficulties in TiO<sub>2</sub> photocatalysis under solar irradiation, such as high recombination rate of photoinduced elec-

tron and hole (e<sup>-</sup>/h<sup>+</sup>) pairs and low absorption in the visible range. In order to improve the separation of photoinduced charge carriers, TiO<sub>2</sub>-based photocatalytic composites consisting of materials of different semiconducting properties, for example, different band gaps for absorbing light of different wavelengths, have been developed for their superior photocatalytic properties [8–10]. When TiO<sub>2</sub> and another semiconductor material are combined into a composite heterostructure, electronic band offsets at the material interface (i.e. heterojunction) are expected to exist. The band offsets created could be utilized to promote the separation of photoinduced e<sup>-</sup>/h<sup>+</sup> pairs, improving the efficiency of photocatalysis [11,12].

TiO<sub>2</sub> and strontium titanate (SrTiO<sub>3</sub>) are photocatalytic materials suitable for photoanode applications due to their strong oxidizing activity and high chemical stability. Anatase and rutile are the two major crystalline phases of TiO<sub>2</sub>

\*Corresponding author. Email: [jayshieh@ntu.edu.tw](mailto:jayshieh@ntu.edu.tw)

and possess band gaps of about 3.2 and 3.0 eV, respectively. Anatase TiO<sub>2</sub> is considered to deliver better photocatalytic performance due to its indirect band gap, smaller electron effective mass, higher mobility of charge carriers, and lower recombination rate of photoinduced e<sup>-</sup>/h<sup>+</sup> pairs [13]. SrTiO<sub>3</sub> on the other hand is of a perovskite structure and exhibits a more negative conduction band (CB) bottom edge and a stronger H<sub>2</sub> reducing power than TiO<sub>2</sub> [14]. Besides TiO<sub>2</sub> and SrTiO<sub>3</sub>, ceria (CeO<sub>2</sub>) is also a photocatalytic material receiving a large amount of interest. CeO<sub>2</sub> is a technologically important oxide material due to its wide applications in fields such as catalyst and catalyst support [15] and electrolyte or anode material in solid oxide fuel cells [16,17]. Nanocrystalline CeO<sub>2</sub> in particular has attracted much attention in photocatalysis research because of its small band gap of approximately 2.5–2.8 eV [18,19].

Aligned arrays of long TiO<sub>2</sub> nanotubes are often considered to be the optimal structure for solar energy conversion due to their high specific surface areas and continuous conduction pathways [6,7]. TiO<sub>2</sub> nanotube arrays can be fabricated by electrochemical anodization of titanium (Ti) in a fluoride-containing electrolyte—a simple process that requires no vacuum or high-temperature processing. In this study, anodized TiO<sub>2</sub> nanotube arrays and SrTiO<sub>3</sub> or CeO<sub>2</sub> nanoparticles were combined to form nanocomposites with favorable semiconductor heterojunctions for photocurrent enhancement. The nanocomposites were fabricated by a combination of anodization, hydrothermal and post-annealing methods. Our main goal was to investigate the optical absorption and photocurrent response of the nanocomposites under irradiation with different wavelength ranges. Changes in the crystalline phase, microstructure and electronic band structure of the nanocomposites with different processing conditions were characterized and related to the measured photoelectrical properties. These tasks were achieved through the interpretation of characterization data from a variety of techniques, including X-ray diffractometry, scanning and transmission electron microscopies, X-ray and ultraviolet photoelectron spectroscopies, optical spectrophotometry and photocurrent analysis in a photoelectrochemical cell (PEC).

## 2. EXPERIMENTAL PROCEDURE

### 2.1. Synthesis of TiO<sub>2</sub> Nanotube Arrays

Anodization of Ti foils in a standard two-electrode electrochemical cell was adopted to produce TiO<sub>2</sub> nanotube arrays, which served as the “scaffold” for the assembly of TiO<sub>2</sub>-SrTiO<sub>3</sub> and TiO<sub>2</sub>-CeO<sub>2</sub> nanocomposites. Ti foils of 0.1 mm thickness (Type 2N8, UMAT, Taiwan) were cleaned in an ultrasonic bath with acetone and isopropyl alcohol. Ethylene glycol (C<sub>2</sub>H<sub>6</sub>O<sub>2</sub>, purity 99% plus, Acros Organics, USA) containing 0.3 wt% ammonium fluoride (NH<sub>4</sub>F, purity 98%

plus, Acros Organics, USA) and 5 vol% deionized water was used as the anodizing electrolyte. Anodization was carried out by applying a constant 20 V potential between the Ti foil (anode) and a platinum electrode (cathode) for 2 h. After anodization, the amorphous TiO<sub>2</sub> nanotube arrays produced were cleaned and then annealed at 450°C in air for 3 h with an initial heating rate of 5°C min<sup>-1</sup> to crystallize into the anatase phase. The microstructure, crystalline phase, optical absorption and photocurrent response of the anatase TiO<sub>2</sub> nanotube arrays were described in our previous study [20]. Note that for comparison purposes, a different set of anodized TiO<sub>2</sub> nanotube array samples were annealed at a different condition—450°C in pure O<sub>2</sub> for 6 h. The concentration of oxygen vacancies within the TiO<sub>2</sub> nanotube arrays could be adjusted by changing the annealing atmosphere. This approach was designed to study the effect of oxygen vacancies on the electronic band structure and photoelectrical properties of the nanocomposites.

### 2.2. Synthesis of TiO<sub>2</sub>-SrTiO<sub>3</sub> and TiO<sub>2</sub>-CeO<sub>2</sub> Nanocomposites

TiO<sub>2</sub>-SrTiO<sub>3</sub> nanostructured composites were fabricated by hydrothermally-treating the 450°C-annealed anatase TiO<sub>2</sub> nanotube arrays in an autoclave containing a 0.05 M Sr(OH)<sub>2</sub> aqueous solution. The hydrothermal reaction was carried out at 160°C for 0.5–2.0 h with a heating rate of 5°C min<sup>-1</sup>. After the hydrothermal process, the surfaces of the TiO<sub>2</sub> nanotube arrays were coated with crystalline SrTiO<sub>3</sub> nanoparticles in the finishing structure. The size of the SrTiO<sub>3</sub> nanoparticles was controlled by the hydrothermal treatment time.

TiO<sub>2</sub>-CeO<sub>2</sub> nanostructured composites were fabricated by hydrothermally-treating the 450°C-annealed anatase TiO<sub>2</sub> nanotube arrays in an autoclave containing a 0.02 M precursor solution of ammonium cerium nitrate ((NH<sub>4</sub>)<sub>2</sub>Ce(NO<sub>3</sub>)<sub>6</sub>, purity 98.5% plus, Sigma-Aldrich, USA) and ammonium hydroxide (NH<sub>4</sub>OH, purity 98.5% plus, Sigma-Aldrich, USA), mixed in deionized water with a molar ratio of 1:2, respectively. The hydrothermal synthesis and deposition of CeO<sub>2</sub> nanoparticles on the surfaces of the TiO<sub>2</sub> nanotube arrays was carried out at 140°C for 3 h. After the hydrothermal process, TiO<sub>2</sub>-CeO<sub>2</sub> nanocomposites were washed with deionized water and then annealed in air for 3 h at one of two temperatures—450 and 550°C—with an initial heating rate of 5°C min<sup>-1</sup>. The lengthy annealing procedure was to fully crystallize the CeO<sub>2</sub> nanoparticles and promote their growth in the TiO<sub>2</sub> nanotube scaffold.

### 2.3. Characterization of Key Properties

The surface morphology and cross-sectional microstructure of the nanostructured samples were examined by field-emission scanning electron microscopy (FE-SEM; Model

1530, LEO, Germany & NOVA NanoSEM 450, FEI, USA). The crystalline phases of the samples were confirmed by X-ray diffraction (XRD; Model X'Pert PRO, PANalytical, The Netherlands). Elemental analysis of the samples was achieved by X-ray photoelectron spectroscopy (XPS; Model PHI 5000 VersaProbe, ULVAC-PHI, Japan) utilizing micro-focused Al  $K\alpha$  X-rays (25 W, 100  $\mu\text{m}$ ), with a photoelectron take-off angle of  $45^\circ$ . The absorption and reflectance spectra of the samples were obtained using an ultraviolet-visible spectrophotometer (UV-Vis; Model V-550, Jasco, USA) with a wavelength range of 200 to 800 nm. For each material component in the nanocomposites, the energy difference between the Fermi level and the valence band (VB) top edge was determined by ultraviolet photoelectron spectroscopy (UPS; Model PHI 5000 VersaProbe, ULVAC-PHI, Japan) using He I ultraviolet radiation (21.2 eV, 50 W), with a photoelectron take-off angle of  $90^\circ$  and an energy resolution of 0.013 eV. Silver metallic foil was routinely analyzed for Fermi level calibration. The photocurrent densities of the nanostructured samples under irradiation with different wavelength ranges were measured using a potentiostatic three-electrode electrochemical cell (Model SP-150, BioLogic, France), with the sample, a platinum foil and a saturated calomel electrode (SCE; Cole-Parmer, USA) employed as the working (photoanode), counter and reference electrodes, respectively. 1 M KOH was used as the electrolyte in the electrochemical cell. The outputs from a 100 W Hg lamp and a 100 W Xe lamp were coupled to optical fibers (1  $\text{cm}^2$  irradiation area) and used respectively as the unfiltered UV and white light sources for photocurrent measurements. The white light source was filtered by a short-pass filter when irradiation of a specific wavelength range was needed.

### 3. RESULTS AND DISCUSSION

#### 3.1. $\text{TiO}_2\text{-SrTiO}_3$ Nanocomposites

The XRD patterns of the  $450^\circ\text{C}$ -annealed  $\text{TiO}_2$  nanotube arrays (serving as the scaffold for composite assembly) and  $\text{TiO}_2\text{-SrTiO}_3$  nanocomposites prepared with different hydrothermal treatment time (0.5, 1 and 2 h) are shown in Figure 1. The anatase and perovskite phases of the  $\text{TiO}_2$  nanotube arrays and  $\text{SrTiO}_3$  nanoparticles are confirmed, respectively. The (110) peak of perovskite  $\text{SrTiO}_3$  increases with increasing hydrothermal treatment time, suggesting the growth and enhanced crystallization of the  $\text{SrTiO}_3$  nanoparticles. In contrast, the (101) peak of anatase  $\text{TiO}_2$  decreases with increasing hydrothermal time, indicating the decomposition of  $\text{TiO}_2$  in order to form  $\text{SrTiO}_3$  (i.e. Ti in  $\text{SrTiO}_3$  came from  $\text{TiO}_2$ ). The cross-sectional and surface SEM micrographs of the anatase  $\text{TiO}_2$  nanotube arrays and  $\text{TiO}_2\text{-SrTiO}_3$  nanocomposites are shown in Figure 2. It is evident that the architecture of the nanocomposites is based on coating the surfaces of the

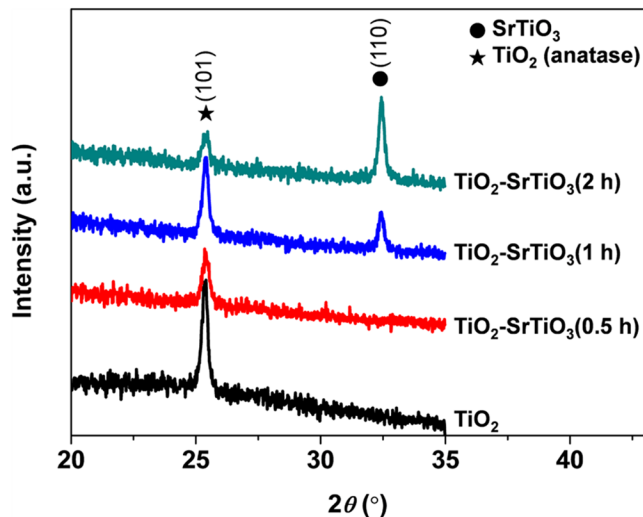


**Figure 1.** XRD patterns of anatase  $\text{TiO}_2$  nanotube arrays and  $\text{TiO}_2\text{-SrTiO}_3$  nanocomposites prepared with different hydrothermal treatment time (0.5, 1 and 2 h).

$\text{TiO}_2$  nanotube arrays with  $\text{SrTiO}_3$  nanoparticles. The  $\text{SrTiO}_3$  nanoparticles nucleate and grow on defect sites on the  $\text{TiO}_2$  nanotube surfaces and the nanoparticle growth process continues as the hydrothermal treatment is extended [8]. Figure 2 shows that the amount and size of the  $\text{SrTiO}_3$  nanoparticles on the  $\text{TiO}_2$  nanotube surfaces increase with increasing hydrothermal treatment time. The microstructure evolution observed from the SEM micrographs correlates well with the XRD data.

In order to construct the electronic band structure of the  $\text{TiO}_2\text{-SrTiO}_3$  heterojunction, crystalline  $\text{SrTiO}_3$  nanoparticles were synthesized separately by the hydrothermal method and had their optical properties characterized. The UV-Vis absorption spectra of the anatase  $\text{TiO}_2$  nanotube arrays and  $\text{SrTiO}_3$  nanoparticles are shown in Figure 3(a). The  $\text{TiO}_2$  nanotube arrays exhibit a certain extent of visible light absorption, as indicated by the rising tail of its absorption curve in the long-wavelength range. This is due to the presence of oxygen vacancies within the  $\text{TiO}_2$  nanotubes [20], introduced during the anodization phase of the synthesis using an electrolyte low in  $\text{H}_2\text{O}$  content (i.e. ethylene glycol-based solution; see Section 2.1). Based on the UV-Vis absorption and reflectance spectra of the  $\text{TiO}_2$  nanotube arrays and  $\text{SrTiO}_3$  nanoparticles, the band gaps of these two components in the nanocomposites were determined to be 3.33 and 3.12 eV, respectively, by adopting the Kubelka-Munk function and Tauc relation [21,22]. Additionally, the energy differences between the Fermi level and the VB top edge for the  $\text{TiO}_2$  nanotube arrays and  $\text{SrTiO}_3$  nanoparticles were determined by UPS to be 3.12 and 1.92 eV, respectively.

In this study, alignment of the Fermi levels of  $\text{TiO}_2$  and  $\text{SrTiO}_3$  at the material interface is assumed without considering the possible band bending at the interface. Based on such assumption and the measured UV-Vis and UPS data, the ap-

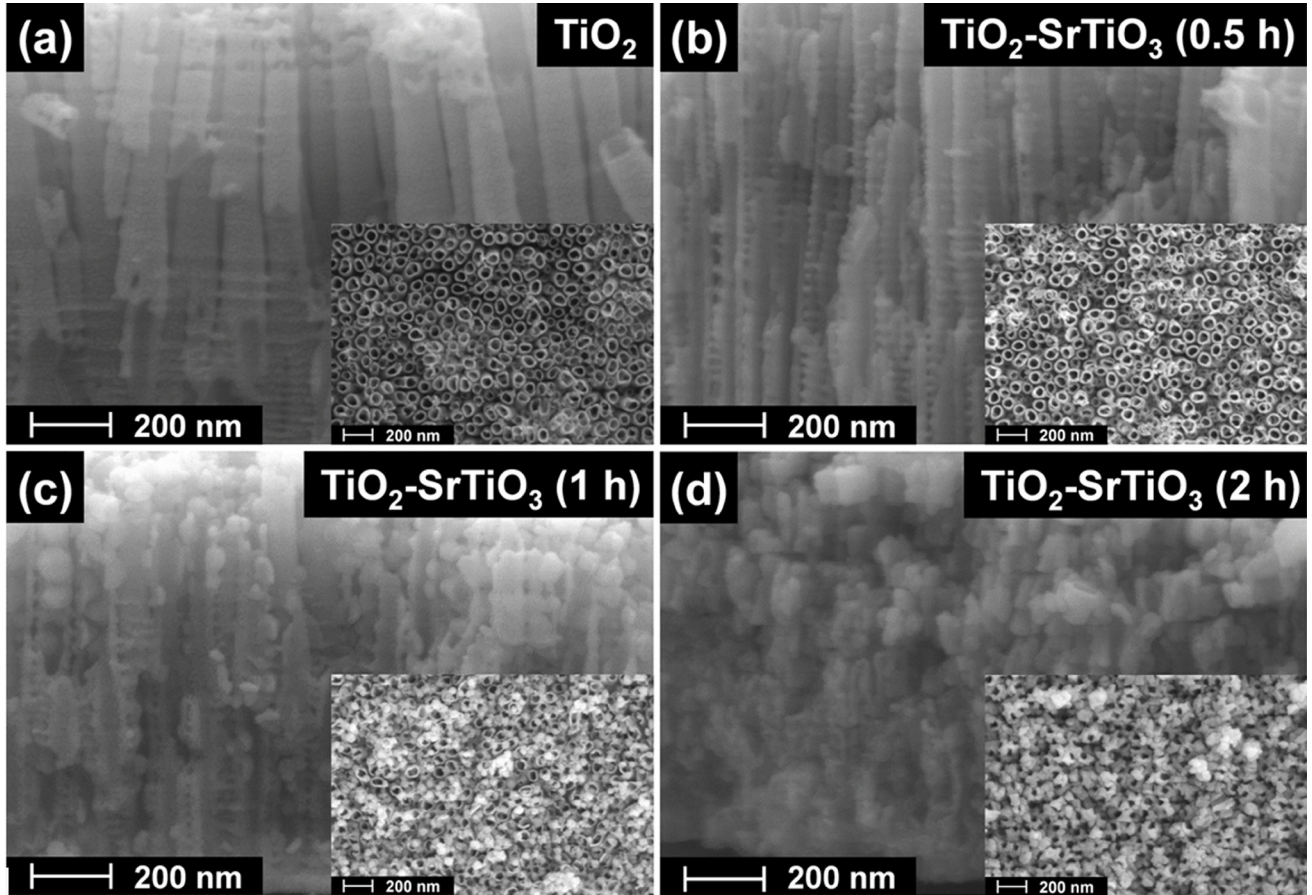


**Figure 2.** Cross-sectional and surface (insert) SEM micrographs of (a) anatase  $\text{TiO}_2$  nanotube arrays and (b)–(d)  $\text{TiO}_2$ - $\text{SrTiO}_3$  nanocomposites prepared with hydrothermal time of (b) 0.5, (c) 1 and (d) 2 h.

the approximate electronic band structure of the  $\text{TiO}_2$ - $\text{SrTiO}_3$  heterojunction can be constructed and is shown in Figure 3(b). Note that since the work functions of the  $\text{TiO}_2$  nanotube arrays and  $\text{SrTiO}_3$  nanoparticles were not characterized, the exact energy positions of the band edges were unable to be determined. Figure 3(b) shows that the  $\text{TiO}_2$ - $\text{SrTiO}_3$  heterojunction possesses a CB offset of about 1.0 eV, promoting the transfer of photoinduced electrons from the CB of  $\text{SrTiO}_3$  nanoparticles to the CB of  $\text{TiO}_2$  nanotube arrays. In contrast, the transfer of photoinduced holes from the VB of  $\text{TiO}_2$  nanotube arrays to the VB of  $\text{SrTiO}_3$  nanoparticles is promoted by the VB offset (1.2 eV) at the heterojunction. It is evident that forming the  $\text{TiO}_2$ - $\text{SrTiO}_3$  heterojunction is an effective approach to promote the separation of photoinduced  $e^-/h^+$  pairs and likely to increase the photocatalytic efficiency of  $\text{TiO}_2$ -based photoelectrodes.

The photocurrent densities of the anatase  $\text{TiO}_2$  nanotube arrays and  $\text{TiO}_2$ - $\text{SrTiO}_3$  nanocomposites measured under on-off UV irradiation cycles are shown in Figure 4. The photocurrent densities of the  $\text{TiO}_2$ - $\text{SrTiO}_3$  nanocomposites prepared with hydrothermal time of 0.5 and 1 h are about 15–25% larger than that of the  $\text{TiO}_2$  nanotube arrays. This sizable photocurrent enhancement is due to the  $\text{TiO}_2$ - $\text{SrTiO}_3$

heterojunction present in the composite heterostructure, promoting the separation of photoinduced  $e^-/h^+$  pairs. However, when the hydrothermal time was extended to 2 h, a large amount of larger  $\text{SrTiO}_3$  nanoparticles were produced on the  $\text{TiO}_2$  nanotube array surfaces, resulting in the increased number of heterogeneous grain boundaries. These structural interfaces (defects) would trap the photoinduced charge carriers and consequently hinder their transportations, resulting in a substantial decrease in photocurrent performance (see Figure 4). This study has found that it is critical to construct the  $\text{TiO}_2$ - $\text{SrTiO}_3$  nanocomposites using a  $\text{TiO}_2$  nanotube scaffold with a high concentration of oxygen vacancies. The oxygen vacancies can increase the visible light absorption [20], provide nucleation sites for the  $\text{SrTiO}_3$  nanoparticles, and most importantly, create a heterojunction with large band offsets. The last point is further discussed in the next section.

### 3.2. Effect of Oxygen Vacancies on Heterojunction Band Structure

The size of the band offsets associated with the  $\text{TiO}_2$ - $\text{SrTiO}_3$  heterojunction has been found to be dependent on

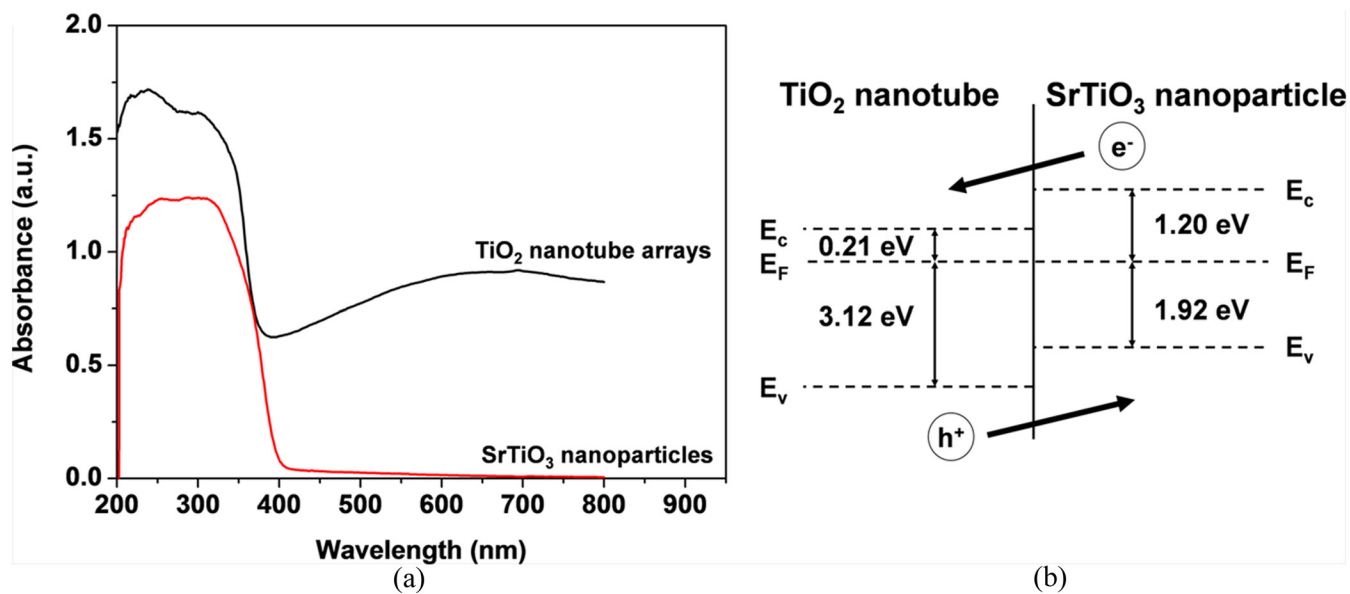


**Figure 3.** (a) UV-Vis absorption spectra of anatase  $\text{TiO}_2$  nanotube arrays and  $\text{SrTiO}_3$  nanoparticles. (b) Approximate electronic band structure of  $\text{TiO}_2\text{-SrTiO}_3$  heterojunction, indicating conduction and valence band offsets.

the concentration of oxygen vacancies in the  $\text{TiO}_2$  nanotube arrays. In this study, another set of  $\text{TiO}_2\text{-SrTiO}_3$  nanocomposites were constructed using the  $\text{TiO}_2$  nanotube arrays annealed in pure  $\text{O}_2$  for 6 h. Compared to the nanotube arrays annealed in air for 3 h, the  $\text{O}_2$ -annealed ones would contain a lower concentration of oxygen vacancies. The different annealing atmospheres were setup to study the effect of oxygen vacancies on the Fermi level and band structure of the  $\text{TiO}_2\text{-SrTiO}_3$  heterojunction. The UV-Vis absorption spectra of the  $\text{TiO}_2$  nanotube arrays annealed in air and in  $\text{O}_2$  are shown in Figure 5(a). A significant decrease in the visible light absorption is observed for the  $\text{O}_2$ -annealed  $\text{TiO}_2$  nanotube arrays (i.e. a less raised absorption curve tail), indicating a much

lower concentration of oxygen vacancies. Based on the UV-Vis and UPS data measured for the  $\text{O}_2$ -annealed  $\text{TiO}_2$  nanotube arrays and  $\text{SrTiO}_3$  nanoparticles, the approximate electronic band structure of the  $\text{TiO}_2\text{-SrTiO}_3$  heterojunction can be constructed and is shown in Figure 5(b). Upon comparing Figures 3(b) and 5(b), it is evident that when the concentration of oxygen vacancies in the  $\text{TiO}_2$  nanotube scaffold is reduced, the Fermi level of  $\text{TiO}_2$  is lowered (i.e. less n-type), resulting in the decreased size of the CB and VB offsets from about 1.0 to 0.77 eV and 1.2 to 0.83 eV, respectively. Such changes in the band structure of the  $\text{TiO}_2\text{-SrTiO}_3$  heterojunction would certainly have a strong impact on the photocurrent response.

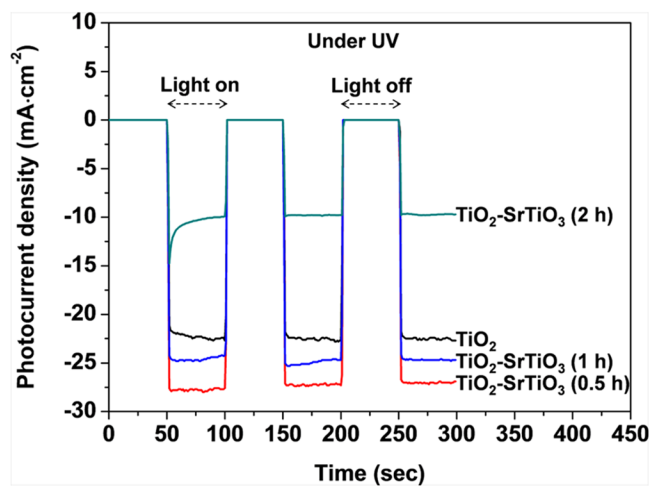


**Figure 4.** Photocurrent densities measured under on-off UV irradiation cycles for anatase  $\text{TiO}_2$  nanotube arrays and  $\text{TiO}_2\text{-SrTiO}_3$  nanocomposites prepared with different hydrothermal time.

The photocurrent densities of the  $\text{TiO}_2\text{-SrTiO}_3$  nanocomposites prepared with a hydrothermal time of 0.5 h and using  $\text{TiO}_2$  nanotube scaffolds annealed at different atmospheres (i.e. air for 3 h and  $\text{O}_2$  for 6 h) are shown in Figure 5(c). The photocurrent density of the nanocomposite using the  $\text{O}_2$ -annealed  $\text{TiO}_2$  nanotube scaffold is about 40% smaller than that of the one using the air-annealed  $\text{TiO}_2$  nanotube scaffold. Such a large difference demonstrates that the size of the band offsets associated with the heterojunction is a critical factor governing the photocurrent response of the nanocomposite. The reduced band offsets, caused by the decreased concentration of oxygen vacancies, would be less effective in charge carrier separation, resulting in the decrease of photocurrent density. It should be noted that fewer oxygen vacancies would also mean the reduction of active sites for photocatalytic reactions and nucleation sites for  $\text{SrTiO}_3$  nanoparticles. These factors also have an influence on the photocurrent response and will be investigated in future studies.

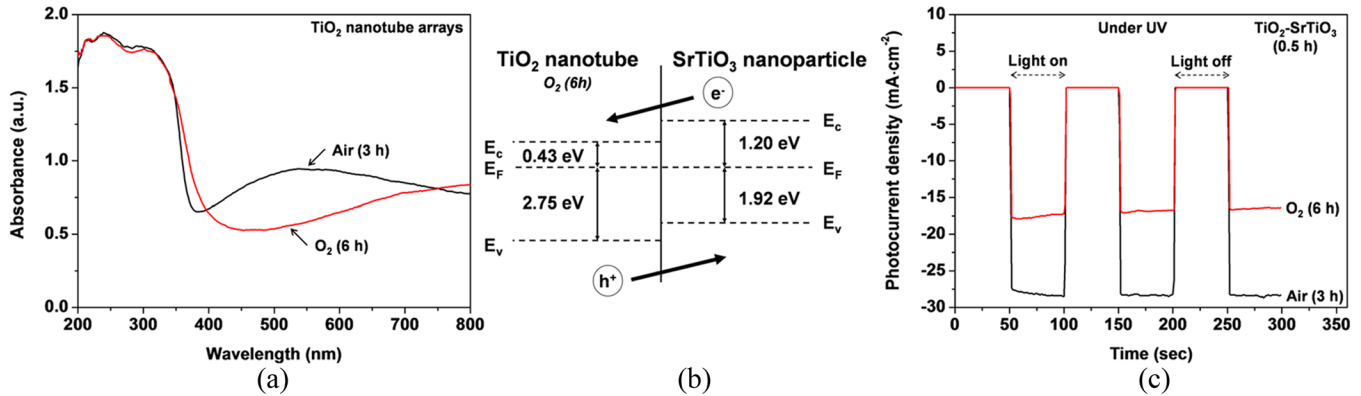


**Figure 5.** (a) UV-Vis absorption spectra of  $\text{TiO}_2$  nanotube arrays annealed at  $450^\circ\text{C}$  in air for 3 h and in  $\text{O}_2$  for 6 h. (b) Approximate electronic band structure of  $\text{TiO}_2$ - $\text{SrTiO}_3$  heterojunction, formed using  $\text{O}_2$ -annealed  $\text{TiO}_2$  nanotube arrays. (c) Photocurrent densities measured under on-off UV irradiation cycles for  $\text{TiO}_2$ - $\text{SrTiO}_3$  nanocomposites using  $\text{TiO}_2$  nanotube scaffolds annealed in air and in  $\text{O}_2$ .

### 3.3. $\text{TiO}_2$ - $\text{CeO}_2$ nanocomposites

Figure 6 shows the cross-sectional and surface SEM micrographs of the  $\text{TiO}_2$ - $\text{CeO}_2$  nanocomposites annealed at  $450^\circ\text{C}$  and  $550^\circ\text{C}$ , revealing that the outer and topmost surfaces of the  $\text{TiO}_2$  nanotube arrays are coated with  $\text{CeO}_2$  nanoparticles, with the number of the nanoparticles increasing with increasing annealing temperature. Figure 7(a) shows the  $\text{Ce}3d$  XPS spectra of the annealed  $\text{TiO}_2$ - $\text{CeO}_2$  nanocomposites. The spectra exhibit the main signals of

$\text{Ce}^{4+}3d$  ( $\text{Ce}^{4+}3d_{5/2}$ , 882 eV;  $\text{Ce}^{4+}3d_{3/2}$ , 901 eV), confirming that  $\text{CeO}_2$  nanoparticles were successfully synthesized by the hydrothermal reaction. The signals of  $\text{Ce}^{3+}3d$  ( $\text{Ce}^{3+}3d_{5/2}$ , 886 eV;  $\text{Ce}^{3+}3d_{3/2}$ , 905 eV) were also detected by XPS. The formation of  $\text{Ce}^{3+}$  ions (i.e.  $\text{Ce}_2\text{O}_3$ ) is believed to be caused by the oxygen deficiency in  $\text{CeO}_2$  nanocrystallites [23,24]. Figure 7(b) shows the UV-Vis absorption spectra of the annealed  $\text{TiO}_2$ - $\text{CeO}_2$  nanocomposites. The large red-shift in the absorption edge with increasing annealing temperature from  $450$  to  $550^\circ\text{C}$  is due to the increased presence and growth of

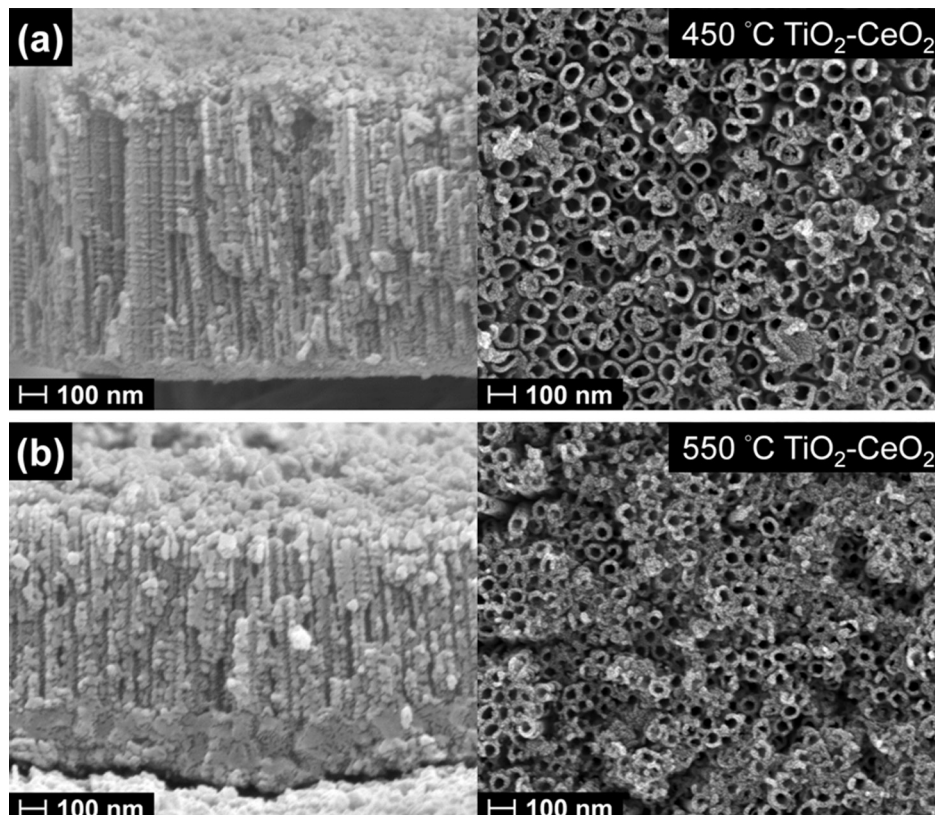


**Figure 6.** Cross-sectional (left) and surface (right) SEM micrographs of  $\text{TiO}_2$ - $\text{CeO}_2$  nanocomposites annealed at (a)  $450^\circ\text{C}$  and (b)  $550^\circ\text{C}$ .

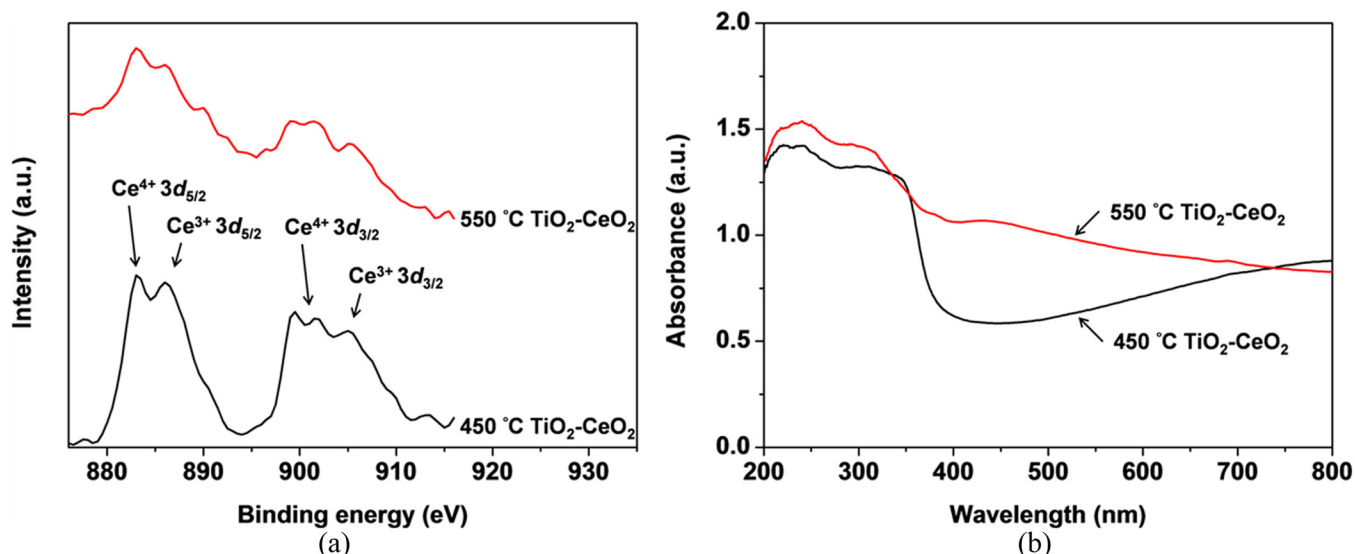


Figure 7. (a) Ce3d XPS and (b) UV-Vis absorption spectra of  $\text{TiO}_2\text{-CeO}_2$  nanocomposites annealed at 450°C and 550°C.

$\text{CeO}_2$  nanoparticles and the likely effect of carbon substitutional doping, i.e. substitution of  $\text{C}^{4-}$  for  $\text{O}^{2-}$  in  $\text{TiO}_2$  [25,26]. Carbon dopants were most likely to come from the residues of ethylene glycol, the electrolyte used in the anodization phase of the synthesis. The residues (carbon-based species) adsorbed on the  $\text{TiO}_2$  nanotube surfaces dissociated during annealing at 550°C [27,28], resulting in the doping of the nanotubes with  $\text{C}^{4-}$ . In comparison, carbon doping was much less effective at 450°C due to incomplete dissociation of the electrolyte residues and slow diffusion of  $\text{C}^{4-}$  in  $\text{TiO}_2$  at this low temperature.

In order to construct the electronic band structure of the  $\text{TiO}_2\text{-CeO}_2$  heterojunction, crystalline  $\text{CeO}_2$  nanoparticles

were synthesized separately by the hydrothermal method and had their optical properties characterized. The UV-Vis absorption spectra of the anatase  $\text{TiO}_2$  nanotube arrays (annealed in air) and  $\text{CeO}_2$  nanoparticles are shown in Figure 8(a). It is evident that the band gap of the  $\text{CeO}_2$  nanoparticles is much smaller than that of the  $\text{TiO}_2$  nanotube arrays. The incorporation of small band gap  $\text{CeO}_2$  nanoparticles in the composite heterostructure would significantly increase the visible light absorption. Based on the UV-Vis and UPS data of the  $\text{TiO}_2$  nanotube arrays (annealed in air) and  $\text{CeO}_2$  nanoparticles, the band gaps of these two components in the nanocomposites were determined to be 3.33 and 2.55 eV, respectively; while, the energy differences between the Fermi

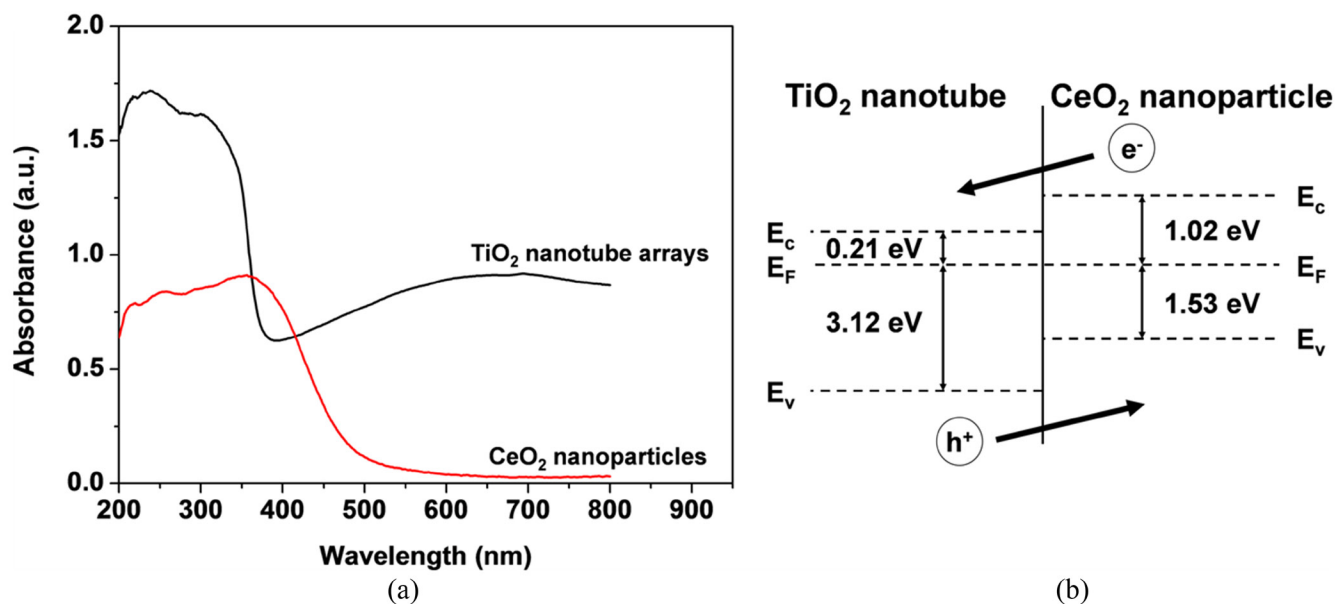
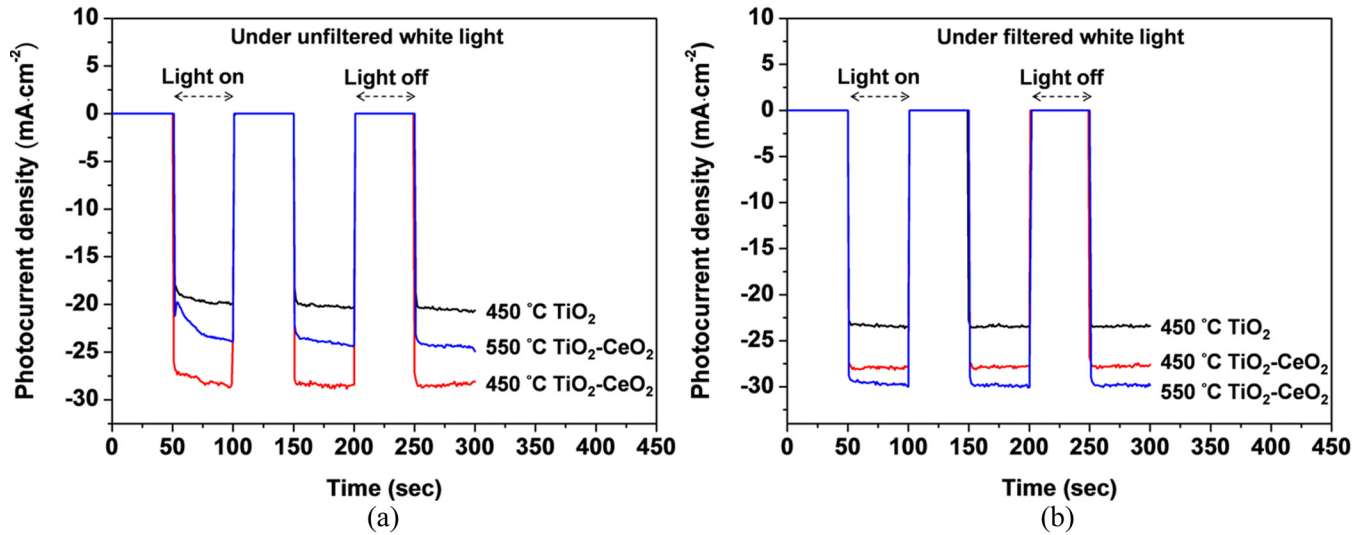


Figure 8. (a) UV-Vis absorption spectra of anatase  $\text{TiO}_2$  nanotube arrays and  $\text{CeO}_2$  nanoparticles. (b) Approximate electronic band structure of  $\text{TiO}_2\text{-CeO}_2$  heterojunction, indicating conduction and valence band offsets.



**Figure 9.** Photocurrent densities measured under on-off (a) unfiltered and (b) filtered white light irradiation cycles for anatase  $\text{TiO}_2$  nanotube arrays and  $\text{TiO}_2\text{-CeO}_2$  nanocomposites annealed at different temperatures.

level and the VB top edge, 3.12 and 1.53 eV, respectively. The approximate electronic band structure of the  $\text{TiO}_2\text{-CeO}_2$  heterojunction can therefore be constructed and is shown in Figure 8(b). The  $\text{TiO}_2\text{-CeO}_2$  heterojunction possesses large CB and VB offsets of about 0.8 and 1.59 eV, respectively, promoting the separation of photoinduced  $e^-/h^+$  pairs.

Figure 9(a) shows the photocurrent densities of the 450 and 550°C-annealed  $\text{TiO}_2\text{-CeO}_2$  nanocomposites under on-off unfiltered white light irradiation cycles. The photocurrent densities of the nanocomposites are about 25–40% larger than that of the anatase  $\text{TiO}_2$  nanotube arrays [also shown in Figure 9(a)]. When the annealing temperature was increased to 550°C, carbon dopants were introduced into the nanocomposite, resulting in an increase in the number of ionic defects and the introduction of extra energy levels associated with  $C^{4-2p}$  in the  $\text{TiO}_2$  band structure. Although the extra energy levels associated with carbon doping gave rise to a significant red-shift in the absorption edge [see Figure 7(b)], the recombination and trapping of photoinduced charge carriers at the defect centers and  $C^{4-2p}$  energy levels would have a detrimental effect on the photocurrent response. This is the reason why the extent of photocurrent enhancement shown by the 550°C-annealed  $\text{TiO}_2\text{-CeO}_2$  nanocomposite is smaller than the 450°C-annealed one.

Figure 9(b) shows the photocurrent densities of the annealed  $\text{TiO}_2\text{-CeO}_2$  nanocomposites under on-off filtered white light irradiation cycles. The filtered white light used had almost zero irradiance at 400–500 nm and was achieved with a 400-nm short-pass fused silica filter. The wavelength region of 400–500 nm was almost completely blocked out upon filtering, while, light with wavelengths longer than 500 nm could still pass through. The filtering operation therefore effectively made the Xe-lamp light source to produce a combination of UV ( $\lambda < 400$  nm) and visible light ( $\lambda > 500$

nm) irradiation. Figure 9(b) shows that the 550°C-annealed  $\text{TiO}_2\text{-CeO}_2$  nanocomposite produces the largest photocurrent density under filtered white light. It is believed that most VB electrons were excited to the CB by the UV portion of the filtered light source and were able to contribute directly to the photocurrent density. In contrast, when the 550°C-annealed nanocomposite was irradiated with unfiltered white light, a portion of the VB electrons were excited to and eventually became trapped and/or recombined at the carbon-doping-induced defects and recombination centers and were unable to contribute to the photocurrent density. This is the reason why the photocurrent density of the 550°C-annealed  $\text{TiO}_2\text{-CeO}_2$  nanocomposite is larger under filtered than unfiltered white light irradiation [see Figure 9(a) and (b)].

Figure 9(b) shows that the photocurrent density of the 550°C-annealed  $\text{TiO}_2\text{-CeO}_2$  nanocomposite is larger than that of the 450°C-annealed one under filtered white light. Since the adverse effects associated with the trapping and recombination of photoinduced charge carriers were minimized under filtered white light, the benefits of having a higher amount of larger crystalline  $\text{CeO}_2$  nanoparticles in the  $\text{TiO}_2$  nanotube scaffold with 550°C annealing would result in a noticeable photocurrent enhancement. Note that the filtered white light source also contains a long-wavelength portion ( $\lambda > 500$  nm), which could be absorbed via the donor-type energy levels associated with the presence of oxygen vacancies and contribute to the photocurrent response of the  $\text{TiO}_2\text{-CeO}_2$  nanocomposites.

#### 4. CONCLUSION

$\text{TiO}_2$  nanotube arrays and  $\text{SrTiO}_3$  or  $\text{CeO}_2$  nanoparticles were combined to form nanocomposites for photocatalytic studies. The nanocomposites were fabricated by a combina-

tion of anodization, hydrothermal and post-annealing methods and were developed to demonstrate the effectiveness of the TiO<sub>2</sub>-SrTiO<sub>3</sub> and TiO<sub>2</sub>-CeO<sub>2</sub> semiconductor heterojunctions in enhancing the photocurrent response of TiO<sub>2</sub>-based photoelectrodes. UV-Vis and UPS analyses were performed to construct the electronic band structures of the TiO<sub>2</sub>-SrTiO<sub>3</sub> and TiO<sub>2</sub>-CeO<sub>2</sub> heterojunctions. The heterojunctions were confirmed to possess large CB and VB offsets promoting the separation of photoinduced e<sup>-</sup>/h<sup>+</sup> pairs. The photocurrent densities of the TiO<sub>2</sub>-SrTiO<sub>3</sub> and TiO<sub>2</sub>-CeO<sub>2</sub> nanocomposites were about 15–40% larger than that of the anatase TiO<sub>2</sub> nanotube arrays under identical irradiation conditions. The size and crystallinity of the SrTiO<sub>3</sub> and CeO<sub>2</sub> nanoparticles, which could be controlled by the hydrothermal and annealing conditions, and the concentration of oxygen vacancies within the TiO<sub>2</sub> nanotube arrays were identified to be the key factors influencing the photocurrent response of the nanocomposites. The nanoparticle-on-nanotube architecture of the TiO<sub>2</sub>-CeO<sub>2</sub> heterostructure has been shown to provide several advantages: a high specific surface area for photocatalytic reactions, a small band gap component capable of absorbing visible light, and a heterojunction effective in charge carrier separation.

## ACKNOWLEDGEMENTS

The authors are grateful for the financial support of the National Science Council (NSC) of Taiwan under contract numbers NSC100-2628-E-002-024-MY2 and NSC102-2221-E-002-059.

## REFERENCES

- [1] Kudo, A. and Miseki, Y., "Heterogeneous photocatalyst materials for water splitting," *Chem. Soc. Rev.* **38**, 253–278 (2009). <http://dx.doi.org/10.1039/b800489g>, PMID:19088977
- [2] Kudo, A., Kato, H. and Tsuji, I., "Strategies for the development of visible-light-driven photocatalysts for water splitting," *Chem. Lett.* **33**, 1534–1539 (2004). <http://dx.doi.org/10.1246/cl.2004.1534>
- [3] Fujishima, A. and Honda, K., "Electrochemical photolysis of water at a semiconductor electrode," *Nature* **238**, 37–38 (1972). <http://dx.doi.org/10.1038/238037a0>, PMID:12635268
- [4] Fujishima, A., Rao, T. N. and Tryk, D. A., "Titanium dioxide photocatalysis," *J. Photochem. Photobiol. C: Photochem. Rev.* **1**, 1–21 (2000). [http://dx.doi.org/10.1016/S1389-5567\(00\)00002-2](http://dx.doi.org/10.1016/S1389-5567(00)00002-2)
- [5] Anpo, M. and Takeuchi, M., "The design and development of highly reactive titanium oxide photocatalysts operating under visible light irradiation," *J. Catal.* **216**, 505–516 (2003). [http://dx.doi.org/10.1016/S0021-9517\(02\)00104-5](http://dx.doi.org/10.1016/S0021-9517(02)00104-5)
- [6] Mor, G. K., Varghese, O. K., Paulose, M., Shankar, K. and Grimes, C. A., "A review on highly ordered, vertically oriented TiO<sub>2</sub> nanotube arrays: fabrication, material properties, and solar energy applications," *Sol. Energy Mater. Sol. Cells* **90**, 2011–2075 (2006). <http://dx.doi.org/10.1016/j.solmat.2006.04.007>
- [7] Mor, G. K., Shankar, K., Paulose, M., Varghese, O. K. and Grimes, C. A., "Use of highly-ordered TiO<sub>2</sub> nanotube arrays in dye-sensitized solar cells," *Nano Lett.* **6**, 215–218 (2006). <http://dx.doi.org/10.1021/nl052099j>, PMID:16464037
- [8] Zhang, J., Bang, J. H., Tang, C. C. and Kamat, P. V., "Tailored TiO<sub>2</sub>-SrTiO<sub>3</sub> heterostructure nanotube arrays for improved photoelectrochemical performance," *ACS Nano* **4**, 387–395 (2010). <http://dx.doi.org/10.1021/nn901087c>, PMID:20000756
- [9] Bessekhoud, Y., Robert, D. and Weber, J. V., "Photocatalytic activity of Cu<sub>2</sub>O/TiO<sub>2</sub>, Bi<sub>2</sub>O<sub>3</sub>/TiO<sub>2</sub> and ZnMn<sub>2</sub>O<sub>4</sub>/TiO<sub>2</sub> heterojunctions," *Catal. Today* **101**, 315–321 (2005). <http://dx.doi.org/10.1016/j.cattod.2005.03.038>
- [10] Sun, W. T., Yu, Y., Pan, H. Y., Gao, X. F., Chen, Q. and Peng, L. M., "CdS quantum dots sensitized TiO<sub>2</sub> nanotube-array photoelectrodes," *J. Am. Chem. Soc.* **130**, 1124–1125 (2008). <http://dx.doi.org/10.1021/ja0777741>, PMID:18183979
- [11] Ni, M., Leung, M. K. H., Leung, D. Y. C. and Sumathy, K., "A review and recent developments in photocatalytic water-splitting using TiO<sub>2</sub> for hydrogen production," *Renew. Sustain. Energy Rev.* **11**, 401–425 (2007). <http://dx.doi.org/10.1016/j.rser.2005.01.009>
- [12] Burnside, S., Moser, J. E., Brooks, K., Gratzel, M. and Cahen, D., "Nanocrystalline mesoporous strontium titanate as photoelectrode material for photosensitized solar devices: Increasing photovoltage through flatband potential engineering," *J. Phys. Chem. B* **103**, 9328–9332 (1999). <http://dx.doi.org/10.1021/jp9913867>
- [13] Tang, H., Prasad, K., Sanjinès, R., Schmid, P. E. and Lévy, F., "Electrical and optical properties of TiO<sub>2</sub> anatase thin films," *J. Appl. Phys.* **75**, 2042–2047 (1994). <http://dx.doi.org/10.1063/1.356306>
- [14] Bolts, J. M. and Wrighton, M. S., "Correlation of photocurrent-voltage curves with flat-band potential for stable photoelectrodes for the photoelectrolysis of water," *J. Phys. Chem.* **80**, 2641–2645 (1976). <http://dx.doi.org/10.1021/j100565a004>
- [15] Trovarelli, A., "Catalytic properties of ceria and CeO<sub>2</sub>-containing materials," *Catal. Rev. Sci. Eng.* **38**, 439–520 (1996). <http://dx.doi.org/10.1080/01614949608006464>
- [16] Mogensen, M., Lindegaard, T., Hansen, U. R. and Mogensen, G., "Physical properties of mixed conductor solid oxide fuel cell anodes of doped CeO<sub>2</sub>," *J. Electrochem. Soc.* **141**, 2122–2128 (1994). <http://dx.doi.org/10.1149/1.2055072>
- [17] Steele, B. C. H., "Appraisal of Ce<sub>1-y</sub>Gd<sub>y</sub>O<sub>2-y/2</sub> electrolytes for IT-SOFC operation at 500°C," *Solid State Ionics* **129**, 95–110 (2000). [http://dx.doi.org/10.1016/S0167-2738\(99\)00319-7](http://dx.doi.org/10.1016/S0167-2738(99)00319-7)
- [18] Masui, T., Fujiwara, K., Machida, K. I., Adachi, G. Y., Sakata, T. and Mori, H., "Characterization of cerium(IV) oxide ultrafine particles prepared using reversed micelles," *Chem. Mater.* **9**, 2197–2204 (1997). <http://dx.doi.org/10.1021/cm970359v>
- [19] Özer, N., "Optical properties and electrochromic characterization of sol-gel deposited ceria films," *Sol. Energy Mater. Sol. Cells* **68**, 391–400 (2001). [http://dx.doi.org/10.1016/S0927-0248\(00\)00371-8](http://dx.doi.org/10.1016/S0927-0248(00)00371-8)
- [20] Chen, C. H., Shieh, J., Hsieh, S. M., Kuo, C. L. and Liao, H. Y., "Architecture, optical absorption, and photocurrent response of oxygen-deficient mixed-phase titania nanostructures," *Acta Mater.* **60**, 6429–6439 (2012). <http://dx.doi.org/10.1016/j.actamat.2012.08.030>
- [21] Kubelka, P. and Munk, F., "Ein Beitrag zur optik der farbanstriche," *Z. Tech. Phys.* **12**, 593–601 (1931).
- [22] Tauc, J., Grigorovici, R. and Vancu, A., "Optical properties and electronic structure of amorphous germanium," *Phys. Status Solidi B* **15**, 627–637 (1966). <http://dx.doi.org/10.1002/pssb.19660150224>
- [23] Zhang, F., Wang, P., Koberstein, J., Khalid, S. and Chan, S. W., "Cerium oxidation state in ceria nanoparticles studied with X-ray photoelectron spectroscopy and absorption near edge spectroscopy," *Surf. Sci.* **563**, 74–82 (2004). <http://dx.doi.org/10.1016/j.susc.2004.05.138>
- [24] Deshpande, S., Patil, S., Kuchibhatla, S. V. N. T. and Seal, S., "Size dependency variation in lattice parameter and valency states in nanocrystalline cerium oxide," *Appl. Phys. Lett.* **87**, 133113 (2005). <http://dx.doi.org/10.1063/1.2061873>
- [25] Khan, S. U. M., Al-Shahry, M. and Ingler Jr., W. B., "Efficient photochemical water splitting by a chemically modified n-TiO<sub>2</sub>," *Science* **297**, 2243–2245 (2002). <http://dx.doi.org/10.1126/science.1075035>, PMID:12351783
- [26] Sakthivel, S. and Kisch, H., "Daylight photocatalysis by carbon-modified titanium dioxide," *Angew. Chem. Int. Ed.* **42**, 4908–4911 (2003). <http://dx.doi.org/10.1002/anie.200351577>, PMID:14579435

- [27] Raja, K. S., Gandhi, T. and Misra, M., "Effect of water content of ethylene glycol as electrolyte for synthesis of ordered titania nanotubes," *Electrochem. Commun.* *9*, 1069–1076 (2007). <http://dx.doi.org/10.1016/j.elecom.2006.12.024>
- [28] Drake, N. L. and Smith, T. B., "The decomposition of ethylene glycol in the presence of catalysts. I. Vanadium pentoxide as catalyst," *J. Am. Chem. Soc.* *52*, 4558–4566 (1930). <http://dx.doi.org/10.1021/ja01374a058>



## A Comparison Between Experimental and Simulation Results in the Fabrication of Nanoporous Platinum Thin Films for Hydrogen Sensing

DR. ADITYA ABBURI

*Department of Physics, Galgotias University, Gautam Buddh Nagar, UP, India 201308*

*Department of Physics, University of Idaho, Moscow, ID, USA 83844*

### KEYWORDS

nanoporous  
thin films  
dealloying  
KMC  
hydrogen sensor

### ABSTRACT

Nanoporous thin films are fabricated by a method of dealloying and coarsening. Dealloying is a common process during which selective dissolution of the most electrochemically active element of the alloy is etched out. This paper compares the results obtained for nanoporous platinum thin films by experimental fabrication and by Kinetic Monte Carlo simulations. Experimentally, the sizes of the pores were controlled by a method of coarsening at different temperatures after dealloying. The KMC simulations also showed similar results which was governed by the temperature dependence of surface diffusion of the platinum adatoms in the thin film. Good agreement is found between experimentally observed and simulated results. A hydrogen gas sensor device was built using the platinum nanoporous thin film and it showed good response to low concentrations of hydrogen.

© 2014 DEStech Publications, Inc. All rights reserved.

### 1. INTRODUCTION

Hydrogen is considered one of the most attractive energy resource in the future for its high efficiency, renewable properties, and being environmentally friendly. As hydrogen has a wide range of application area, but has a potential for explosion, research is ongoing on the design and development of hydrogen gas sensors that are reliable, chemically selective, reversible, simple to operate, cheap and sensitive to low concentration of hydrogen gas with fast response time. A basic classification of sensors comprises catalytic sensors, electrochemical sensors, resistive palladium alloy sensors, field effect transistors, Schottky diodes, and semiconductor metal oxide sensors [1–3].

Nanostructured devices are being extensively investigated for their possible applications. The occurring surface effects, small-size effect, and even quantum effects markedly affect the physical and chemical properties of these nanosized materials. Nanostructures have recently attracted the attention

of scientists to overcome the limitations of current hydrogen sensors because of their surface activity, superior sensitivity, and lowpower consumption due to their small size. A nanoporous platinum film is expected to exhibit much higher surface area than a polished platinum film. This feature is very advantageous in the study of electrochemical reactions involving adsorption which include sensing of hydrogen. In this work, a process of cosputtering, dealloying and coarsening was employed to fabricate nanoporous platinum (np-Pt) thin films. These films substantially increase the surface area and number of site for hydrogen adsorption on the platinum surface.

Nanoporous materials are increasingly being used as catalysts [4] and as absorption media [5] because of their unique structural properties and large accessible internal surface area, i.e. the presence of voids of tunable dimensions at the atomic, molecular, and nanometer scales. Porous materials are also of scientific and technological importance because of their ability to absorb and interact with atoms, ions, and molecules on their large interior surfaces and in nanometer-sized pore spaces. With a unique combination of low mass and high surface area, porous materials are particularly

\*Corresponding author. Email: [aditya.abburi@gmail.com](mailto:aditya.abburi@gmail.com)

attractive for scientific research and industrial applications such as catalysis, sensing, and filtration. Thus there is a continued interest in the discovery of new porous materials, new fabrication methods, and new processing techniques to integrate them into useful forms for applications.

Dealloying is a corrosion process in which one component of an alloy is selectively removed. In the case of a binary alloy this process results in the formation of a bi-continuous metal/void structure of the more noble element. Sieradzki and Newman were the first to propose a fundamental description of the dealloying process in 1987 [6]. They described the dealloying process as a competing process of surface roughening and surface smoothing [7,8]. Nanostructured devices are being extensively investigated for their possible applications. The occurring surface effects, small-size effect, and even quantum effects markedly affect the physical and chemical properties of these nanosized materials. Nanostructures have recently attracted the attention of scientists to overcome the limitations of current hydrogen sensors because of their surface activity, superior sensitivity, and low-power consumption due to their small size. A nanoporous platinum film is expected to exhibit much higher surface area than a polished platinum film. This feature is very advantageous in the study of electrochemical reactions involving adsorption which include sensing of hydrogen.

Kinetic Monte Carlo models are dynamic Monte Carlo algorithms that use a simplified transition state theory [9] to model the kinetics of slow processes as opposed to the fast kinetics (on the order of picoseconds) modeled by molecular dynamics by abstracting the individual motions of every particle to the less intensive task of tracking only successful outcomes to transitions.

## 2. EXPERIMENTAL FABRICATION OF NANOPOROUS PLATINUM

The alloy thin films were fabricated by a method of co-sputtering of copper and platinum using the ATC 1800F multigun sputtering system. Si (001) wafers 0.5  $\mu\text{m}$  thick were chosen as the substrate to deposit the thin films. The sputtering rate of the two targets was first determined by fixing one set of values of the following parameters: DC/RF power, gas pressure, deposition time, and the gun angle toward the sample. The thin film was fabricated by supplying power to both the guns simultaneously. The power supplied to the guns was adjusted to obtain the desired composition of  $\text{Cu}_{80}\text{Pt}_{20}$  and the time of sputtering was adjusted such that the thickness of the deposited thin film would be 150 nm. The gun with the copper target was supplied a DC power of 75 W and the gun with the platinum target was supplied an RF power of 20 W. The thickness of sample was confirmed by using a profilometer.

The sputtered thin films were dealloyed in  $\text{H}_2\text{SO}_4$  to remove the copper. The SEM and EDX results of the deposited

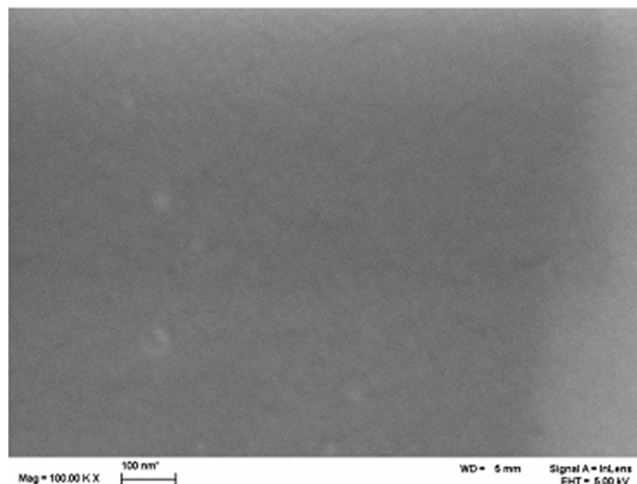


**Figure 1.** SEM image of 150 nm  $\text{Cu}_{80}\text{Pt}_{20}$  film after dealloying.

sample showed a flat surface with the elemental composition of Cu 80% and Pt 20%. The SEM morphology observations (Figure 1) of the dealloyed film did not show the presence of three dimensional voids in the network of Pt atoms. The EDX data confirmed that all the Cu in the thin film was dissolved.

Dealloying did not result in a porous structure. To obtain a porous structure, we tested several methods such as, changing the composition of the initial alloy, dealloying the sample in acid for a longer time and increasing the temperature of the acid. None of these methods resulted in the formation of pores in platinum. The dealloyed thin films were heated under vacuum at different temperatures. The samples were allowed to cool down to room temperature under vacuum. Surface characterization using FESEM was performed on each sample heated at different temperature for pore size measurements. The thermal coarsening resulted in nanoporous platinum films with different pore sizes. Figure 2(a)–(d) shows the FESEM images of the surface of the thin films after thermal coarsening at different temperatures. The pore sizes obtained were < 5 nm for 250°C, (5–10) nm for 300°C, 25 nm for 400°C and 35 nm for 500°C.

## 3. SIMULATION OF DEALLOYING AND COARSENING

Central to any KMC model are the kinetic rate laws used to describe the transition rates. In this model for dealloying, we include only diffusion and dissolution. Each of the atoms is allowed to diffuse into empty neighboring positions. In this way diffusion of adatoms on a terrace or vacancies in the bulk are treated the same, the latter being due to 11-coordinated atoms hopping into empty but 12-coordinated neighbor sites. Only LN atoms participate in dissolution. For diffusion, a “bond-breaking model,” is used by which an atom hops to an empty neighboring site by surmounting an activa-

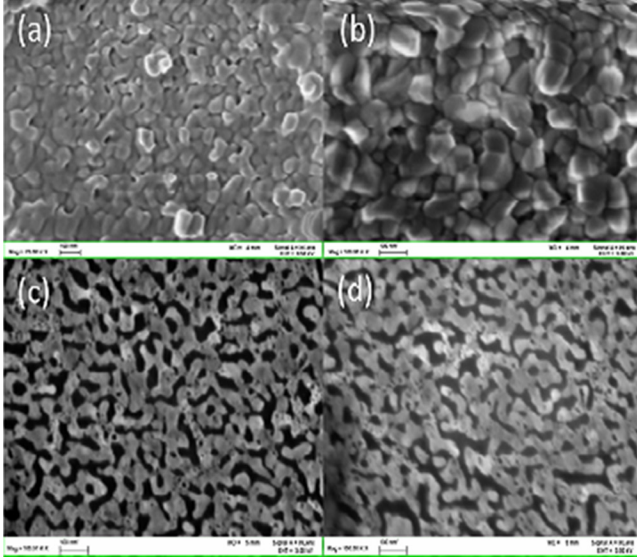


**Figure 2.** Nanoporous Pt after dealloying in 93%  $H_2SO_4$  and (a) coarsened at 250°C (b) coarsened at 300°C (c) coarsened at 400°C (d) coarsened at 500°C.

tion barrier whose height equals the sum of bond-interaction energies to all neighboring atoms.

The two types of transitions allowed for metal atoms in this model were diffusional transitions among lattice sites that were bordered by the electrolyte and dissolution events in which the atom gave up a certain number of electrons and became an ion in the electrolyte. An Arrhenius form was used for both types of rate equations (diffusion and dissolution). The transition rates used in this model were calculated using:

$$R_i = v_i e^{-\frac{E_b^i}{k_b T}} \quad (1)$$

$R_i$  is the rate of process  $i$ ,  $v_i$  is the oscillation frequency,  $E_b^i$  is an energy barrier,  $k_b$  is the Boltzmann constant, and  $T$  is the simulation temperature in Kelvin. In the diffusion transition, the atom overcame the energy barrier for diffusion ( $E_{Diff}^{Barrier}$ ) and in the dissolution transition; the atom overcame the energy barrier ( $E_{Diss}^{Barrier}$ ) for dissolution. In both transitions, the zero-point for the energy well was set at infinity; that is, the atom was required to break all of its near-neighbor bonds before it could undergo the transition. The rates obtained from Equation (1) were used to calculate the event probabilities and to determine the iteration  $\Delta t$ .

The probability of a particular transition occurring is equal to the ratio of that transition rate to the total transition rate. The total transition rate,  $R_T$ , is equal to the sum for all the possible transitions that can occur in a particular iteration. In the case of the simulation developed for this dealloying model, the time-step was chosen to be proportional to the inverse of the total transition rate.

$$\Delta t = \frac{1}{R_1 + R_2 + R_3} = \frac{1}{R_T} \quad (2)$$

The oscillation frequency,  $v$ , for diffusion was chosen to be on the same order as the Debye frequency of the lattice:  $1 \times 10^{13}/s$ , for both the least noble and most noble components. For dissolution,  $v$  was determined empirically as  $1 \times 10^4/s$  for the LN component, after Erlebacher [10].

The energy barriers,  $E_{Diff}^{Barrier}$ ,  $E_{Diss}^{Barrier}$  to diffusion and dissolution, were determined using a local bond-breaking approximation—that is, the number and type of nearest-neighbor bonds for the atom of interest established its barrier to motion or dissolution [11]. For diffusion in a binary system, the energy barrier for diffusional motion was given by Equation (3) for an atom,  $j$ , with a given configuration of  $A$  and  $B$  metal and electrolyte neighbors.

$$E_b^j = mmE_{A-A} + nnE_{A-B} + ppE_{A-e} \quad (3)$$

$E_{A-A}$  is the bond energy between  $A-A$  atoms,  $E_{A-B}$  is the bond energy between  $A-B$  atoms,  $E_{A-e}$  is the interaction energy between an  $A$  atom and a neighboring electrolyte component,  $mm$  is the number of  $A-A$  bonds,  $nn$  is the number of  $A-B$  bonds, and  $pp$  is the number of  $A-e$  interactions

Likewise, for dissolution, the energy barrier ionization was given by Equation (4) for a given configuration of  $A$  and  $B$  atom neighbors and electrolyte neighbors for an atom,  $j$ ,

$$E_b^j = \{mmE_{A-A} + nnE_{A-B} + ppE_{A-e}\} - (V_{app} - E_r) \quad (4)$$

$V_{app}$  is the externally applied potential and  $E_r$  is an energy barrier related to the Nernst potential. As the experiments we performed were simple chemical dealloying and not electrochemical dealloying, both  $V_{app}$  and  $E_r$  are 0.

Table 1 provides data on the binding energies for platinum and copper. The inter-species binding energies were obtained using the assumption that the metal components formed an ideal solution.

$$E_{A-B} = \frac{1}{2}(E_{A-A} + E_{B-B}) \quad (5)$$

There were two ways in which the MN and LN atoms were distinguished in the model: the first was through the

**Table 1. Binding Energies for Atoms in the Simulation Alloys.**

Bond Type	Energy per Bond (eV)
Pt-Pt*	-0.69
Cu-Cu*	-0.58
Cu-Pt**	-0.63

\*These values were obtained from literature.

\*\*This value was obtained using Equation (5).

value used for the dissolution hop frequency—which was empirically determined as described above. The second was through its binding energy with like and unlike neighbors.

In the model developed in this work the Bortz-Kalos-Lebowitz [12] algorithm was adopted for the KMC implementation. The algorithm proceeded as follows:

1. The system was initialized at time  $t = 0$ . That is, the crystal structure was generated with the specified alloy composition and the electrolyte was populated with the desired concentration of ions. A nearest neighbor look-up table was created.
2. A look up table of all of the possible energy wells based on every configuration of neighbors was generated.
3. The main execution loop was begun based on the # of iterations input for that simulation. A cut-off time of 100,000 seconds in the simulation world was established. That is, if, in the course of the simulation, the simulated dealloying time exceeded  $1 \times 10^5$  seconds then the simulation was stopped.
  - a. Enumerated all of the metal atoms in the alloy-electrolyte interface and stored their dissolution and diffusion rates and potential exchange sites.
  - b. Calculated the cumulative rate function:  $R_T = \sum_i R_i$  where  $R_i$  was the rate for a process and  $i$  was an index that looped over the dissolution and diffusion processes.  $R_T$  was the total rate.
  - c. Determined the probabilities for all events,  $i$ , to occur by obtaining  $P_i = R_i/R_T$
  - d. Obtained a uniform random number,  $u1$ , between 0 and 1 and determine the event that would be carried out by finding the event,  $i$ , for which  $P_{i-1} < u1 < P_i$ .
  - e. Carried out event  $i$  by exchanging an atom with an electrolyte component or ionizing the atom.
  - f. Obtained a new uniform random number,  $u2$  between 0 and 1 and updated the time step such that  $t = t + \Delta t$
  - g. Checked to see if the simulation count was exceeded or if the simulation time cutoff was exceeded. If not, proceed to step 3a.

The simulation progresses by dynamically tracking all events that may occur, then picking one at random according to its weighted probability and incrementing the time step appropriately. At this point, the list of all possible transitions has changed (some atoms may have evaporated, or their coordination may have changed due to a nearby diffusion event), so the list of all possible transitions must be updated. Once updated, a new time step may be calculated and the cycle repeated. For every iteration of the simulation, two random numbers are picked. The first picks the kind of transition, and the second picks the particular manifestation of that transition.

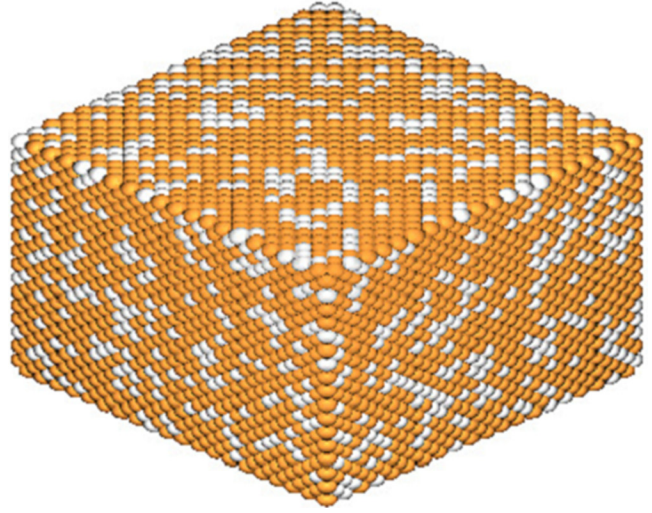


**Figure 3.** Generated CuPt sample by simulation model.

To perform the coarsening simulations at various temperatures, the final data obtained after dealloying is used as the initial crystal structure. Diffusion is the only process that is allowed to occur during the simulation run. The temperature and time of simulation are the two parameters that are input into the program. Rendering of the ligament was made with the freeware program POV-RAY, in which atoms were portrayed as opaque spheres illuminated by directed light sources.

We found that the KMC model was able to reproduce all relevant experimental characteristic of dealloying CuPt. Initially the simulation sample was formed and all data was recorded by the program. The required parameters, which included the electrolyte and the temperature at which experiments were performed are entered and the simulation was started. POV-RAY is a freeware program that was used to render the simulation images from the output data files. The output files were opened in POV-RAY and the images were obtained. Figure 3 shows a simulation sample that was a binary alloy composed of 80% of the LN component (Copper) and 20% of the MN component (Platinum).

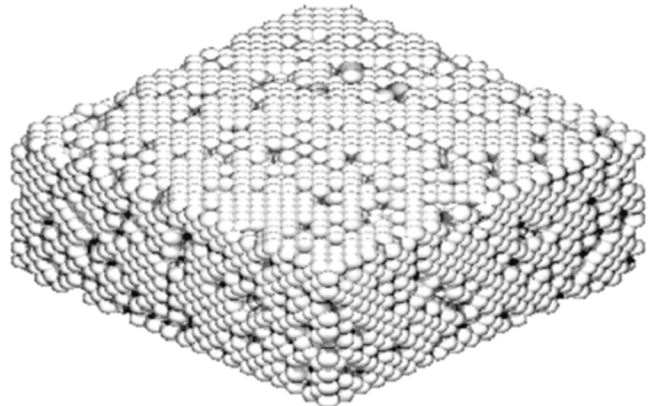


**Figure 4.** Dealloyed Film obtained from the simulation program.

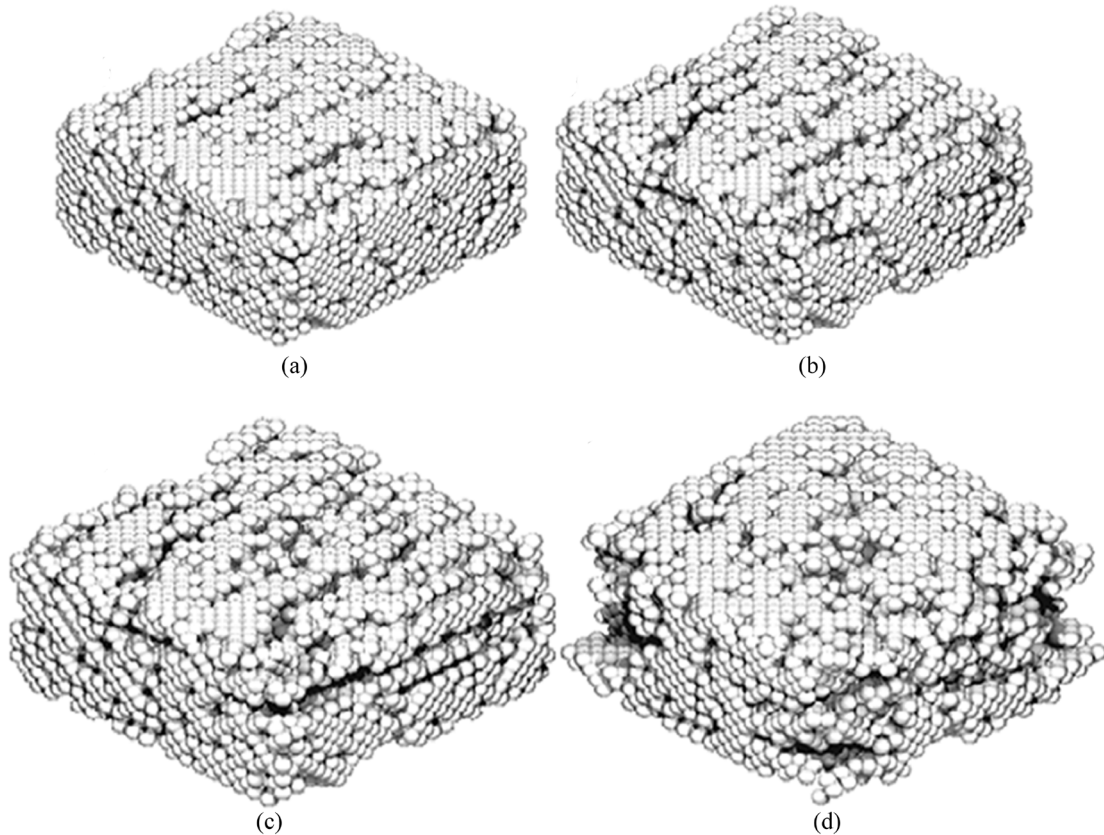


**Figure 5.** Simulation results after coarsening for 30 minutes at (a) 250°C (b) 300°C (c) 400°C (d) 500°C.

The rendered output file at the end of the simulation time is shown in Figure 4. The image shows the dealloyed thin film. We saw that no copper atoms remained in the film. It also shows the presence of no pores in the film. This is consistent with our experimental results. We only see vacancy sites throughout the film.

The data file obtained from the dealloyed film was input into the program to study the effect of coarsening on the dealloyed films. During coarsening, only diffusion of the remaining atoms takes place and the rate of diffusion directly depends on the temperature [Equation (1)]. The temperature and time of coarsening were the two inputs given to the simulation. Simulations were performed to repeat experimental conditions for coarsening the dealloyed film for 30 minutes at 250°C, 300°C, 400°C and 500°C. Figure 5(a)–(d) show the rendered images of the coarsened thin films. The evolution of porosity is clearly visible in the figures.

The top layers of the rendered dealloyed and coarsened images were extracted to analyze the porosity in the films. Figure 6 shows the top layer of the as dealloyed film before coarsening. Figure 7(a)–(d) show the extracted top layers of the rendered images. ImageJ manipulates the average area occupied by the pores in a two dimensional sample. The top layer from the simulated image was extracted and the porosity was calculated.

The data was compared to the porosity calculated from the surface morphology obtained from the SEM images. Table 2 shows the obtained porosity values and the percentage error calculated between the experimental and simulated results. The results obtained from experiments and simulations confirm that the evolution of porosity can be controlled by controlling the temperature at which the samples are coarsened post dealloying.

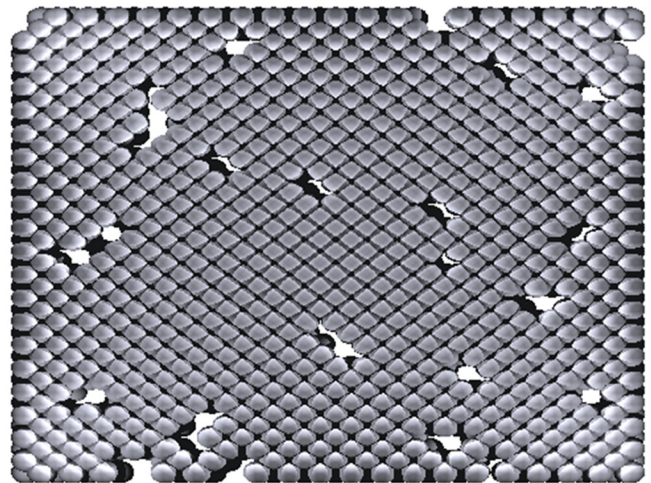


**Figure 6.** Extracted top layer of the simulated image after dealloying.

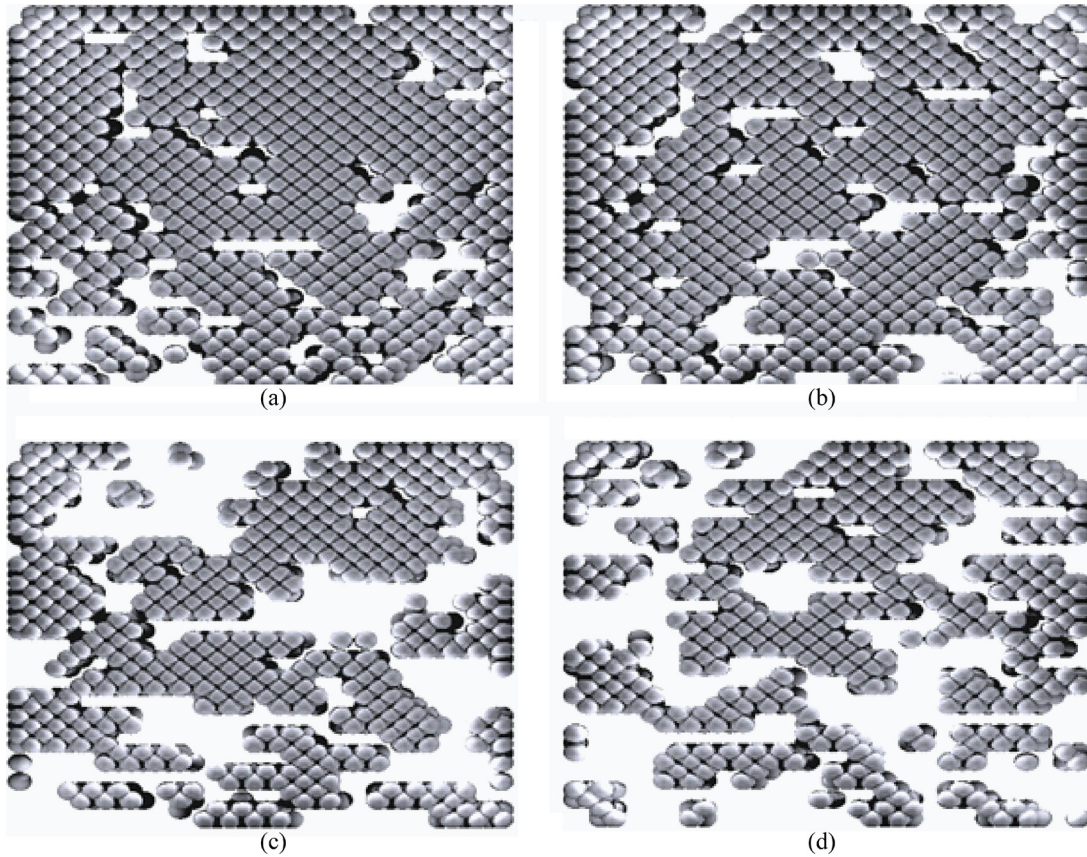


**Figure 7.** Extracted top layers from simulation results after coarsening for 30 minutes at (a) 250°C; (b) 300°C; (c) 400°C; (d) 500°C.

#### 4. HYDROGEN SENSOR

Nanoporous Pt thin films were fabricated by a method of co-sputtering, dealloying and coarsening. A microscope glass slide with dimensions 2.5 cm × 7 cm was the substrate used. The sensor device was prepared on the nanoporous platinum thin films. A stainless steel mask was used to define a four probe pattern required for four-probe DC measurements. The sensitivity of the fabricated np-Pt thin films to hydrogen was determined by a resistance transient method where the change in resistance at different concentrations of hydrogen was measured. The resistance of the np-Pt thin film at normal air conditions under atmospheric pressure was taken as the base value. The resistance at each measured value of current was calculated and tabulated.

**Table 2. Comparison of Porosity between Experimental and Simulated Results.**

Temperature	Porosity from Experiment	Porosity from Simulation	Percent Error
250°C	0.230838911	0.216434	6.65%
300°C	0.3245796	0.3187462	1.83%
400°C	0.4965248	0.5146215	3.51%
500°C	0.53475743	0.5523239	3.18%

The device was placed in a chamber and pumped down to vacuum for 300 seconds. At the end of this time, the chamber was filled with 1000 ppm of hydrogen in air. Figure 8 shows the percent change in resistance versus time. The initial part of the curve till 300 seconds shows that there was no change in resistance from the base value even under vacuum. After 300 seconds, we saw that there was a change in the resistance with time. The change in resistance saturated at a different peak value for each sample with different pore size. We see that the sensitivity increased from 0.6% for the control sample with no pores to 1.5% for pore size of < 5 nm and further increased to 3.5% for 35 nm sized pores on the thin film. The increase in the sensitivity of the sensor with increase in pore size can be explained by the phenomenon of enhanced Knudsen diffusion coefficient ( $D_k$ ). This increase in the amount of diffused hydrogen causes a larger change in the conductivity of the nanoporous thin film or an increase in the sensitivity of the device to the gas. Hence we see the sensitivity of the sensor increase with an increase in the pore size.

To test the repeatability of the sensor, the sample with pore size of 35 nm was tested for multiple exposures to hydrogen. The sensor was left at its highest response value of 3.5% for 5 minutes following which the chamber was con-

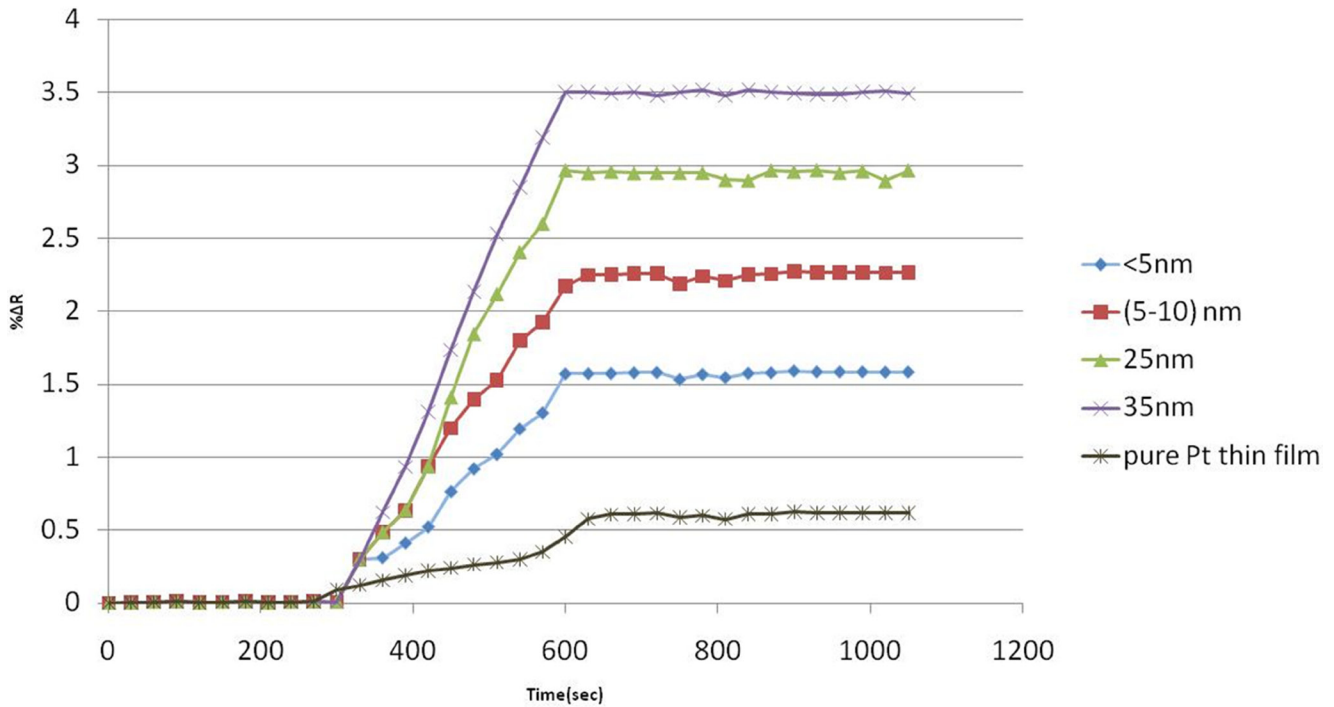


Figure 8. Percent change in resistance of control sample and different pore-sized nanoporous Pt thin films at 25°C and 1000 ppm of H<sub>2</sub>.

tinuously purged with 200 sccm of nitrogen for 5 minutes. During the 5 minutes of purging, the response decreased sharply reaching a steady state value as seen in Figure 9 and the resistance went back to its original value. The chamber was then pumped down to vacuum for 5 minutes and 1000

ppm of hydrogen was reintroduced. This process was repeated multiple times and results confirm that the sensing properties of the thin film remained the same. The nanoporous Pt thin film sensor was totally reversible and showed repeatability.

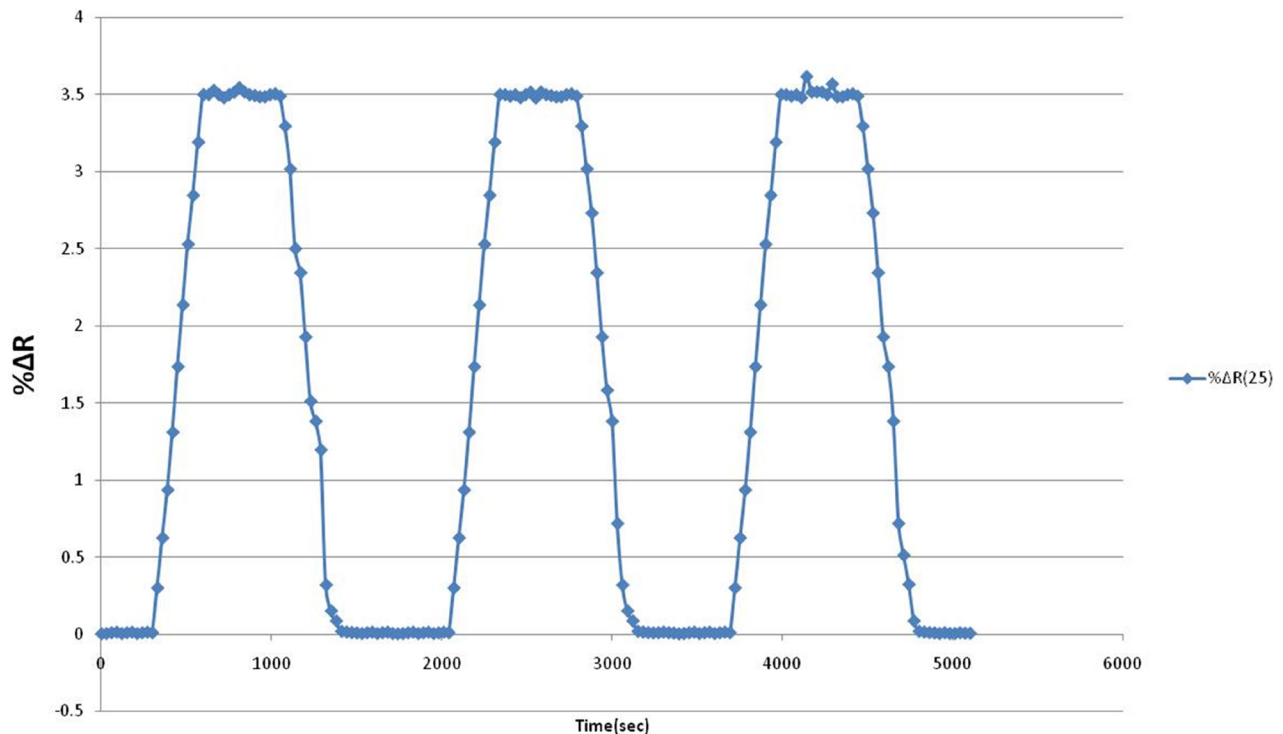


Figure 9. Percent change in resistance of the nanoporous Pt thin film for multiple exposures to 1000 ppm of H<sub>2</sub>.

## 5. CONCLUSIONS

The simulation model explained in this paper reproduces the characteristics of dealloying and coarsening and the observation of porosity evolution. The conclusion that can be made is that the porosity or average size of pores depends on the temperature of coarsening. The simulation results agree very closely with the experimental results showing the increase of porosity with increase in coarsening temperature. Nanoporous Pt thin film based sensor for hydrogen detection has been fabricated and tested. The pore size dependence was studied along with the repeatability of the sensing mechanism. It has been observed that sensors made with nanoporous platinum demonstrate a significant change in resistance when exposed to hydrogen. In summary, chemical dealloying followed by coarsening of amorphous copper-platinum co-sputtered alloy films results in the self assembly of polycrystalline nanoporous metal structures with controllable pore sizes. This process is a new approach to forming high surface area Pt electrodes on Si for emerging applications such as hydrogen gas sensors, non enzymatic glucose sensors, microfuelcells, biosensors, microbatteries, and supercapacitors.

## REFERENCES

- [1] T. Xu, M. P. Zach, Z. L. Xiao, D. Rosenmann, U. Welp, W. K. Kwok, and G. W. Crabtree, "Self-assembled monolayer-enhanced hydrogen sensing with ultrathin palladium films," *Appl. Phys. Lett.*, vol. 86, no. 20, pp. 203104-1–203104-3, 2005. <http://dx.doi.org/10.1063/1.1929075>
- [2] C. Christofides and A. Mandelis, "Operating characteristics and comparison of photopyroelectric and piezoelectric sensors for trace hydrogen gas detection. II. Piezoelectric quartz-crystal microbalance sensor," *J. Appl. Phys.*, vol. 66, no. 9, pp. 3986–3992, 1989. <http://dx.doi.org/10.1063/1.344006>
- [3] P. F. Ruths, S. Ashok, S. J. Fonash, and J. M. Ruths, "A study of Pd/SiMIS Schottky barrier diode hydrogen detector," *IEEE Trans. Electron Devices*, vol. 28, no. 9, pp. 1003–1009, Sep. 1981. <http://dx.doi.org/10.1109/T-ED.1981.20475>
- [4] Y. Ding, Y.-J. Kim, and J. Erlebacher, "Nanoporous Gold Leaf: Ancient Technology/Advanced Material," *Advanced Materials*, vol. 16, no. 21, pp. 1897–1900, Nov. 2004. <http://dx.doi.org/10.1002/adma.200400792>
- [5] F. B. Surani, X. Kong, and Y. Qiao, "Two-staged sorption isotherm of a nanoporous energy absorption system," *Applied Physics Letters*, vol. 87, no. 25, p. 251906, 2005. <http://dx.doi.org/10.1063/1.2144280>
- [6] K. Sieradzki and R. Newman, "Stress-corrosion cracking," *Journal of Physics and Chemistry of Solids*, vol. 48, no. 11, pp. 1101–1113, 1987. [http://dx.doi.org/10.1016/0022-3697\(87\)90120-X](http://dx.doi.org/10.1016/0022-3697(87)90120-X)
- [7] K. Sieradzki, R. R. Corderman, K. Shukla, and R. C. Newman, "Computer simulations of corrosion: Selective dissolution of binary alloys," *Philosophical Magazine A*, vol. 59, no. 4, pp. 713–746, Apr. 1989. <http://dx.doi.org/10.1080/01418618908209817>
- [8] K. Sieradzki, "Curvature Effects in Alloy Dissolution," *Journal of The Electrochemical Society*, vol. 140, no. 10, p. 2868, 1993. <http://dx.doi.org/10.1149/1.2220924>
- [9] A. Voter, "Classically exact overlayer dynamics: Diffusion of rhodium clusters on Rh(100)," *Physical Review B*, vol. 34, no. 10, pp. 6819–6829, Nov. 1986. <http://dx.doi.org/10.1103/PhysRevB.34.6819>
- [10] J. Erlebacher, "An Atomistic Description of Dealloying," *Journal of The Electrochemical Society*, vol. 151, no. 10, p. C614, 2004. <http://dx.doi.org/10.1149/1.1784820>
- [11] G. Bales and D. Chrzan, "Dynamics of irreversible island growth during submonolayer epitaxy," *Physical Review B*, vol. 50, no. 9, pp. 6057–6067, Sep. 1994. <http://dx.doi.org/10.1103/PhysRevB.50.6057>
- [12] A. B. Bortz, M. H. Kalos, and J. L. Lebowitz, "A new algorithm for Monte Carlo simulation of Ising spin systems," *Journal of Computational Physics*, vol. 17, no. 1, pp. 10–18, Jan. 1975. [http://dx.doi.org/10.1016/0021-9991\(75\)90060-1](http://dx.doi.org/10.1016/0021-9991(75)90060-1)



## Characterization of the Microstructure and Photoelectrical Properties of TiO<sub>2</sub>-SrTiO<sub>3</sub> and TiO<sub>2</sub>-CeO<sub>2</sub> Nanocomposites

CHUN-HSIEN CHEN<sup>1</sup>, JAY SHIEH<sup>1,\*</sup> and JING-JONG SHYUE<sup>1,2</sup>

<sup>1</sup>Department of Materials Science and Engineering, National Taiwan University, 1 Roosevelt Road, Sec. 4, Taipei 106, Taiwan

<sup>2</sup>Research Center for Applied Sciences, Academia Sinica, 128 Academia Road, Sec. 2, Taipei 115, Taiwan

### KEYWORDS

titania  
strontium titanate  
ceria  
nanocomposites  
heterojunction  
photocatalysis

### ABSTRACT

The microstructure, optical absorption and photocurrent response of TiO<sub>2</sub>-SrTiO<sub>3</sub> and TiO<sub>2</sub>-CeO<sub>2</sub> nanostructured composites based on the design of coating the surfaces of anodized TiO<sub>2</sub> nanotube arrays with large band gap SrTiO<sub>3</sub> or small band gap CeO<sub>2</sub> nanoparticles have been investigated in this study. The nanocomposites were fabricated by a combination of anodization, hydrothermal and post-annealing methods. The UV-visible and ultraviolet photoelectron spectra of the structural components were measured in order to determine the electronic band structures of the TiO<sub>2</sub>-SrTiO<sub>3</sub> and TiO<sub>2</sub>-CeO<sub>2</sub> heterojunctions. These heterojunctions are designed to promote the separation of photoinduced charge carriers when the nanocomposites are adopted in photocatalytic or photoelectrode applications. The TiO<sub>2</sub>-SrTiO<sub>3</sub> and TiO<sub>2</sub>-CeO<sub>2</sub> heterojunctions were confirmed to possess large conduction and valence band offsets, promoting the separation of photoinduced electron and hole (e<sup>-</sup>/h<sup>+</sup>) pairs. The photocurrent densities of the TiO<sub>2</sub>-SrTiO<sub>3</sub> and TiO<sub>2</sub>-CeO<sub>2</sub> nanocomposites were about 15–40% larger than that of the anatase TiO<sub>2</sub> nanotube arrays. The size and crystallinity of the SrTiO<sub>3</sub> and CeO<sub>2</sub> nanoparticles, which could be controlled by the hydrothermal and annealing conditions, and the concentration of oxygen vacancies within the TiO<sub>2</sub> nanotube arrays were identified to be the key factors influencing the photocurrent response of the nanocomposites.

© 2014 DEStech Publications, Inc. All rights reserved.

### 1. INTRODUCTION

For solar energy applications, photocatalytic decomposition of molecules (e.g. water splitting and pollutant breakdown) is one of the main topics of interest and research. In photocatalytic water splitting, how to choose suitable semiconductor materials for photoelectrode applications is undoubtedly the most critical issue [1,2]. Since splitting of water into H<sub>2</sub> and O<sub>2</sub> on titania (TiO<sub>2</sub>) photoelectrode was demonstrated by Fujishima and Honda in the early 1970s [3], there have been many studies focusing on improving the photocatalytic properties of TiO<sub>2</sub> [4–7]. However, there are some difficulties in TiO<sub>2</sub> photocatalysis under solar irradiation, such as high recombination rate of photoinduced elec-

tron and hole (e<sup>-</sup>/h<sup>+</sup>) pairs and low absorption in the visible range. In order to improve the separation of photoinduced charge carriers, TiO<sub>2</sub>-based photocatalytic composites consisting of materials of different semiconducting properties, for example, different band gaps for absorbing light of different wavelengths, have been developed for their superior photocatalytic properties [8–10]. When TiO<sub>2</sub> and another semiconductor material are combined into a composite heterostructure, electronic band offsets at the material interface (i.e. heterojunction) are expected to exist. The band offsets created could be utilized to promote the separation of photoinduced e<sup>-</sup>/h<sup>+</sup> pairs, improving the efficiency of photocatalysis [11,12].

TiO<sub>2</sub> and strontium titanate (SrTiO<sub>3</sub>) are photocatalytic materials suitable for photoanode applications due to their strong oxidizing activity and high chemical stability. Anatase and rutile are the two major crystalline phases of TiO<sub>2</sub>

\*Corresponding author. Email: [jayshieh@ntu.edu.tw](mailto:jayshieh@ntu.edu.tw)



## Study on Compressive Properties of Syntactic Foams for Marine Applications

Z. SALLEH<sup>1,2,\*</sup>, M. M. ISLAM<sup>1</sup> and H. KU<sup>1</sup>

<sup>1</sup>Centre of Excellence in Engineered Fibre Composites (CEEFC), Faculty of Engineering and Surveying, University of Southern Queensland, Toowoomba, Queensland 4350, Australia

<sup>2</sup>Malaysian Institute of Marine Engineering Technology (MIMET), Universiti Kuala Lumpur (UniKL), 32200 Lumut Perak, Malaysia

### KEYWORDS

syntactic foams  
hollow particles  
resins  
properties  
comparison

### ABSTRACT

Generally, syntactic foams are close pore foams fabricated by the mechanical mixing of hollow microsphere particles in a polymeric matrix resin. From the literature review, it was found that there are several polymeric resins that have been used for development of syntactic foams such as epoxy, cyanate ester, polypropylene, polysialate and vinyl ester. In this paper, a comparative discussion is presented on the mechanical properties and water absorption properties of hollow glass particles mixing with polymeric resins for development of syntactic foams for the use of these composites in bulk applications such as marine structures. From the previous reports, vinyl ester, epoxy resin, PP and PU as a matrix materials reinforced with glass microballoons are widely used for marine structure compared to other polymers. From the mechanical properties, the highest dynamic compress stress yield at 73.91MPa for dry NCSF 2%. Moisture condition result showed that the storage modulus and  $T_g$  for nanoclay reinforced syntactic foams up to 2% by weight increased when compared with their pure syntactic foam counterparts, irrespective of whether they were dry or moisture conditioned.

© 2014 DEStech Publications, Inc. All rights reserved.

### 1. INTRODUCTION

Sea to space involved in engineering applications such as marine and aerospace structural applications strive for materials having a combination of low density and high tensile strength, good modulus elasticity and damage tolerance. In order to achieve all these kind of characteristics lighter and strong components should be made from composite materials. Composite materials are increasingly being used in recent years in such applications especially sandwich types. Figure 1 shows the several marine application products made from syntactic foam manufactured by Trelleborg CRP companies such as mooring buoys, deep water ultra-buoys, pipe line installation buoys and umbilical floats [1]. Sandwich composites comprising low density core materials are especially useful in such applications. When use of open cell foams as core materials results in low through-the-thickness compres-

sive strength and modulus of elasticity, thereby limiting the applications of such composites [2]. A class of closed cell foams synthesized by dispersing rigid hollow particles in a matrix material has shown considerable promise for such applications called as syntactic foam [3–5]. This closed foam possesses higher density than open cell foams. However, in term of their considerably superior mechanical properties make it possible to use them in load bearing structural applications, where open cell foams cannot be used in these applications. Additionally, the presence of porosity inside hollow particles, called microballoons, leads to lower moisture absorption and lower thermal expansion, resulting in better dimensional stability [6,7]. The size and distribution of porosity can be controlled very closely in these foams by means of microballoon volume fraction and wall thickness<sup>8</sup>. An extensive variety of polymer, metal and ceramic matrix syntactic foams has been studied in the previous published literature. In polymer matrix syntactic foams, epoxy resins are most commonly used as matrix resin, due to the widespread use of these resins in aerospace applications [9–18].

\*Corresponding author. Email: [zulzamri@mimet.unkl.edu](mailto:zulzamri@mimet.unkl.edu)

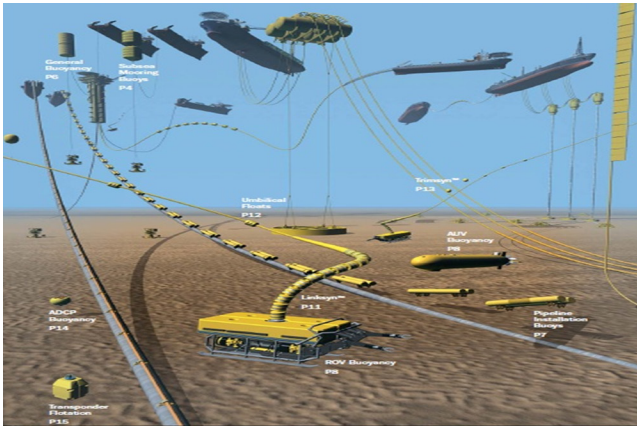


Figure 1. Several products made from syntactic foams [1].

Studies on epoxy matrix syntactic foams have produced a better understanding of correlations between properties of the composite with properties of matrix and microballoons, including their volume fractions and the micro balloon wall thickness [15,19]. However, in recent years, the increasing price of epoxy resin has required to find lower cost alternatives, especially for bulk structural applications. Additionally, the performance demands for materials are increasing.

Hence, alternatively new matrix materials need to have lower cost along with higher performance levels. Suitable polymeric material for the foam matrix can be selected from a vast range of thermosetting resins and thermoplastic resins such as cyanate ester [20], polypropylene [21], polysialate [22] and vinyl ester [23,24] as matrix materials for either cost reduction or for enhanced performance levels. In several cases, additional reinforcement such as fibres can also be added to syntactic foams to obtain certain desired properties [25,26]. This paper will investigate the development of syntactic foams with compared the characteristics such as materials used, mechanical properties and results finding from previous reports.

## 2. POLYMERIC RESINS

### 2.1. Epoxy Resin

The first production of epoxy resins manufactured in Europe and in the United States in the late 1930s and early 1940s namely company as Pierre Castan of Switzerland and S.O. Greenlee of the United States. They produce of bisphenol-A with epichlorohydrin. The families of epoxy resins that they commercialized were first used as casting compounds and coatings. Epoxy resins are a class of thermoset materials used extensively in structural and specialty composite applications because they offer a unique combination of properties that are unattainable with other thermoset resins. Available in a wide variety of physical forms from low-viscosity liquid to high-melting solids, they are amenable to a wide range of processes and applications. Epoxies

offer high strength, low shrinkage, and excellent adhesion to various substrates, effective electrical insulation, chemical and solvent resistance, low cost, and low toxicity. They are easily cured without evolution of volatiles or by-products by a broad range of chemical specie. Epoxy resins are also chemically compatible with most substrates and tend to wet surfaces easily, making them especially well-suited to composites applications. Epoxy resins are routinely used as an adhesive, coatings, encapsulates, casting materials, potting compounds, and binders. Some of their most interesting applications are found in the aerospace and recreational industries where resins and fibres are combined to produce complex composite structures. Epoxy technologies satisfy a variety of non-metallic composite designs in commercial and military aerospace applications, including flooring panels, ducting, vertical and horizontal stabilizers, wings, and even the fuselage. This same chemistry, developed for aerospace applications, is now being used to produce lightweight bicycle frames, golf clubs, snowboards, racing cars, and musical instruments. To support these applications, epoxy resins are formulated to generate specific physical and mechanical properties. The designers of these systems must balance the limitations of the raw materials and the chemistry with the practical needs of the part fabricator. While the simplest formulations may combine a single epoxy resin with a curative, more-complex recipes will include multiple epoxy resins, modifiers for toughness or flexibility or flame/smoke suppression, inert fillers for flow control or coloration, and a curative package that drives specific reactions at specified times. When selecting a thermoset resin, consideration is usually given to tensile strength, modulus and strain, compression strength and modulus, notch sensitivity, impact resistance, heat deflection temperature or glass transition temperature ( $T_g$ ), flammability, durability in service, material availability, ease of processing, and price. Epoxy resins are of particular interest to structural engineers because they provide a unique balance of chemical and mechanical properties combined with extreme processing versatility. In all cases, thermoset resins may be tailored to some degree to satisfy particular requirements, so formulation and processing information are often maintained as trade secrets. The three basic elements of an epoxy resin formulation that must be understood when selecting a thermoset system are the base resin, curatives, and the modifiers. When formulating an epoxy resin for a particular use, it is necessary to know what each of these components contributes to the physical and mechanical performance of the part during and after fabrication.

### 2.2. Cyanate Ester (CE) Resin

Cyanate Ester (CE) are a family of high-temperature thermosetting resins—more accurately named polycyanurates—that bridge the gap in thermal performance between

engineering epoxy and high-temperature polyimides. In addition to their outstanding thermal performance, CE resins have several desirable characteristics that justify their higher cost in many applications. They possess a unique balance of properties and are particularly notable for their low dielectric constant and dielectric loss, low moisture absorption, low shrinkage, and low outgassing characteristics. Despite their relatively high cost they have found wide applications in electronics, printed circuit boards, satellite and aerospace structural composites, and low-dielectric and radar applications. They can be formulated for use as high-performance adhesives, syntactic foams, honeycomb, and fibre-reinforced composites and are often found in blends with other thermosetting resins such as epoxy, bismaleimide, and engineering thermoplastics. Grigat first successfully synthesized aryl cyanate monomers in the early 1960s, and in 1963, a process was developed to produce the monomers commercially. In the 1970s, the first patents for CE resins were awarded to Bayer AG and Mobay. These patents focused primarily on their use in printed circuit boards (PCBs), using a bisphenol A-based prepolymer. In the late 1970s, patents were licensed to Mitsubishi Gas Chemical and Celanese. Mitsubishi marketed a CE and bismaleimide blend under the name BT resin. Both blended and 100% CE resins systems were initially targeted into the PCB industry. In the 1980s, Hi-Tech Polymers, formerly Celanese, was instrumental in the commercial development of CE resin technology by producing and characterizing a wide array of different polymer backbones with CE functionality. Dave Shimp and Steve Ising of Hi-Tech Polymers are noted for their great contribution to the applications and development of CE polymers during this period. By the mid-1980s, work was proceeding on the development of commercial CE and CE/epoxy blends for aerospace and PCB applications. This work was undertaken because of keen interest in improving the hot/wet performance of composites for both structural composites and electronic applications. Cyanate esters were selected for development because of their excellent low moisture-absorbing characteristics and high mechanical and thermal performance. But, due to their high cost and lack of a comprehensive database, they did not penetrate into the large commercial aircraft and structural composite industry. It also accepted for dimensionally critical applications in space structures where weight-to-stiffness trade-offs allow higher materials costs. Lower-cost CE resins and CE blends with epoxy and with bismaleimide were eventually developed and entered the electronics industry; these lower-cost resins and blends currently account for approximately 80% of CE use.

### 2.3. Vinyl Ester

Polymeric resin such as vinyl esters are widely used in marine structural applications. Hence, investigating the

properties of vinyl ester matrix syntactic foams and developing structure-property correlations for these materials represent important challenges. The existing studies on vinyl ester syntactic foams have used fly ash chenosphere as the hollow particles [23–25]. Chenosphere's are by-products of combustion of coal in thermal power plants also called as carbon black. Such particles have large number of defects, considerable variation in chemical composition, different microstructures and porosity in embedded in their walls [26]. Hence, the properties of such particles and resulting composites are expected to be significantly affected by these inhomogeneities present in chenosphere. The present study uses borosilicate glass microballoons to fabricate syntactic foams so that the properties of the composite can be better related to the properties of constituent materials and their volume fractions.

Epoxy-glass microballoon syntactic foams have shown that their properties can be tailored by selecting appropriate type of microballoons, and using them in different volume fractions [8]. Similar to most porous materials [27], the strength and modulus of syntactic foams increase with increasing density. Only a few compositions of syntactic foams show superior mechanical properties compared to those of the neat resin. Therefore, a significant challenge is to develop syntactic foams with superior mechanical properties and lower density than the neat resin. In this paper, collecting result from the previous research will be discussed and compared when used variety of polymeric resin as matrix either from thermosetting and thermoplastic resins has been used. While the effect on volume fraction and wall thickness from the microballons is also explained such as tensile properties and modulus elasticity. From the literature review thermosetting and thermoplastic materials polymeric resins extensively used for polymer matrix in syntactic foam.

### 3. COMPARISON OF MECHANICAL PROPERTIES

The mechanical properties for syntactic foam mainly carried out using the Universal Tensile Machine (UTM) Instron 4469 and 4467. Table 1 shows the results for mechanical properties of several syntactic foams. Among all polymeric resin, vinyl ester is widely used as matrix in syntactic foam in marine application. From the previous report, understanding the dynamic compressive behaviour of vinyl ester based syntactic foams when subjected to hygrothermal conditioning is of critical importance as these systems will eventually find applications in deep seawater devices [29]. From the previous result for nanoclay syntactic foam sample (NCSF) shows that the dynamic strength is about 40–135% higher than their corresponding static compressive strength. With an increase in strain rate, the compressive strength increases irrespective of the type of conditioning. The reduction in dynamic compressive properties of the DI (De-Ionised) conditioned specimen (40–46%) was high when compared

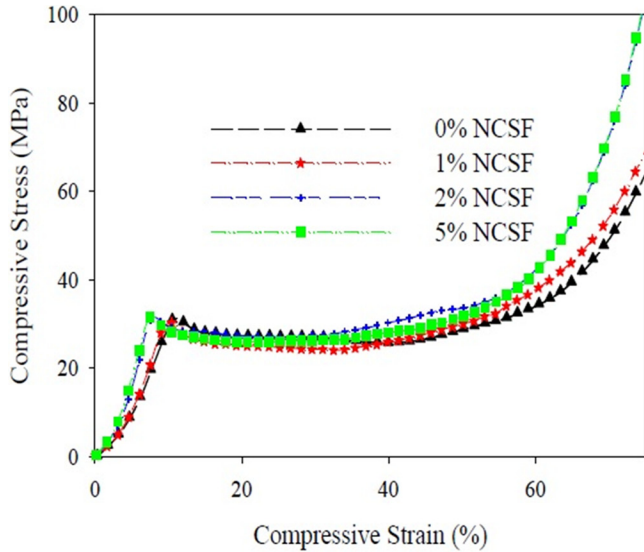


Figure 2. Compressive stress-strain diagram for vinyl ester syntactic foams [29].

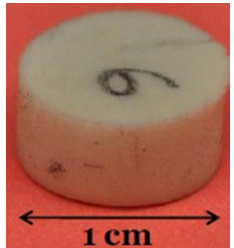
with SW (Sea Water) specimen (27–42%). It can be seen that the maximum dynamic compressive strength at 73.91 MPa, 51.04 MPa and 44.66 MPa for dry NCSF 2%, SW NCSF 5% and DI NCSF 2% respectively. While for the maximum compress yield strength at 32.53 MPa, 24.51 MPa and 24.12 MPa for dry NCSF 2%, SW NCSF 2% and DI NCSF 5% were recorded respectively at Figure 2. Common material syntactic foam for marine application was used epoxy resin. In deep water exploration development of insulator for pipe is very important to ensure is an effectively reduce the cost of exploration. The insulation, mainly based on polymeric material, must withstand the high pressure, water ingress, high internal and low external temperatures.

Therefore, the syntactic foam is then in contact with water on all its surface, on the one hand cold water on the outer surface on the other hand hot water near the steel sur-

face. In this case, only the external surface of the system is in contact with water. This solution was used for example for the insulation of Bonga production steel catenary riser [31]. The material such epoxy syntactic foam hardened by an anhydride curing agent. This resin has been reinforced with sodium-borosilicate glass micro-balloons of density 0.38 g/cm<sup>3</sup> at 55% volume fraction shows at Table 1. The mechanical testing has been conducted on foams with different matrices: Polypropylene (PP), Polyurethane (PU) and Epoxy (EP). The three foams were filled with glass micro-balloons of same density 0.38 g/cm<sup>3</sup>. The samples were machined in cylindrical form with diameter 10 mm and height 10 mm. The gravimetric test or Isothermal ageing tests also performed on the samples were performed at 80°C in deionised water, in natural sea water and in relative humidity 90% in an oven. The sizes of the samples were 50 × 50 × 2 mm<sup>3</sup>. The water uptake in percentage (%mass gain) was calculated following ASTM D570 (mass gain determined on blotted dry samples normalised by the initial mass). From the gravimetric result shows that weight uptake was the highest for deionised water, whereas the sea water induced a smaller weight increase. While result concerns the water uptake in relative humidity, in this case, the weight gain is very low, not proportional to the humidity level and to the water uptake of the foam in liquid environment.

While compared the behaviour of syntactic foam with different matrices, a confined compression set-up has been used. This solicitation has been chosen to simulate the mechanical loading actually applied on the insulation coating when it is bonded onto the steel surface. The Figure 3 presents the compression curves of three syntactic foam materials, two with soft matrices (PP and PU) and one with rigid matrix (epoxy) [30]. These tests were conducted up to 250 MPa, obviously a very high loading towards service conditions, in order to know the overall behaviour of the material until rupture. After a first increase of load, one can observe

Table 1. Mechanical Properties of Several Syntactic Foams.

Reference	Matrix Materials	Micro Balloon Materials Reinforcement	Strength	Photo of Sample	
[29]	HYDREX 100® 33350 vinyl ester (density = 1100 kg/m <sup>3</sup> )	Glass S22 (outer diameter of 40 µm and a density of 220 kg/m <sup>3</sup> )	Nanoclay	Dynamic Compressive strength 73.94 MPa (strain rate 1200s <sup>-1</sup> ) Compressive Yield strength 32.53MPa	
[30]	Polypropylene (PP), Polyurethane (PU), Epoxy resin (EP)	Glass sodium-borosilicate (density 0.38 g.cm <sup>-3</sup> at 55% volume fraction)	Nanoclay	Monotonic tests, the load was increased up to 25 MPa 20 MPa for soft matrices (PU, PP)	

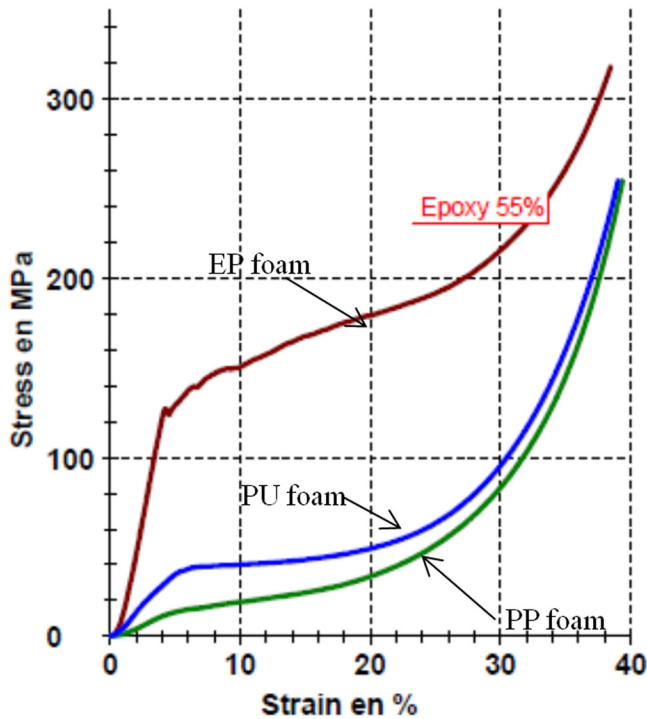


Figure 3. Compression curve for three matrix syntactic foams [30].

that there is more or less a plateau which corresponds to the rupture of the microballoons. When all the balloons are broken, there is compaction of the material and the load increases rapidly.

#### 4. COMPARISON OF MOISTURE PROPERTIES

Performance of syntactic foam was tested the ability in marine condition by using hygrothermal moisture condition. In this research [30], moisture conditioning was performed by immersing one set of specimen in salt water and another set of specimen in de-ionized water. The water absorbed was measured periodically. When variation in weight of the specimen due to moisture absorption reached less than 0.1% in 7 days (ASTM D 5229-92), it was assumed that saturation was attained [29]. Based on the results when the moisture absorption studies conducted on salt water (SW) and de-ionized (DI) water specimen, it shows that the DI water conditioned specimen had enhanced moisture intake (50% increment) when compared with their SW conditioned counterparts. The ionic species of salt water ( $\text{Na}^+$ ) is large enough to reduce diffusion rate as compared to the ionic species of de-ionized water. The variation of storage modulus with nanoclay weight fraction for SW and DI water conditioned specimen is shown in Figure 4 and Figure 5, respectively. From these figures it can be visualized that storage modulus was a constant initially, until it gradually starts sloping down. Once the material passes through the  $T_g$  (Glass transition temperature) region, an abrupt fall in the storage modulus

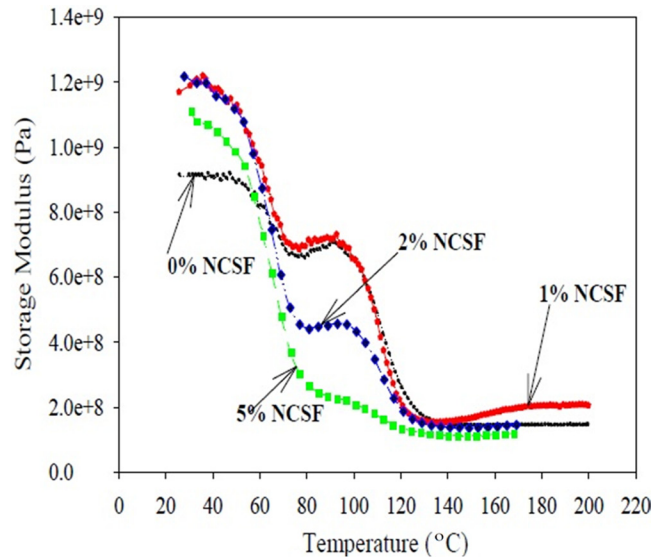


Figure 4. Variation of storage modulus for SW specimen with nanoclay weight fractions [29].

curve can be noticed. This corresponds to the softening/relaxation of polymeric chains. Thus, in a more relaxed state, the polymeric chains can be easily deformed due to the tensile loading condition employed in DMA (Dynamic Mechanical Testing) testing. From the results, the storage modulus and  $T_g$  for nanoclay reinforced syntactic foams up to 2% by weight increased when compared with their pure syntactic foam counterparts, irrespective of whether they were dry or moisture conditioned. The nano-scale distribution of clay platelets in the polymeric matrix with glass microballoons resulted in better reinforcement, and hence higher stiffness

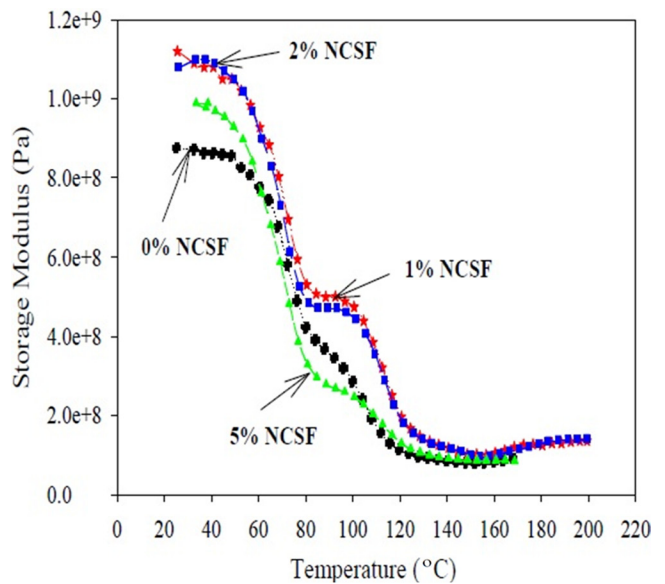


Figure 5. Variation of storage modulus of DI specimen with nanoclay weight fractions [29].

and  $T_g$  values. The reduction in storage modulus and  $T_g$  was higher for the DI water conditioned specimen compared to SW conditioned specimen. Moisture absorption resulted in deteriorating or weakening chemical bonds between polymeric chains, resulting in lower viscoelastic properties, compared to dry syntactic foams. Due to moisture absorption, the free volume of the conditioned specimen will be higher than that of the dry specimen. This swelling of the syntactic foam resulted in a reduction of  $T_g$  of the material [32].

## 5. CONCLUSIONS

From the literature review, it can be found that syntactic foams made from vinyl ester, epoxy resin, PP and PU as a matrix materials reinforced with glass microballoon are widely used in marine application. For an example vinyl ester syntactic foam subjected to salt water (SW) conditioning had less moisture absorption when compared with their de-ionised (DI) water counterparts. The compressive strength test for both static and dynamic reduced when the specimen is subjected to hygrothermal conditioning and the reduction is the highest for the de-ionised (DI) water specimen when compared with the sea water (SW) specimen. While the result use of polymers based syntactic foams reinforced with glass microballoon pipeline insulation in deep water depths a better understanding of their behaviour. There is not much improving for the ageing resistance of the syntactic foams. Compared to the mechanical testing result with various syntactic foams concluded that soft matrices material such as PP and PU exhibited as continuous and uniform damage whereas brittle EP can withstand at higher loaded but induced sudden and localise damage.

## 6. REFERENCES

- [1] <http://www.trelleborg.com/en/offshore/Markets-and-Applications/Subsea/>
- [2] N. Mills, *Polymer Foams Handbook: Engineering and Biomechanics Applications and Design Guide*. (Butterworth-Heinemann, Burlington, MA, 2007).
- [3] F. A. Shutov, "Syntactic Polymer Foams," *Advances in Polymer Science*, (1986), pp. 63–123. 3.
- [4] A. J. Hodge, "Mechanical Property Allowables Generated for the Solid Rocket Booster Composite Nose Cap," type, 2000.
- [5] A. J. Hodge, R. K. Kaul, W. M. McMahon, and T. Reinarts, "Sandwich composite, syntactic foam core based application for space structures," *45th International 11 SAMPE Symposium and Exhibition (Proceedings)* 45, (2000), pp. 2293–2300.
- [6] V. Sauvant-Moynot, N. Gimenez, and H. Sautereau, "Hydrolytic ageing of syntactic foams for thermal insulation in deep water: Degradation mechanisms and water uptake model," *Journal of Materials Science* 41(13), (2006), pp. 4047–4054. <http://dx.doi.org/10.1007/s10853-006-7618-0>
- [7] N. Gupta and E. Woldesenbet, "Hygrothermal studies on syntactic foams and compressive strength determination," *Composite Structures* 61(4), (2003), pp. 311–320. [http://dx.doi.org/10.1016/S0263-8223\(03\)00060-6](http://dx.doi.org/10.1016/S0263-8223(03)00060-6)
- [8] N. Gupta, S. Priya, R. Islam, and W. Ricci, "Characterization of mechanical and electrical properties of epoxy-glass microballoon syntactic composites," *Ferroelectrics* 345, (2006), pp. 1–12. <http://dx.doi.org/10.1080/00150190601018002>
- [9] D. Rittel, "Adiabatic shear failure of a syntactic polymeric foam," *Materials Letters* 59(14–15), (2005), pp. 1845–1848. <http://dx.doi.org/10.1016/j.matlet.2004.09.059>
- [10] N. Gupta, C. S. Karthikeyan, S. Sankaran, and Kishore, "Correlation of processing methodology to the physical and mechanical properties of syntactic foams with and without fibers," *Materials Characterization* 43(4), (1999), pp. 271–277. [http://dx.doi.org/10.1016/S1044-5803\(99\)00039-X](http://dx.doi.org/10.1016/S1044-5803(99)00039-X)
- [11] C. S. Karthikeyan, S. Sankaran, and Kishore, "Elastic behaviour of plain and fibre-reinforced syntactic foams under compression," *Materials Letters* 58(6), (2004), pp. 995–999. <http://dx.doi.org/10.1016/j.matlet.2003.08.012>
- [12] C. S. Karthikeyan, S. Sankaran, and Kishore, "Flexural behaviour of fibre-reinforced syntactic foams," *Macromolecular Materials and Engineering* 290(1), (2005), pp. 60–65. <http://dx.doi.org/10.1002/mame.200400177>
- [13] E. M. Wouterson, F. Y. C. Boey, X. Hu, and S. C. Wong, "Fracture and impact toughness of syntactic foam," *Journal of Cellular Plastics* 40(2), (2004), pp. 145–154. <http://dx.doi.org/10.1177/0021955X04041960>
- [14] E. M. Wouterson, F. Y. C. Boey, X. Hu, and S. C. Wong, "Fracture toughness and impact resistance of syntactic foam," presented at the *Annual Technical Conference—ANTEC, Conference Proceedings, 2003* (unpublished).
- [15] Kishore, R. Shankar, and S. Sankaran, "Gradient syntactic foams: Tensile strength, modulus and fractographic features," *Materials Science and Engineering A* 412(1–2), (2005), pp. 153–158. <http://dx.doi.org/10.1016/j.msea.2005.08.017>
- [16] M. Koopman, K. K. Chawla, K. B. Carlisle, and G. M. Gladysz, "Microstructural failure modes in three-phase glass syntactic foams," *Journal of Materials Science* 41(13), (2006), pp. 4009–4014. <http://dx.doi.org/10.1007/s10853-006-7601-9>
- [17] L. Bardella, "Discussion on the paper "Simulation of porosity by microballoon dispersion in epoxy and urethane: Mechanical measurements and models" by M. A. El-Hadek and H. V. Tippur, *Journal of Materials Science*, 37, 1649–1660, 2002, [1]," *Journal of Materials Science Letters* 22(22), (2003), pp. 1643–1646. <http://dx.doi.org/10.1023/A:1026313314513>
- [18] G. M. Gladysz, B. Perry, G. McEachen, and J. Lula, "Three-phase syntactic foams: Structure-property relationships," *Journal of Materials Science* 41(13), (2006), pp. 4085–4092. <http://dx.doi.org/10.1007/s10853-006-7646-9>
- [19] N. Gupta, E. Woldesenbet, and P. Mensah, "Compression properties of syntactic foams: Effect of cenosphere radius ratio and specimen aspect ratio," *Composites Part A: Applied Science and Manufacturing* 35(1), (2004), pp. 103–111. <http://dx.doi.org/10.1016/j.compositesa.2003.08.001>
- [20] B. John, C. Nair, K. Devi, and K. Ninan, "Effect of low-density filler on mechanical properties of syntactic foams of cyanate ester," *Journal of Materials Science* 42(14), (2007), pp. 5398–5405. <http://dx.doi.org/10.1007/s10853-006-0778-0>
- [21] H. Mae, M. Omiya, and K. Kishimoto, "Effects of strain rate and density on tensile behavior of polypropylene syntactic foam with polymer microballoons," *Materials Science and Engineering: A*, In Press, Corrected Proof, doi:10.1016/j.msea.2007.05.028. <http://dx.doi.org/10.1016/j.msea.2007.05.028>
- [22] C. G. Papakonstantinou, J. W. Giancaspro, and P. N. Balaguru, "Fire response and mechanical behavior of polysialate syntactic foams," *Composites Part A: Applied Science and Manufacturing*, In Press, Corrected Proof, doi:10.1016/j.compositesa.2007.08.029. <http://dx.doi.org/10.1016/j.compositesa.2007.08.029>
- [23] D. Ray and R. Gnanamoorthy, "Friction and wear behavior of vinyl-ester resin matrix composites filled with fly ash particles," *Journal of Reinforced Plastics and Composites* 26(1), (2007), pp. 5–13. <http://dx.doi.org/10.1177/0731684407069945>

- [24] D. Ray, D. Bhattacharya, A. K. Mohanty, L. T. Drzal, and M. Mishra, "Static and dynamic mechanical properties of vinylester resin matrix composites filled with fly ash," *Macromolecular Materials and Engineering* 291(7), (2006), pp. 784–792. <http://dx.doi.org/10.1002/mame.200600097>
- [25] Gupta, N.; Karthikeyan, C.S.; Sankaran, S.; Kishore, Correlation and Processing Methodology to the Physical and Mechanical Properties of Syntactic Foams with and without Fibers, *Materials Characterization*, 43(1999) 271–277. [http://dx.doi.org/10.1016/S1044-5803\(99\)00039-X](http://dx.doi.org/10.1016/S1044-5803(99)00039-X)
- [26] Karthikeyan, C.S.; Sankaran, S.; Kumar, M.N.J.; Kishore, Processing and Compressive Strengths of Syntactic Foams with and without Fibrous Reinforcement, *Journal Applied Polymer Science*, 81(2001) 405–411. <http://dx.doi.org/10.1002/app.1452>
- [27] Bledzki AK, Mamun AA, Jazskiewicz A, Volk J. PLA composites reinforced by wheat and rye husk. In: *ANTEC@NPE conference proceedings, Chicago, USA*; 2009.
- [28] White NM, Ansell MP. Straw reinforced polyester composites. *J Mater Sci* 1993;18:1549–56. <http://dx.doi.org/10.1007/BF01111977>
- [29] B. Demissie, M. John, E. Woldesenbet, High Strain Rate Behaviour of Hydrothermally conditions syntactic foams for marine application: Conference proceeding 18th International Conference on Composite Materials Edinburgh Scotland 2009.
- [30] François Grosjean, Nadège Bouchonneau, Dominique Choqueuse and Valérie Sauvant-Moynot, Comprehensive analyses of syntactic foam behaviour in deepwater environment *Journal of Materials Science March 2009, Volume 44, Number 6* : Pages 1462-1468. <http://dx.doi.org/10.1007/s10853-008-3166-0>
- [31] Okonkwo U., Uralil F., Berti E., Judd S., *Proceedings of Deep Off-shore Technology, Vitoria*, November 2005.
- [32] A. Haque and M.K. Hossain. 2003. Effects of moisture and temperature on high strain rate behavior of S2-glass-vinyl ester woven composites, *J. Compos. Mater.*, 37: 627–647. <http://dx.doi.org/10.1177/002199803029732>



## A Novel Controlled Fatigue Technique to Increase Cement Paste Permeability

J. GOLDMAN<sup>1</sup>, CHUN-YANG YIN<sup>2,\*</sup> and XI CHEN<sup>3,4</sup>

<sup>1</sup>Market and Social Systems Engineering, University of Pennsylvania, Philadelphia, PA 19104, USA

<sup>2</sup>Chemical and Analytical Sciences, Murdoch University, Murdoch, 6150 WA, Australia

<sup>3</sup>Columbia Nanomechanics Research Center, Department of Earth and Environmental Engineering, Columbia University, New York, NY 10027-6699, USA

<sup>4</sup>International Center for Applied Mechanics, SV Lab, School of Aerospace, Xi'an Jiaotong University, Xi'an 710049, China

### KEYWORDS

controlled fatigue technique  
concrete/mortar paste  
permeability  
crack formation

### ABSTRACT

In this study, a novel approach using low-load cyclic compression fatigue technique to gradually propagate cracks in a brittle porous material and enhance fluid flow in a controlled direction was investigated. The technical feasibility of using this technique to increase permeability was evaluated by conducting cyclic fatigue, hydraulic conductivity, and crack formation tests. The technique could be used to gradually propagate crack(s) in a controlled direction, and increase permeability in a porous and brittle material. The method improves the conventional counterpart of hydraulic fracture by inducing controlled damage formations, without suddenly compromising the structural integrity of the material, thereby manipulating permeability. The highest permeability recorded is  $4.25 \times 10^{-9}$  m/s for 1,000 fatigue cycles. The results could have important implications for enhancing the capabilities of liquid CO<sub>2</sub> sequestration in deep sea sediments.

© 2014 DEStech Publications, Inc. All rights reserved.

### 1. INTRODUCTION

In conventional engineering areas, permeability has been related to the wear and deterioration of brittle materials, mainly through the formation of cracks. High permeability is highly undesirable since it reduces structural integrity. Nonetheless, for other applications such as liquid carbon dioxide (CO<sub>2</sub>) sequestration in deep-sea sediments, the presence of highly permeable pores in the sediments is vital. This is because the pores have to be sufficiently interconnected to enable diffusion of liquid CO<sub>2</sub> into the sediments while at the same time, provide a physical barrier from ocean currents to prevent release of the liquid CO<sub>2</sub> into the ocean [1]. Liquid CO<sub>2</sub> injected into deep-sea sediment directly below the seafloor will be stored safely because of gravitational stability [2]; however, the current bottleneck of such a technique is that despite of the large porosity (~70%) of the sediment, the available volume for CO<sub>2</sub> diffusion is

very small since the microstructure of the sediment is analogous to a closed-cell foam, with an extremely low permeability. In order to take advantage of the promising potential of deep sea sediment for CO<sub>2</sub> sequestration, permeability of porous brittle material (e.g. sediment) must be increased in a controllable manner.

For porous brittle materials such as rocks, hydraulic fracturing is regarded as a conventional technique to interconnect pores and increase permeability by creating cleavage cracks [3]. However, the large uncontrolled force of hydraulic fracturing will shatter deep-sea sediment in a non-direction specific manner. This could create conduits linking to the seafloor surface allowing the CO<sub>2</sub> to escape [3]. Motivated by the above considerations, we propose the new concept of “controlled fatigue”, may be employed to gradually propagate microcracks in a controlled direction and increase permeability gradually without shattering the sediments; it involves much smaller pressure than hydraulic fracture and thus more practical for deep-sea objects.

This study investigates the feasibility of using a low load

\*Corresponding author. Email: [c.yin@murdoch.edu.au](mailto:c.yin@murdoch.edu.au)

cyclic compression technique to gradually propagate cracks in a model porous brittle material, and subsequently enhance fluid flow in a controlled direction. Porous cement paste is used as a simulant of deep-sea sediment, which shares a similar porous microstructure. To successfully employ this technique, mechanical (elastoplastic) property measurement and fracture toughness measurement using microindentation tests are first carried out. These experiments set the basis for parameters to be used in cyclic fatigue test. The permeability of porous samples is measured after a number of fatigue tests, and the permeability is correlated to load magnitude, number of cycles, and characteristics of microcracks. The study provides useful insights regarding the possibility of utilization of controlled fatigue technique to increase permeability in a simulated sea-bed sediment structure. Findings from this research can aid in providing a precursory and complementary structural data for future studies involving dynamics and controlled movement of liquid CO<sub>2</sub> within sediment pores.

## 2. MATERIALS AND METHODS

### 2.1. Material

Fast-setting cement with high homogeneity was mixed with water (3 quarts of water per 50 lb cement mix) and cast into cylindrical shapes (1-cm radius; 2.5 cm in length). In a sense, this was done to impart mortar/paste-like properties to the cement mix which had comparatively lower strength and higher elasto-plasticity, so as to provide better simulation of the stiffness and strength of deep-bed sediment. The samples were placed on top of a glass plate, vibrated for three minutes to allow some air bubbles to escape and allowed to dry for 24 hours. After the drying process, the samples were removed from the tubing. During the fast setting process, sub-mm sized air bubbles were trapped inside the concrete, forming closed-cell foam-like microstructure.

### 2.2. Indentation

Any mechanical integrity test (e.g. fatigue) needs to be preceded by mechanical property characterization, such that the correct boundaries of the failure test can be set. For a porous brittle material, the determination of its elastoplastic properties and fracture toughness could set the useful limits of the load magnitude to be used in the subsequent cyclic experiment. Microindentation test [4] is a versatile technique that can be employed to quickly and effectively measure a variety of mechanical properties, and it is employed in the current study. During this technique, a rigid indenter is pressed into and then unload from a specimen (in a quasi-static manner), and the indentation force-depth penetration history is continuously recorded. The reverse analysis of such data allows the determination of material properties.

For indentation tests, a Vickers tip (four-sided pyramid with 136° between opposite sides, precision machined AISI 4340 steel) was installed on an Instron 4206 with a loading rate of 0.005 inches/minute. Indentation load,  $P$  and displacement,  $\delta$  were measured continuously. The classic indentation theory [Equations (1) and (2)] [5] was used to relate Young's modulus,  $E$  and yield strength,  $\sigma_y$ , to the indentation hardness,  $H$  and contact stiffness,  $S$  where

$$S = dP / d\delta \Big|_{\delta=\delta_m}^{unloading}$$

(slope of the initial portion of unloading indentation force-displacement,  $P - \delta$  curve) obtained from a single indentation test.

$$H = \frac{P}{A} = c_b \sigma_y \quad (1)$$

$$S = \gamma B \frac{2}{\sqrt{\pi}} \bar{E} \sqrt{A} \quad (2)$$

The plane-strain modulus,  $\bar{E}$  in Equation (2) is

$$\bar{E} \equiv E / (1 - \nu^2) \quad (3)$$

with  $\nu$  the Poisson's ratio. The constant  $c_b$  is a constraint factor approximated at 2.9 for elastic-perfectly plastic materials [6,7] (which is a reasonable assumption for brittle materials). The projected contact area  $A = \pi a^2$ , where  $a$  was the projected contact radius whose first order approximation is  $a = \tan(70.3^\circ) \cdot \delta$ . The mechanical property measurements were carried out at low-indentation loads to avoid cracking.

When measuring the fracture toughness, higher indentation load is employed to initiate a crack. Upon Vickers indentation, the radial crack is initiated from the corner of the pyramidal impression and the crack length can be correlated to the material elastoplastic properties (measured above) and maximum load force, according to the following equation [8]:

$$\frac{K_c}{\sigma_y \sqrt{a}} = 0.129 \left( \frac{c}{a} \right)^{-3/2} \left( \frac{E}{\sigma_y} \right)^{2/5} \quad (4)$$

where  $c$  is the length of the radial crack, and  $K_c$  is the mode-I stress intensity factor.

### 2.3. Cyclic Fatigue

The dried cement paste (DCP) samples were first subjected to a compression test on the Instron 4206 to determine the crush load,  $P_{crush}$ , which sets the upper bound of the subsequent cyclic compressive loading ( $P_{max} = 1200$  lbs and  $P_{min} = 0$  lbs) at a frequency of 0.5 Hz until failure. The number of cycles until failure was counted. The total number

of cycles was divided into intervals (200 cycles) for cyclic fatigue. The longest crack on each sample and the number of surface cracks on each sample were measured after each interval of cyclic fatigue.

### 2.4. Permeability Tests

Hydraulic conductivity ( $K$ ), a form of permeability, is the ease at which water can move through pore spaces or fractures. A falling head apparatus was developed to determine permeability ( $K$ ) according to the following Darcy equation [9]:

$$K = \frac{aL}{At} \ln \frac{\Delta h_0}{\Delta h(t)} \quad (5)$$

The DCP samples were wrapped with Teflon tape and inserted into plastic tubes to prevent water leaking and air interference.  $L$  and  $A$  were the height (cm) and cross-sectional area (cm<sup>2</sup>) of the DCP sample, respectively. The outer diameter of the samples was equivalent to the inner diameter of the steel tubes to enable exact fit. A plastic tube with cross-sectional area (inner diameter)  $a$  (cm<sup>2</sup>) was inserted into a drilled hole in a rubber stopper and sealed with watertight silicone epoxy. This tube was filled with water via suction and its top end was subsequently sealed to prevent water exit. The whole setup was placed on top of the sample with the end of plastic tube contacting the sample. The test was initiated when the top end seal was released and time was recorded.  $\Delta h_0$  was the water height at the beginning of the test ( $m$ ) while  $\Delta h(t)$  was the water height at time  $t$  (sec). By using Equation (5), the steady-state permeability of the DCP samples was determined.

## 3. RESULTS AND DISCUSSION

### 3.1. Overview of Hydraulic Fatigue

A visual overview of experimental techniques and applications demonstrates the investigation of hydraulic fatigue as shown in Figure 1. The objective is to demonstrate how hydraulic fatigue can be used to control fluid flow in a specific direction as used for environmental and energy applications. This study includes numerous interconnected elements. First, low load indentation and high load indentation are used to calculate the material properties and fracture properties respectively. These material and fracture characteristics are used to set the cyclic fatigue load. The relationship between cyclic fatigue and permeability is then investigated. After intervals of cyclic loading, the crack length, crack number, crack direction and permeability were measured. Permeability varies depending upon microstructure and the resulting crack length and direction from cyclic fatigue.

### 3.2. Indentation

Indentation was used to determine the material elastoplastic properties [10,11]. The Young’s modulus and yield stress of DCP were determined to be 1 GPa and 30 MPa respectively. The low Young’s modulus value is expected since we have customized the mixture to simulate a dried paste-like material. Although any cyclic load will create cracks and increase permeability, the fracture toughness is needed to determine the range of successful cyclic forces for the propagation of a controlled crack. The determined crack length is correlated with the stress intensity factor

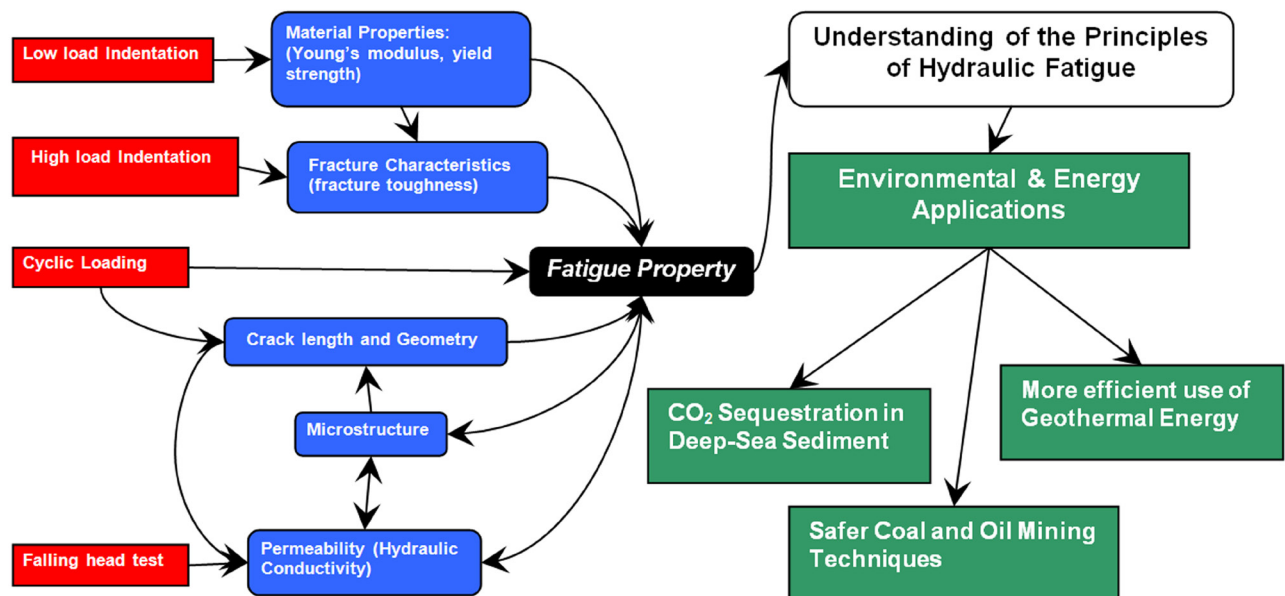


Figure 1. Elements of hydraulic fatigue and its applications.

(SIF) at the crack front and material elastoplastic properties via explicit relationships, from which a reverse analysis can be carried out such that the critical SIF (fracture toughness) can be readily derived once the crack length is measured [8]. From the measured crack length, the fracture toughness was calculated to be  $0.01 \text{ MPa m}^{1/2}$ , typical for a chalk-like brittle material. It is important to note that the fracture toughness of seabed sediment may be higher and thus different ranges of cyclic loads may be applied in that case.

### 3.3. Cyclic Fatigue and Crack Formation

The average increase of permeability ( $K$ ) for 200 cycles of cyclic compression at 1200 lbs is  $3.94 \times 10^{-10} \text{ m/s}$  per 200 cycles with the highest permeability recorded is approximately  $4.25 \times 10^{-9} \text{ m/s}$  for 1,000 cycles. This value is compared with permeability of stressed and unstressed concrete ( $< 5 \times 10^{-10} \text{ m/s}$ ) reported by Banthia *et al.* [12] and ordinary Portland cement-based concrete ( $< 1 \times 10^{-11} \text{ m/s}$ ) reported by Chindaprasirt *et al.* [13]. This provides an initial indication of the effectiveness of cyclic fatigue to increase permeability of brittle material.

Figure 2 shows the effect of the number of fatigue cycles on samples 1, 2 and 3, respectively. At the beginning of the cyclic loading, hydraulic conductivities for all three samples are approximately the same. The average increase of hydraulic conductivity for the three samples is  $3.64 \times 10^{-9} \text{ m/s}$  for 1000 cycles of cyclic fatigue. Sample 1 exhibits a significant increase in hydraulic conductivity at the end of 1,000 cycles ( $\approx 1550\%$ ) compared to samples 2 ( $\approx 650\%$ ) and 3 ( $\approx 550\%$ ). The linear fit of hydraulic conductivities of both samples 2 and 3 (not shown) shows a direct relationship with gradient of curve =  $1.66 \times 10^{-12} \text{ m/s/cycle}$  and a residual sum of

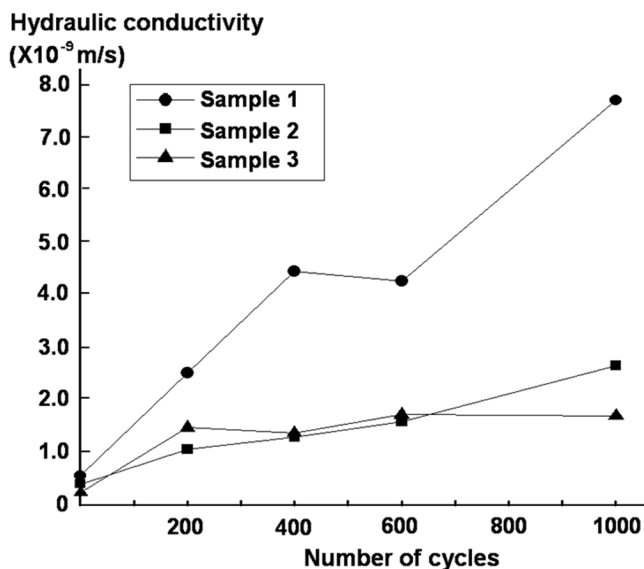


Figure 2. Effect of the number of fatigue cycles on hydraulic conductivity for samples 1, 2 and 3.

squares (RSS) =  $9.76 \times 10^{-19}$ . It is postulated that the significant increase in hydraulic conductivity at the end of 1,000 cycles for sample 1 is attributed to its higher porosity as a result of variation caused during the cement mixing stage. At this point, it is to be noted that this variation is deliberate to simulate the variation in porosity of deep-sea sediment.

Figure 3 shows the effect of the number of fatigue cycles on crack length of samples 1, 2 and 3. Crack length increases at a faster rate from 600 cycles onwards for samples 1 and 2. The average surface crack length after 1000 cycles is 1.63 cm. In general, cracks allow the flow of fluid and increase hydraulic conductivity. The samples with longer cracks should therefore yield greater hydraulic conductivity measurements. The linear fit of effect of crack length on hydraulic conductivity (Figure 4) shows a direct relationship with gradient of curve =  $2.26 \times 10^{-9} \text{ ms}^{-1}/\text{cm}$  and a residual sum of squares (RSS) =  $1.14 \times 10^{-17}$ . This shows a link between crack length and hydraulic conductivity. If the sample is sufficiently large, hydraulic conductivity should increase non-linearly with number of cycles of cyclic fatigue.

Unidirectional crack formation ensures control over the direction of fluid flow. All cyclic fatigue loads yielded small cracks that are essentially parallel to the direction of cyclic compression, indicating controlled pore formation. For comparison purpose, crush fracture technique with a large quasi-static compressive load was also conducted on a sample. Figure 5 illustrates the difference between crack formations induced by fatigue and fracture. It is obvious that the conventional fracture technique shatters the sample completely, allowing fluid flow but nonetheless creates an unstable condition and renders the sample structurally unsound. This is an indication that controlled fatigue is a significantly better technique in increasing permeability of sea-bed sediment-

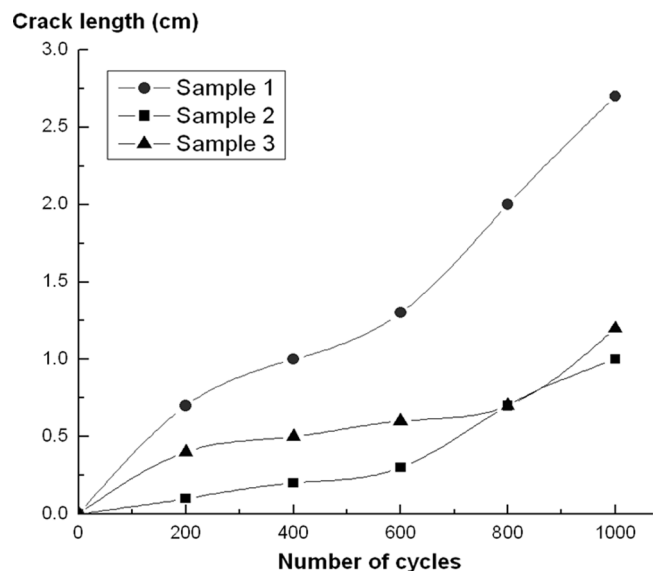


Figure 3. Effect of the number of fatigue cycles on crack length of samples 1, 2 and 3.

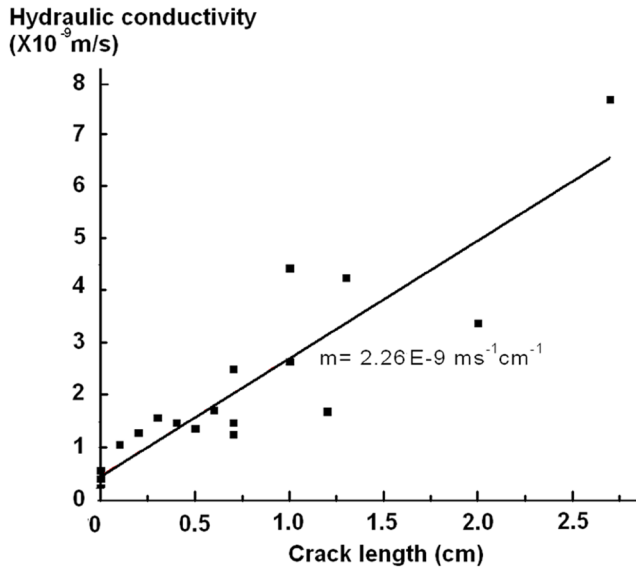


Figure 4. Linear fit of effect of crack length on hydraulic conductivity.

alike specimens than hydraulic fracture. A closer inspection reveals that the substantially smaller cracks induced by controlled fatigue may be much more favourable in preventing permeation of liquid CO<sub>2</sub> out into the ocean.

#### 4. CONCLUSIONS

It is shown from the present preliminary study that cyclic fatigue can be used to gradually propagate a crack in a controlled direction and increase permeability in a porous and brittle material. This represents a novel approach which improves upon the conventional method of hydraulic fracture by inducing controlled pore formations without compromising the structural integrity of the material. Thus, controlled fatigue shows potential in its usage as part of liquid CO<sub>2</sub>

sequestration initiatives since it is capable of creating and propagating substantially smaller cracks in model brittle materials, increasing permeability in a tailored manner, and the crack extension direction can be controlled. Data obtained from this study can shed some light for future studies involving dynamics and tailored movement of liquid CO<sub>2</sub> within deep sea sediment pores. Future studies include a more systematic understanding of crack characteristics (e.g. crack length, density, crack tip opening) with cyclic load, and correlate that with permeability of CO<sub>2</sub> through a predictive theoretical model.

#### REFERENCES

- [1] Goldberg, D., "CO<sub>2</sub> sequestration beneath the seafloor: evaluating the in situ properties of natural hydrate-bearing sediments and oceanic basalt crust," *Proc. 3rd International Conference on Materials Engineering for Resources* (1999).
- [2] House, K.Z., Schrag, D.P., Harvey, C.F. and Lackner, K.S., "Permanent carbon dioxide storage in deep-sea sediments," *Proc. Natl. Acad. Sci. USA* 103, 12291–12295 (2006). <http://dx.doi.org/10.1073/pnas.0605318103>, PMID:16894174 PMCid:PMC1567873
- [3] Levine, J.S., Matter, J.M., Goldberg, G., Cook, A., and Lackner, K.S., "Gravitational trapping of carbon dioxide in deep-sea sediments: permeability, buoyancy and geomechanical analysis," *Geophys. Res. Lett.* 34, L24703 (2007). <http://dx.doi.org/10.1029/2007GL031560>
- [4] Pharr, G.M., "Measurement of mechanical properties by ultra-low load indentation," *Mater. Sci. Eng. A* 253, 151–159 (1998). [http://dx.doi.org/10.1016/S0921-5093\(98\)00724-2](http://dx.doi.org/10.1016/S0921-5093(98)00724-2)
- [5] Oliver, W.C., and Pharr, G.M., "Improved technique for determining hardness and elastic modulus using load and displacement sensing indentation experiments," *J. Mater. Res.* 7, 1564–1580 (1992). <http://dx.doi.org/10.1557/JMR.1992.1564>
- [6] Johnson, K.L., [Contact mechanics], Cambridge University Press, (1985).
- [7] Chen, X., Ogasawara, N., Zhao, M., and Chiba, N., "On the uniqueness of measuring elastoplastic properties from indentation: the indistinguishable mystical materials," *J. Mech. Phys. Solids* 55, 1618–1660 (2007). <http://dx.doi.org/10.1016/j.jmps.2007.01.010>
- [8] Tang, Y., Yonezu, A., Ogasawara, N., Chiba, N., and Chen, X., "On radial crack and half-penny crack induced by Vickers indenta-

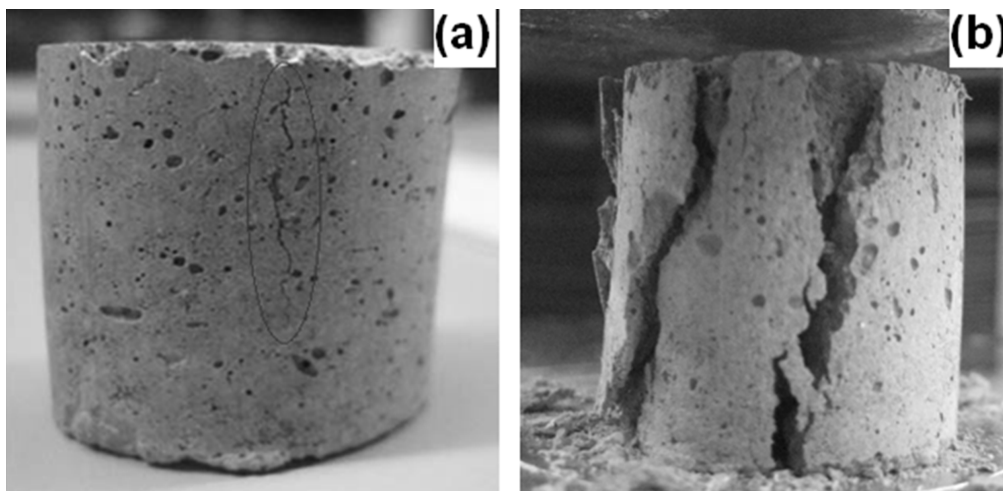


Figure 5. Comparison of crack formation between controlled cyclic fatigue (a) and hydraulic fracture (b).

- tion,” *Proc. Royal. Soc. A* 464, 2967–2984 (2008). <http://dx.doi.org/10.1098/rspa.2008.0077>
- [9] Banthia, N., Pigeon, M., Marchand, J., and Boisvert, J., “Permeability of roller compacted concrete,” *ASCE J. Mater. Civ. Eng.* 4, 27–40 (1992). [http://dx.doi.org/10.1061/\(ASCE\)0899-1561\(1992\)4:1\(27\)](http://dx.doi.org/10.1061/(ASCE)0899-1561(1992)4:1(27))
- [10] Chen, X., Hutchinson, J.W., and Evans, A.G., “The mechanics of indentation induced lateral cracking,” *J. Am. Ceram. Soc.* 88, 1233–1238 (2005). <http://dx.doi.org/10.1111/j.1551-2916.2005.00281.x>
- [11] Ogasawara, N., Chiba, N., and Chen, X., “Limit analysis-based approach to determine the material plastic properties with conical indentation,” *J. Mater. Res.* 21, 947–957 (2006). <http://dx.doi.org/10.1557/jmr.2006.0108>
- [12] Banthia, N., Biparva, A., and Mindess, S., “Permeability of concrete under stress,” *Cement Conc. Res.* 35, 1651–1655 (2005).
- [13] Chindapasirt, P., Homwuttiwong, S., and Jaturapitakkul, C., “Strength and water permeability of concrete containing palm oil fuel ash and rice husk–bark ash,” *Const. Build. Mater.* 21, 1492–1499 (2007). <http://dx.doi.org/10.1016/j.conbuildmat.2006.06.015>



## Micromechanics-based Study on Thermo-mechanical Behavior of ZrO<sub>2</sub>/Ti Functionally Graded Materials

HIDEAKI TSUKAMOTO\*, YOSHIKI KOMIYA, HISASHI SATO and YOSHIMI WATANABE

Graduate School of Engineering, Nagoya Institute of Technology, Gokiso-cho, Showa-ku, Nagoya, Aichi, 466-8555, Japan

### KEYWORDS

mean-field micromechanics  
functionally graded materials (FGMs)  
spark plasma sintering (SPS)  
Ti-ZrO<sub>2</sub> composites

### ABSTRACT

The aim of this study is to investigate thermo-mechanical response of ZrO<sub>2</sub>/Ti functionally graded materials (FGMs) fabricated by spark plasma sintering (SPS) based on a mean-field micromechanics model, which takes account of micro-stress relaxation due to interfacial diffusion between ceramic and metal phases as well as creep of both phases. A resistance to cyclic thermal shock loadings of FGMs with different compositional gradation patterns including Ti-rich, linear and ZrO<sub>2</sub>-rich gradation patterns has been investigated. The results demonstrate that Ti-rich FGMs show superior properties among the tested FGM samples. Mean-field micromechanics-based examinations reveal that the range and ratio of thermal stresses in ZrO<sub>2</sub> surface layers in FGMs can affect cyclic thermal shock fracture behaviour but not mean thermal stresses. Creep of ZrO<sub>2</sub> have a large influence on dependence of the range and ratio of thermal stresses in ZrO<sub>2</sub> surface layers on compositional gradation patterns in the FGMs.

© 2014 DEStech Publications, Inc. All rights reserved.

## 1. INTRODUCTION

Ti-ZrO<sub>2</sub> composites are to be high-temperature materials applied to aerospace and automobile structures. ZrO<sub>2</sub> has superior thermal and mechanical properties, which satisfies thermal barrier functions. One of superior mechanical properties of ZrO<sub>2</sub> is high fracture toughness due to stress-induced transformation from tetragonal (t-) ZrO<sub>2</sub> to monoclinic (m-) ZrO<sub>2</sub> under some stress conditions, which leads to enhancement of fracture toughness of other ceramics and ceramic matrix composites [1]. It is also stated that mechanical properties of ZrO<sub>2</sub> can be enhanced by incorporating Ti. Weber *et al.* [2] reported that sintered ZrO<sub>2</sub> crucibles containing 15 at% Ti showed superior strength and thermal shock resistance. Arias [3] also found that the thermal shock resistance and strength of ZrO<sub>2</sub> with 15 mol % Ti were increased due to the inhabitation of grain growth of ZrO<sub>2</sub> by Ti during sintering processes at 1850°C. In their research, they concluded that these phenomenon were related to dissolution of oxygen atom into Ti to form titanium oxides

without taking into account possible reactions between Ti and ZrO<sub>2</sub>.

Functionally graded materials (FGMs) are advanced multi-phase composites that are engineered to have a smooth spatial variation of material constituents. This variation results in an inhomogeneous structure with smoothly varying thermal and mechanical properties [4,5]. In the past decade, ZrO<sub>2</sub>/Ti FGMs have been of high potential as thermal barrier coating (TBC) structures in aerospace industries. Several studies have been conducted investigating the phase transformation of ZrO<sub>2</sub> caused by thermal stresses generated in FGMs [6,7]. Teng *et al.* [7] showed that only  $\alpha$ -Ti, tetragonal (t-) ZrO<sub>2</sub>, and monoclinic (m-) ZrO<sub>2</sub> were found in various Ti-ZrO<sub>2</sub> composites after annealing from 1400 to 1650°C. It was reported that the volume fraction of m-ZrO<sub>2</sub> increased with Ti content in Ti-ZrO<sub>2</sub> composites, while the interfacial stresses, arising from plastic deformation of Ti and thermal expansion mismatch of Ti and ZrO<sub>2</sub>, were driving forces for phase transformation from t-ZrO<sub>2</sub> to m-ZrO<sub>2</sub>. The interfacial reaction between Ti and ZrO<sub>2</sub> in FGMs has been also studied so far [8]. Thermodynamic analysis is essential for chemical design of Ti-ZrO<sub>2</sub> composites [8,9]. It was reported that

\*Corresponding author. Email: [tsukamoto.hideaki@nitech.ac.jp](mailto:tsukamoto.hideaki@nitech.ac.jp)

the standard Gibbs free energy of  $\text{Ti}_2\text{O}$  plays an important role in the thermodynamic assessment of Ti– $\text{ZrO}_2$  system, in which the formation of  $\text{Ti}_2\text{O}$  is easier than that of the other titanium oxides [9].

In many applications, FGMs can be exposed to constant or alternating thermal loading with a high temperature gradient from one side to the other. Thermal shock resistance, thermal fatigue characteristics, temperature profile have been targets of research so far. There are several theoretical, analytical and experimental studies investigating thermo-mechanical behaviour of FG TBCs subject to thermal shock loadings [10–14]. For the theoretical and analytical studies, Jin *et al.* [11,12] investigated the effect of thermal property gradients on edge cracking in FGM TBCs subject to thermal shock loadings. Wang *et al.* [13] calculated transient temperature fields and associated thermal stresses in FG TBCs by a finite element/finite difference method. Thermal shock fracture of a FGM plate was analysed when the plate is suddenly exposed to an environmental medium of a different temperature. Experimental works have been also conducted to investigate the thermal shock fracture behaviour of FG TBCs [14–16]. The works by Kokini *et al.* [14] and Han *et al.* [15] identified that vertical cracks were possibly generated in ceramic surface layers in FG TBCs. Hamatani *et al.* [16] investigated effects of compositional gradation profiles and coating densities in FG TBCs on the thermal shock resistance. There have been not so many studies examining resistances to fracture of FGMs subject to cyclic thermal shock loadings.

In this study, cyclic thermal shock fracture behaviour of  $\text{ZrO}_2/\text{Ti}$  FGMs fabricated by spark plasma sintering (SPS) has been investigated. The effect of compositional gradation patterns on cyclic thermal shock fracture of FGMs has been examined based on a mean-field micromechanics-based model. The thermal stress states in the FGMs have been estimated and some parameters to understand cyclic thermal shock fracture behaviour of the FGMs have been introduced. The influence of creep of  $\text{ZrO}_2$  on thermal stress states has been also examined.

## 2. EXPERIMENTAL PROCEDURES

### 2.1. Fabrication

The starting powders were  $\text{ZrO}_2$  partially-stabilized by 3 mol %  $\text{Y}_2\text{O}_3$ . The average diameter of  $\text{ZrO}_2$  powder is 26 nm, and that of Ti powder is less than 45  $\mu\text{m}$ . The SPS was conducted in vacuum at 1400°C under the uniaxial pressure of 30 MPa with the time duration of 20 minutes. The sintered FGM samples have a diameter of 20 mm and thickness of 9 mm, in which the FGM part has a thickness of 3 mm and Ti substrate part has that of 6 mm. The FGM part consists of 6 composite layers with different compositions according to predetermined compositional gradation

patterns of the FGMs. Step-wised compositional gradation patterns are parametrically described using the following expression [5,17].

$$f_m(i) = 1 - f_c(i) = (i-1)^n / (P-1)^n \quad (1)$$

where,  $f_m(i)$  and  $f_c(i)$  are the volume fractions of metal (Ti) and ceramics ( $\text{ZrO}_2$ ) phases in the  $i$ -th sub-layer, respectively.  $P$  is the total number of sub-layers, which have the thickness of 0.5 mm for each in the FGM part. The exponent,  $n$ , is a parameter characterizing the compositional gradation pattern. For the gradation parameter  $n$ ,  $n = 1$  means the linear compositional gradation,  $n > 1$  means the ceramic-rich gradation and  $n < 1$  means the metal-rich gradation. In this study, FGM samples with three different compositional gradation patterns of  $n = 0.5$ , 1 and 2 were fabricated to investigate the effects of compositional gradation patterns on the microstructure and thermo-mechanical properties. Figure 1 shows the compositional gradation patterns used in this study.

### 2.2. Property Characterization

A microstructure observation was conducted using optical microscope (OM) and scanning electron microscope (SEM, JSM-5900LV, JEOL, Japan) with an acceleration voltage of 15 kV. The microscope samples were prepared with sintered FGM samples embedded into the resin and mechanically polished using alumina powders.

The X-ray diffraction (XRD) investigation was performed with Cu  $K\alpha$  radiation using the Rigaku XRD meter. The  $2\theta$  was measured from 10° to 90° in a step of 0.02° with a scan speed of 2°/min. Micro-Vickers hardness tests were conducted with Shimadzu Micro-Vickers Tester at room temperature (R.T.).

Cyclic thermal shock tests were conducted on the samples of  $\text{ZrO}_2/\text{Ti}$  FGMs with  $n = 0.5$ , 1 and 2 using the testing

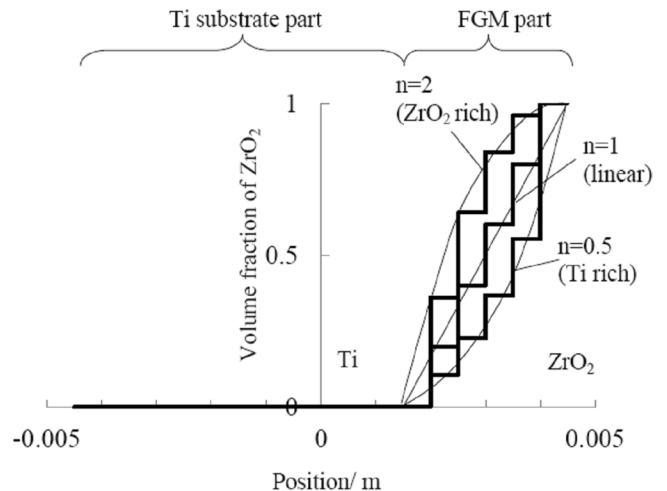


Figure 1. Compositional gradation patterns of FGMs.

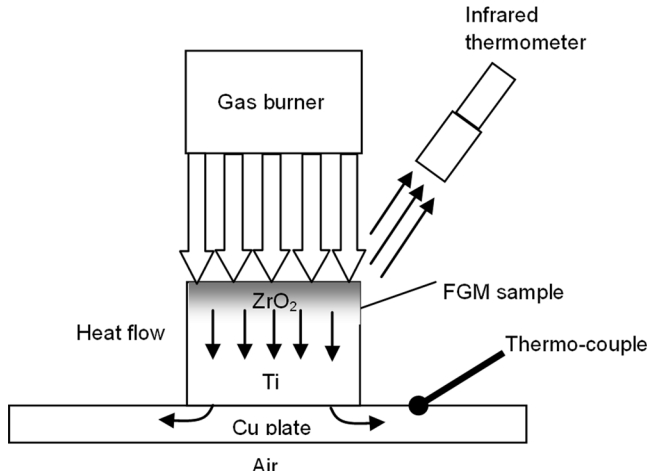


Figure 2. Set-up of thermal shock tests with FGM samples.

set-ups shown in Figure 2. The profile of temperature of the  $ZrO_2$  surface for one cycle used in the experiments is shown in Figure 3. The observation of  $ZrO_2$  surface by OM and micro-Vickers hardness test were conducted after every cyclic thermal shock loading (until the 4th cycle).

### 3. EXPERIMENTAL RESULTS

The fabricated FGMs were investigated on microstructure and thermo-mechanical behaviour under cyclic thermal shock loading conditions. The FGM sample appearance is shown in Figure 4. The sample dimensions are as described above. Figure 5 shows the SEM (backscattered electron) low and high magnification images of  $ZrO_2/Ti$  FGMs with compositional gradation patterns of  $n = 1$ . The high magnification image is accompanied with EDS point analysis data. It is seen that the compositions of  $ZrO_2$  and Ti vary

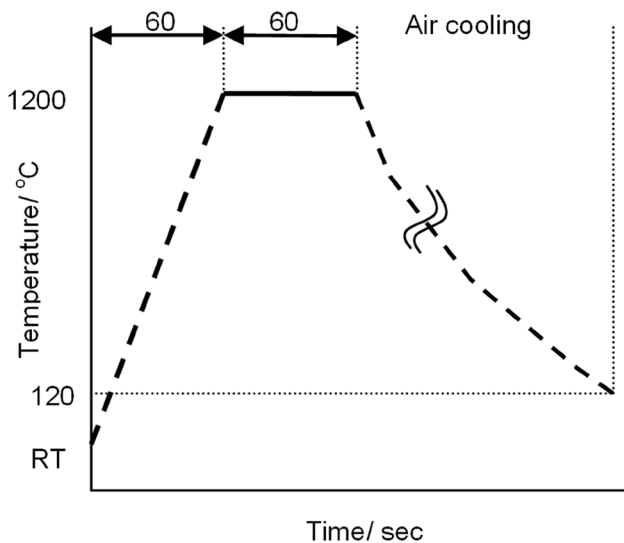
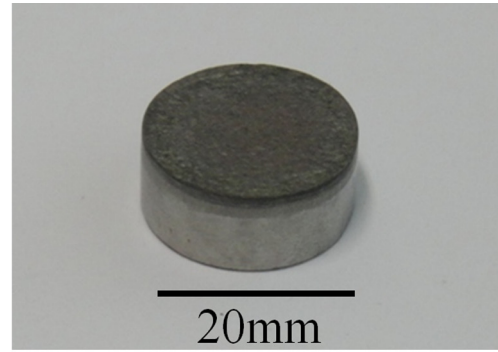
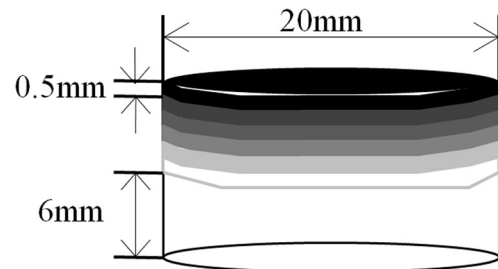


Figure 3. Profile of temperature of  $ZrO_2$  surfaces under thermal shock loading conditions.



(a)



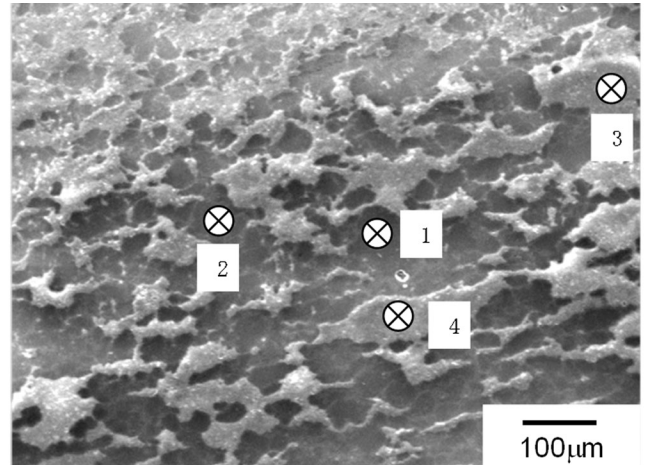
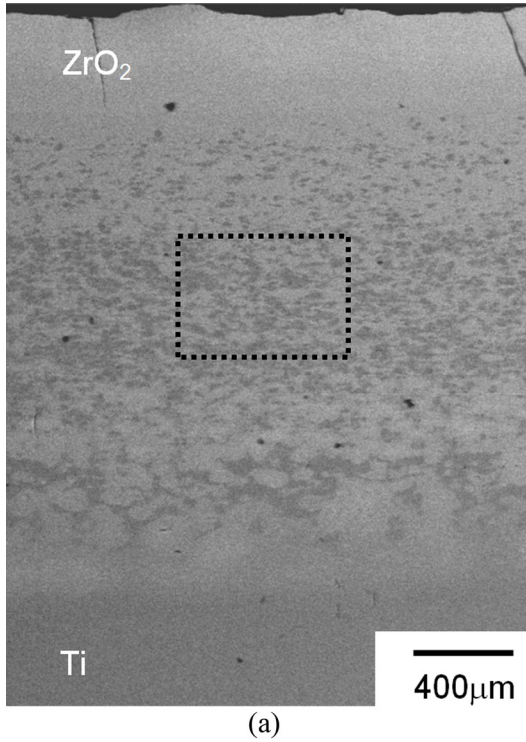
(b)

Figure 4. FGM sample appearance. (a)  $ZrO_2/Ti$  FGM sample and (b) illustration of the FGM sample.

in the thickness direction according to prescribed compositional gradation patterns. The discontinuity between layers with step-wised 6-layer compositional gradations disappears because of occurrence of inter-diffusion of Ti, Zr and O during the fabrication processes. There is no large cluster and few void in the samples. From Figure 5(b), it is seen that the composition of each phase is as predetermined and even in Ti phases oxygen is also present (at analysis point 2), which enables to expect that Ti may react with oxygen to make some titanium oxide in Ti phase.

Figure 6 shows the X-ray diffraction pattern of  $ZrO_2$  surface layer in  $ZrO_2/Ti$  FGMs with  $n = 1$ . It is seen that only the peaks for  $ZrO_2$  with the tetragonal crystal structure and ZrO can be detected, which means that there is no crystal structure change from tetragonal to monoclinic of  $ZrO_2$  in  $ZrO_2$  surface layer during the fabrication (cooling) process.

Next we look at thermo-mechanical behaviour of the FGMs under cyclic thermal shock loading conditions. Figure 7 shows micro-Vickers hardness of  $ZrO_2$  surfaces as a function of number of thermal shock cycles. In case of the number of thermal shock cycles of 0 (just after fabrication), the hardness of  $ZrO_2$  surfaces of the FGMs with  $n = 2$  is low compared to FGMs with  $n = 0.5$  and  $n = 1$ , which means that the FGMs with  $n = 2$  may have more tensile stresses in the  $ZrO_2$  surface layer. According to XRD investigation on  $ZrO_2$  surfaces in the  $ZrO_2/Ti$  FGMs, it was found that only  $ZrO_2$  with a tetragonal crystal structure can be detected in the FGMs with  $n = 0.5$  and 1, meanwhile some of  $ZrO_2$  change their crystal structures from tetragonal to monoclinic in the

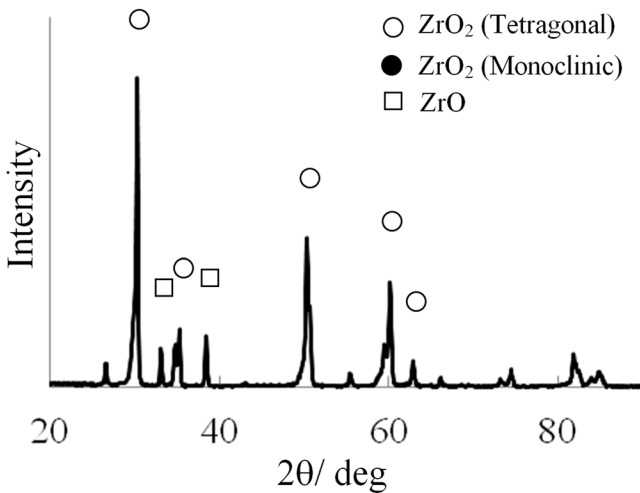


Point number	1	2	3	4
Zr	1.9	0	42.8	42.8
O	9.8	8.5	58.6	56.0
Ti	88.3	91.5	0.8	1.2

**Figure 5.** SEM images of ZrO<sub>2</sub>/Ti FGMs with  $n = 1$ . (a) low magnification image including the area of the high magnification image (surrounded by a dot line) and (b) high magnification image with EDS point analysis data.

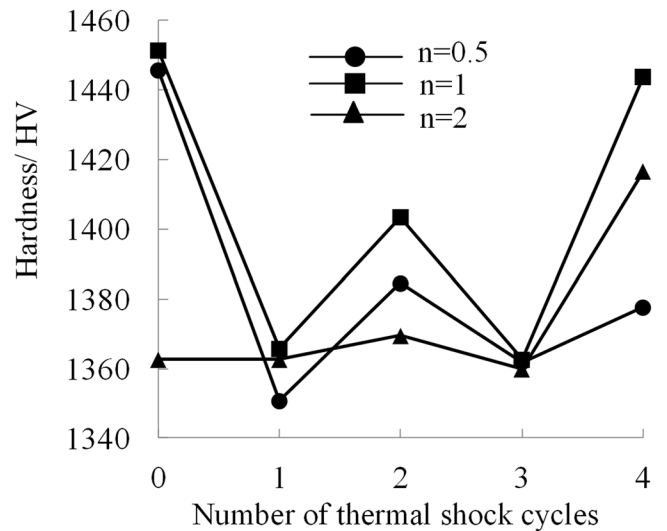
FGMs with  $n = 2$  during fabrication processes, which enable to expect that the residual tensile stresses in the FGMs with  $n = 2$  were enough for causing the stress-induced transformation of ZrO<sub>2</sub> in the ZrO<sub>2</sub> surface layer. In case of the number of thermal shock cycles of 4, hardness of ZrO<sub>2</sub> surfaces in FGMs with  $n = 0.5$  is low compared to FGMs with  $n=1$  and  $n = 2$ .

Figure 8 shows the OM image of ZrO<sub>2</sub> surface, in which



**Figure 6.** X-ray diffraction pattern of ZrO<sub>2</sub> surface layer in ZrO<sub>2</sub>/Ti FGMs with a compositional gradation pattern of  $n = 1$ .

cracks are generated [in Figure 8(a)] and relation between the total length of cracks and number of thermal shock cycles [in Figure 8(b)]. It is seen in Figure 8(a) that a number of cracks are generated near edge of the samples. From Figure 8(b), the total length of cracks increases with increasing number of thermal shock cycles. The FGMs with higher ZrO<sub>2</sub> content, which corresponds to higher value of  $n$ , show higher total length of cracks generated on ZrO<sub>2</sub> surfaces and are



**Figure 7.** Micro-Vickers hardness measured on ZrO<sub>2</sub> surfaces in the FGMs as a function of number of thermal shock cycles.

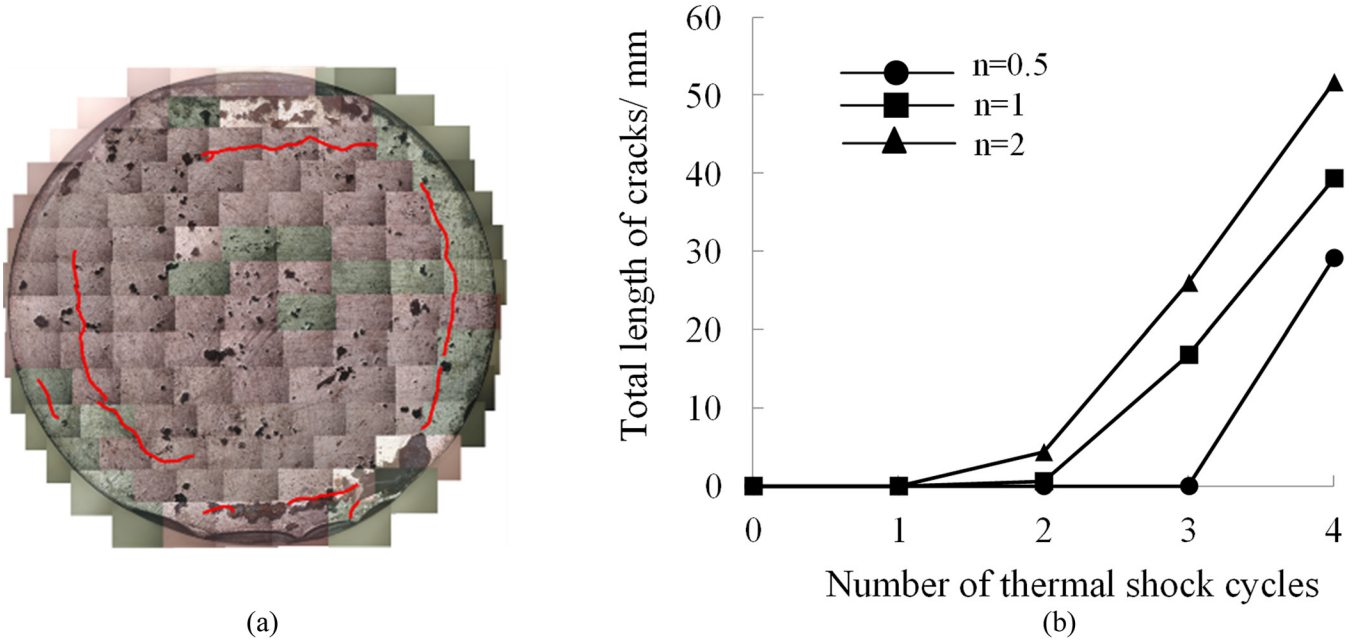


**Figure 8.** Cyclic thermal shock fracture behavior of FGMs. (a) OM image of  $ZrO_2$  surface after the 4th thermal shock loading, in which cracks are generated, and (b) relation between total length of cracks on  $ZrO_2$  surface and number of thermal shock cycles.

easier to fracture in the FGMs under cyclic thermal shock loading conditions. Among the tested samples, FGMs with  $n = 0.5$  show the best resistance to cyclic thermal shock loadings. For the hardness of  $ZrO_2$  surfaces after the 4th cyclic thermal shock loading, FGMs with  $n = 0.5$  show lower hardness than FGMs with  $n = 1$  and  $n = 2$  as shown in Figure 7, which may be attributed to thermal stress relief after cracking on  $ZrO_2$  surfaces in the FGMs subject to cyclic thermal shock loadings. In the next section, a mean-field micromechanics-based model [5] is described to examine such cyclic thermal shock behaviour of the FGMs.

#### 4. MEAN-FIELD MICROMECHANICS-BASED ANALYSIS

Now let us examine the experimental results on cyclic

thermal shock resistance of the FGMs based on a mean-field micromechanics-based model formulated by Tsukamoto [5]. Macroscopically homogeneous composites with spherical particles are considered to be building blocks of the functionally graded thermal barrier coating (FG TBC) plate. The building blocks are assumed to be subject to balanced bi-axial plane stresses. Here, the metal phase is assumed to be matrix and ceramic phase is particles, which are indicated by subscript 0 and 1, respectively, while the inversion of the relation of matrix and particles can be easily derived in the similar way. The inelastic deformation of constituents of the composites include creep with the strain,  $\varepsilon^c$ , plastic deformation with the strain,  $\varepsilon^p$ , and diffusional mass transport along the metal-ceramic interface with the eigen strain of the particle,  $\varepsilon^d$ . The in-plane and out-of-plane micro-stresses in each phase can be written as follows [5],

$$\sigma_0^{in} = 2(\beta_0 + 1/3\gamma_0)\sigma + 3f_1\beta^*(\alpha_1 - \alpha_0)\theta + 2f_1\gamma^*\{(\varepsilon_1^c - \varepsilon_0^c) + \varepsilon^d - \varepsilon^p\} \quad (2)$$

$$\sigma_0^{out} = 2(\beta_0 - 2/3\gamma_0)\sigma + 3f_1\beta^*(\alpha_1 - \alpha_0)\theta - 4f_1\gamma^*\{(\varepsilon_1^c - \varepsilon_0^c) + \varepsilon^d - \varepsilon^p\} \quad (3)$$

for the metal matrix (indicated by subscript 0), and

$$\sigma_1^{in} = 2(\beta_1 + 1/3\gamma_1)\sigma - 3f_0\beta^*(\alpha_1 - \alpha_0)\theta - 2f_0\gamma^*\{(\varepsilon_1^c - \varepsilon_0^c) + \varepsilon^d - \varepsilon^p\} \quad (4)$$

$$\sigma_1^{out} = 2(\beta_1 - 2/3\gamma_1)\sigma - 3f_0\beta^*(\alpha_1 - \alpha_0)\theta + 4f_0\gamma^*\{(\varepsilon_1^c - \varepsilon_0^c) + \varepsilon^d - \varepsilon^p\} \quad (5)$$

for the ceramic particle (indicated by subscript 1).

Here,  $f_0$  and  $f_1$  are the volume fraction,  $\alpha_0$  and  $\alpha_1$  are the coefficient of thermal expansion, and  $\sigma$  is a macro-stress due to balanced bi-axial loadings.  $\beta_0, \beta_1, \gamma_0, \gamma_1, \beta^*$  and  $\gamma^*$  are micromechanical constants depending on the elastic constants and volume fraction of each phase, which were given in the work by Tsukamoto [5]. In this analysis, plastic and creep deformations are supposed to obey the associated flow rule in which both deformation potentials are taken equal to the von Mises-type yield function. Plastic deformation of metal phase is assumed to be expressed by the Swift's equation:

$$\sigma_0^{eq} = a(c + \varepsilon^{p,eq})^{n_p} \quad (6)$$

where  $a, c$  and  $n_p$  are constants.  $\sigma_0^{eq}$  is the flow stress of metals. When the creep deformation of each phase is assumed to be controlled by grain-boundary diffusion (Coble creep), the constitutive equation is expressed as follows,

$$\dot{\varepsilon}_{coble}^{c,eq} = C \frac{\omega_{gb} D_{gb} \Omega}{k T d^3} \sigma^{eq} \quad (7)$$

$C$  is the geometric constant ( $\sim 16$ ),  $D_{gb}$  the grain boundary diffusivity,  $\omega_{gb}$  the grain boundary width,  $\Omega$  the volume of a diffusing atom and  $k$  the Boltzman's constant. The inelastic strain  $\varepsilon^{d,eq}$  by mass transport along the interface between metal and ceramic phases is expressed as follows [5],

$$\dot{\varepsilon}^{d,eq} = C^{int} \frac{\omega_{int} D_{int} \Omega}{k T d_p^3} \sigma_1^{eq} \quad (8)$$

$C^{int}$  is the material constant derived from micromechanical considerations,  $\omega_{int}$  the interface width for diffusion,  $D_{int}$  the interfacial diffusivity and  $\Omega$  the volume of diffusing atom. Therefore, when considering the composites under plane-stress conditions, the constitutive equations can be described by

$$\dot{\sigma}(z,t) = \{S^e(z) + S^p(z,t)\}^{-1} \{ \dot{\varepsilon}(z,t) - \alpha(z) \dot{\theta}(z,t) - \varepsilon^{p(cd)}(z,t) - \varepsilon^{c-d}(z,t) \} \quad (9)$$

$\dot{\sigma}(z,t)$  is the plane stress rate,  $S^e(z)$  the overall plane-stress elastic compliance,  $S^p(z,t)$  the overall plane-stress plastic compliance,  $\alpha(z)$  the overall in-plane thermal expansion coefficient,  $\varepsilon^{p(cd)}(z,t)$  the overall plastic strain rate due to the difference between creep abilities of each phase and interfacial diffusion, and  $\varepsilon^{c-d}(z,t)$  the overall creep strain rate. The details for mathematical expressions of these functions are given in the work by Tsukamoto [5].  $\dot{\sigma}(z,t)$  given in Equation (9) can be incorporated with the lamination theory.

The material property data of Ti and ZrO<sub>2</sub> used in the calculations are shown in Table 1. The total thickness of the samples is set at 9 mm (including 3 mm thickness for the FGM part and 6 mm thickness for the substrate part) as real

**Table 1. Material Property Data of Ti and ZrO<sub>2</sub> Used in the Calculation.**

	Ti	ZrO <sub>2</sub>
Young's modulus, GPa	116	200
Poisson's ratio	0.32	0.3
CTE, 10 <sup>-6</sup> K <sup>-1</sup>	8.6	10.0
Thermal conductivity, Wm <sup>-1</sup> K <sup>-1</sup>	21.9	3.0
Specific heat, Jkg <sup>-1</sup> K <sup>-1</sup>	520	3000
Density, kgm <sup>-3</sup>	4506	5990
Coble creep parameters		
D <sub>gb0</sub> (pre-exp. Term) × W <sub>gb</sub> , m <sup>3</sup> s <sup>-1</sup>	1.9 × 10 <sup>-7</sup>	0.29 × 10 <sup>-6</sup>
Activation energy, Jmol <sup>-1</sup>	1.53 × 10 <sup>5</sup>	5.7 × 10 <sup>5</sup>
Atomic volume, m <sup>3</sup>	1.15 × 10 <sup>-29</sup>	4.66 × 10 <sup>-29</sup>
Grain size, m	10.0 × 10 <sup>-6</sup>	0.01, 1 and 10.0 × 10 <sup>-6</sup>

Diameter of a particle is 40 × 10<sup>-6</sup>m,  $D_{int} \times W_{int}$  is assumed to be the same value as  $D_{gb} \times W_{gb}$  for Ti. Flow stress parameters in Swift equation for Ti are  $a = 600$  MPa,  $c = 0.3$  and  $n = 1$ .

samples have. The thermo-mechanical boundary conditions are considered as follows. The powders to be sintered is stuffed in dice (fully constraint in both in-plane and out-of-plane deformations) at 1400°C. Under this condition, there is no stress in the samples. Then temperature of samples goes down to room temperature (R.T.) at the cooling rate of 100°C/min under the mechanical boundary conditions of fully constraint deformation. At R.T., all the mechanical constraints are relieved (free mechanical constraint). After that, cyclic thermal shock tests start. The ceramic surface is assumed to be heated to 1200°C for 1 min. After the temperature of the ceramic surface reaches 1200°C, the temperature is hold for 60 sec. Then the ceramic surface is exposed to the air with the heat transfer coefficient of 300 W/(m<sup>2</sup>K) and temperature of R.T. during cooling processes. The air cooling processes take 60 sec, and then the ceramic surface is suddenly cooled down to R.T. During cyclic thermal shock tests Ti substrate sides are exposed to air with the heat transfer coefficient of 500 W/(m<sup>2</sup> K) all the time. This process corresponds to one cycle, which is repeated 4 times in the simulation like the current experiments.

Figure 9 shows calculation results of temperature transient of the ZrO<sub>2</sub> surface and maximum stress transient in the ZrO<sub>2</sub> surface layer during fabrication and cyclic thermal shock test processes. It is seen in Figure 9(b) that maximum stresses in the ZrO<sub>2</sub> surface layer vary with temperature transients. The highest stresses can be reached just after the fabrication [at point A in Figures 9(a) and (b)]. During cyclic thermal shock tests, the maximum stresses in the ZrO<sub>2</sub> surface layer change with temperature transients, in which high maximum stress peaks are reached at R.T. Now let us define three parameters such as the mean stress,  $\sigma_{mean}$ , range,  $\Delta\sigma$ , and ratio,  $R$ , of the maximum thermal stresses. To begin with, it is set  $\sigma_{max}$  the high peak value of maximum thermal

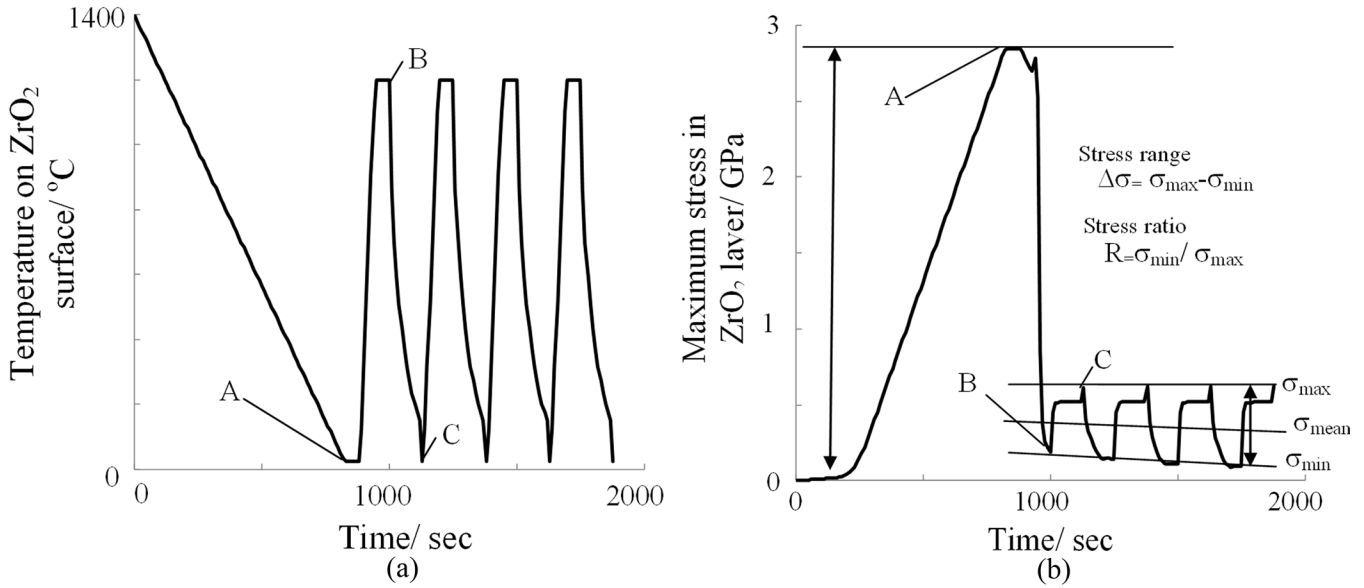


**Figure 9.** Temperature transient of  $ZrO_2$  surface (a) and maximum thermal stress transient in  $ZrO_2$  surface layer (b) during fabrication and cyclic thermal shock processes. Points A, B and C shown in the figures indicates the corresponding points, at which the time is the same.

stresses in the  $ZrO_2$  surface layer at R.T. in a cycle, and  $\sigma_{min}$  the low peak value of the maximum thermal stresses in the  $ZrO_2$  surface layer at  $1200^\circ C$  in a cycle. The mean stress,  $\sigma_{mean}$ , is defined by  $(\sigma_{max} + \sigma_{min})/2$ . The range of stress,  $\Delta\sigma$ , is defined by  $\sigma_{max} - \sigma_{min}$ . The ratio of stress,  $R$ , is defined by  $\sigma_{min}/\sigma_{max}$ .

Now we look at the residual stress states in the  $ZrO_2$  surface layer just after fabrication processes, which are shown in Figure 10. This figure also shows the effect of creep ability (grain size) of  $ZrO_2$  on the residual stress states. It is seen that in cases of any grain sizes ( $0.01$ ,  $1$  and  $10 \mu m$ ) of  $ZrO_2$ , there is little influence of compositional gradation patterns on the residual stress states, meanwhile the grain size (corresponding to creep ability) of  $ZrO_2$  affects the residual stress states.

Figure 11 shows  $\sigma_{mean}$ ,  $\Delta\sigma$  and  $R$  as a function of the number of thermal shock cycles. It is seen in Figure 11(a) that FGMs with a compositional gradation pattern of  $n = 0.5$  (Ti-rich) show the highest mean stresses in the  $ZrO_2$  surface layer among FGMs with three different compositional gradation patterns. This result leads to a premonition that FGMs with  $n = 0.5$  are most likely to be degraded by the cyclic thermal shock loadings. However, from the experimental results shown in Figure 8, FGMs with  $n = 0.5$  show the highest resistance to cyclic thermal shock loadings. Therefore, mean stresses are considered not to be a factor controlling cyclic thermal shock fracture behaviour of the FGMs. Meanwhile, it is seen in Figure 11(b) that higher  $n$  is, higher  $\Delta\sigma$  is, which is reasonable to explain experimental results on cyclic thermal shock fracture behaviour of the FGMs shown in Figure 8. Further, in any compositional gradation patterns,  $\Delta\sigma$  increases with increasing number of thermal shock cycles. For the ratio of maximum stress,  $R$ , it is seen in Figure 11(c)

that the higher  $n$  is, the lower  $R$  is, which is also reasonable to explain experimental results. With increasing number of thermal shock cycles,  $R$  decreases in cases of  $n = 1$  and  $2$ , while  $R$  is almost constant in case of  $n = 0.5$ . Consequently using the parameters of  $\Delta\sigma$  and  $R$ , we can design FGMs with superior resistance to cyclic thermal shock loadings.

Next let us examine the effect of creep ability of  $ZrO_2$  on the range,  $\Delta\sigma$ , and the ratio,  $R$ , of maximum thermal stresses in  $ZrO_2$  surface layers. Figure 12 shows the range,  $\Delta\sigma$ , and ratio,  $R$ , of maximum thermal stresses in  $ZrO_2$  surface layers after the 4th cyclic thermal shock loading as a function of the grain size of  $ZrO_2$ . The grain size of  $ZrO_2$  can be related to the creep ability of  $ZrO_2$  by Equation (7). It is seen in Figure

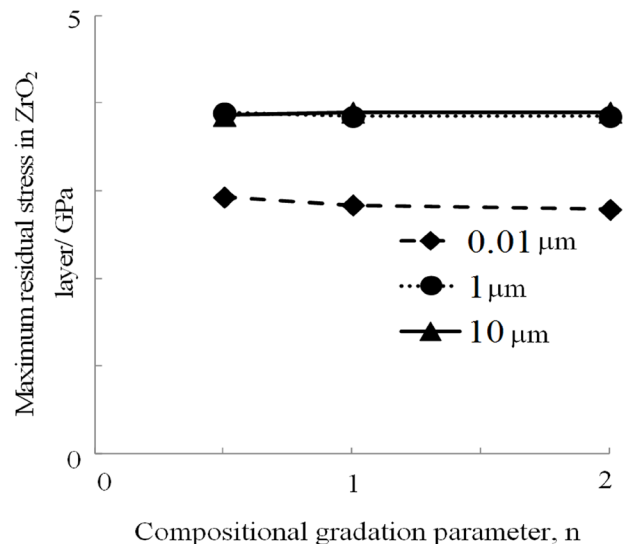


**Figure 10.** Residual stress states in the  $ZrO_2$  surface layer just after fabrication processes.

12(a) that higher  $n$  is, higher  $\Delta\sigma$  is. In case of the grain size of  $0.01\ \mu\text{m}$ ,  $\Delta\sigma$  is largely affected by compositional gradation patterns. It is seen in Figure 12(b) that higher  $n$  is, lower  $R$  is. In case of the grain size of  $0.01\ \mu\text{m}$ ,  $R$  is also largely dependent on compositional gradation patterns compared to the cases of grain sizes of  $1$  and  $10\ \mu\text{m}$ . For FGMs with any compositional gradation patterns,  $R$  increases with increasing grain size of  $\text{ZrO}_2$ .

## 5. DISCUSSION

FGMs are soundly fabricated using SPS. The fabricated FGM samples show reasonable microstructures as predeter-

mined compositional gradation patterns. The presence of titanium oxide in Ti phase was verified by SEM EDS analysis as shown in Figure 5. Cyclic thermal shock behaviour of FGMs was investigated with the fabricated FGM samples with different compositional gradation patterns. Lower  $n$  (corresponding to higher composition of Ti) is, higher resistance to cyclic thermal shock loadings as seen in Figure 8. This experimental result was examined based on the mean-field micromechanics model considering the creep of constituent phases (ceramics and metals) and plasticity of metals and diffusive mass flow at the ceramic and metal phases [5]. Creep of  $\text{ZrO}_2$  largely affects stress states in the FGMs. The FGMs with  $n = 0.5$  taking the highest mean maximum

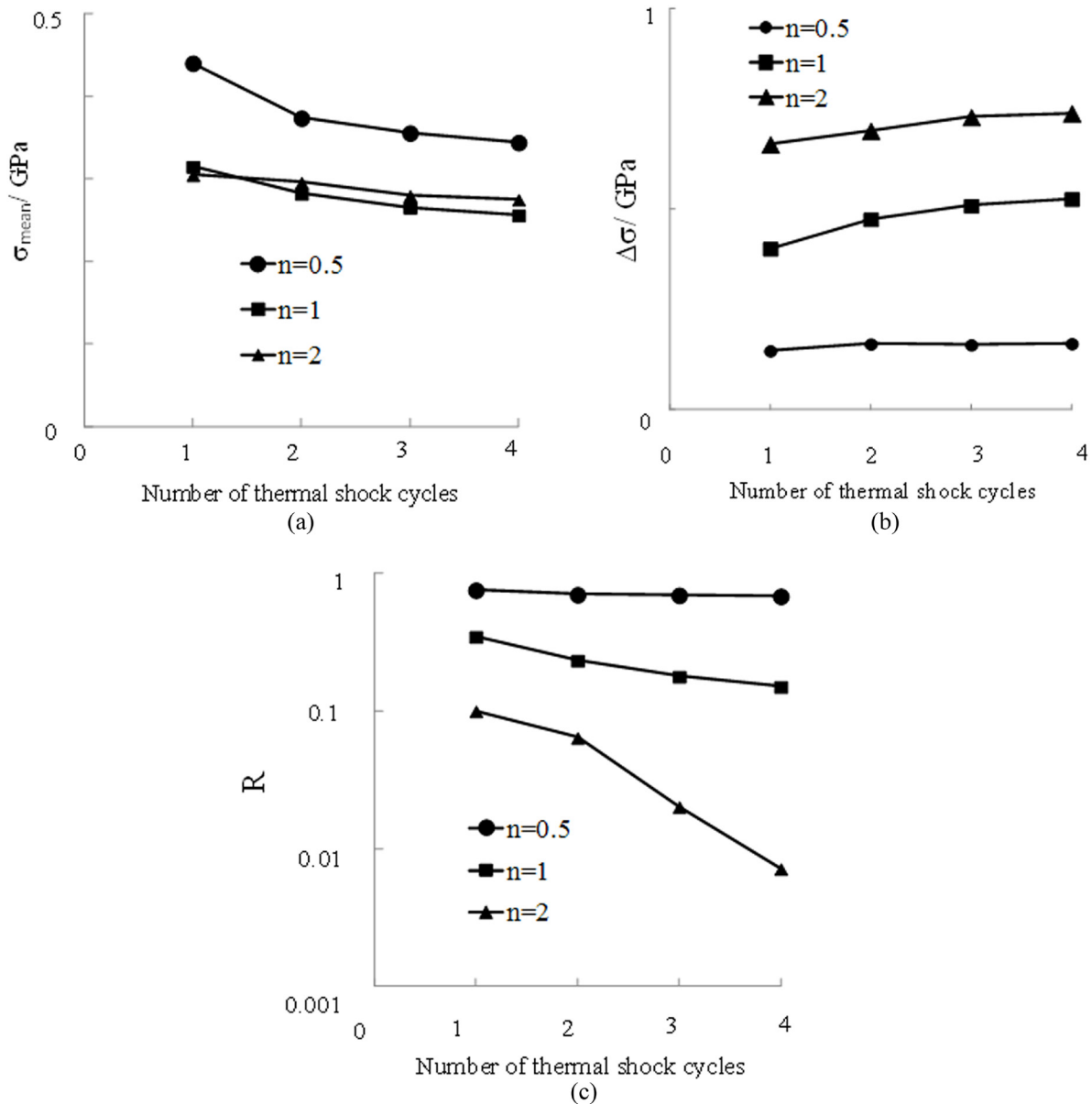


**Figure 11.** Mean stress,  $\sigma_{\text{mean}}$ , range,  $\Delta\sigma$ , and ratio,  $R$ , of thermal stresses in  $\text{ZrO}_2$  surface layer during cyclic thermal shock loading tests. (a)  $\sigma_{\text{mean}}$ , (b)  $\Delta\sigma$ , (c)  $R$ .

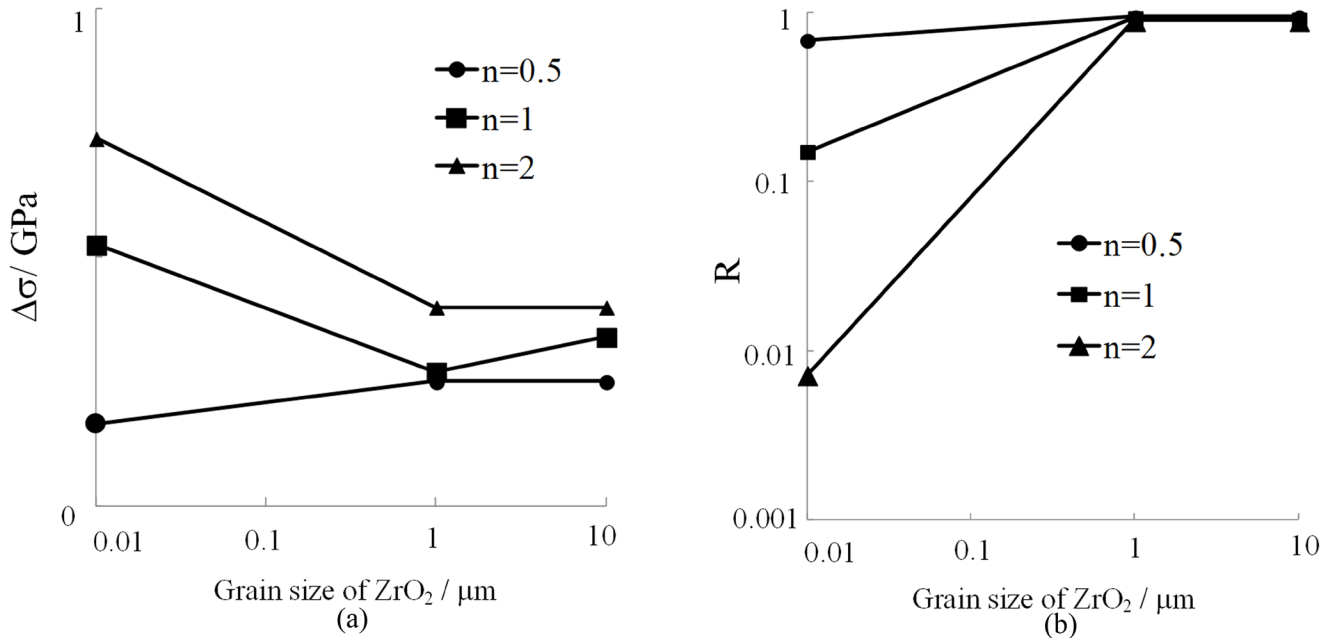


**Figure 12.** Range ( $\Delta\sigma$ ) and ratio ( $R$ ) of maximum thermal stresses in ZrO<sub>2</sub> surface layer after the 4th thermal shock loadings plotted against the grain size of ZrO<sub>2</sub>. (a)  $\Delta\sigma$ , (b)  $R$ .

stresses do not provide the lowest resistance to cyclic thermal shock fracture, which can be unexpected if the mean maximum stresses dominate thermal shock fracture behaviour. Meanwhile, the range,  $\Delta\sigma$ , and ratio,  $R$ , of maximum stresses are considered to determine the cyclic thermal shock fracture behaviour of the FGMs. It is considered that higher  $\Delta\sigma$  and lower  $R$  contribute to promotion of thermal shock fracture of the FGMs. In any number of thermal shock cycles, the order in levels of resistance to cyclic thermal shock loadings in the FGMs with different compositional gradation patterns is fixed.

Creep of ZrO<sub>2</sub> is considered to largely affect the thermal shock fracture behaviour of the FGMs. As seen in Figure 12, the range and ratio of the maximum stresses are highly dependent on compositional gradation patterns in the FGMs with the grain size of 0.01 μm corresponding to high creep ability of ZrO<sub>2</sub>. In this study, ZrO<sub>2</sub> powders used in the experiments have a diameter of 26 nm (0.026 μm). Therefore, the grain size of 0.01 μm is closest and the most reasonable to be used in the simulation to examine the experimental results. It is considered that the cyclic thermal shock resistance of the FGMs fabricated in the study can be largely affected by compositional gradation patterns. Consequently it is important to determine suitable compositional gradation patterns considering the creep ability of ZrO<sub>2</sub> to engineer such FGMs subject to cyclic thermal shock loadings.

## 6. CONCLUSIONS

This study investigated thermo-mechanical behaviour of ZrO<sub>2</sub>/Ti functionally graded materials (FGMs) fabricated by

spark plasma sintering (SPS). A resistance to cyclic thermal shock loadings in FGMs with different compositional gradation patterns (Ti-rich, linear and ZrO<sub>2</sub>-rich gradation patterns) was examined. Under cyclic thermal shock loading conditions, Ti-rich FGMs show superior properties among the tested FGM samples. Mean-field micromechanics-based examinations reveal that the range and ratio of maximum thermal stresses in ZrO<sub>2</sub> surface layers in FGMs are dominant factors controlling cyclic thermal shock fracture but not mean thermal stresses. The FGMs with Ti-rich gradation patterns show high range and low ratio of maximum stresses in ZrO<sub>2</sub> surface layers, which can lead to FGMs having high resistance to cyclic thermal shock loadings. Creep of ZrO<sub>2</sub> have a large influence on the range and ratio of thermal stresses in ZrO<sub>2</sub> surface layers, that is, the range and ratio of thermal stresses in ZrO<sub>2</sub> surface layers largely depends on compositional gradation patterns in case of high creep rates of ZrO<sub>2</sub> in the FGMs.

## ACKNOWLEDGEMENTS

The authors acknowledge the financial supports from Ministry Education, Culture, Sports, Science and Technology, Regional Innovation Cluster program (Gifu Technical Innovation Program, Japan).

## REFERENCES

- [1] P.M. Kelly, L.R.F. Rose, "The martensitic transformation in ceramics—its role in transformation toughening," *Prog. Mater. Sci.* 47, 463–557 (2002). [http://dx.doi.org/10.1016/S0079-6425\(00\)00005-0](http://dx.doi.org/10.1016/S0079-6425(00)00005-0)

- [2] B.C. Weber, H.J. Garrett, F.A. Mauer, M.A. Schwartz, "Observations on the stabilization of zirconia," *J. Am. Ceram. Soc.* 39, 197–207 (1956). <http://dx.doi.org/10.1111/j.1151-2916.1956.tb15645.x>
- [3] A. Arias, "Thermal shock resistance of zirconia with 15 mol %Titanium," *J. Am. Ceram. Soc.* 49, 334–338 (1966). <http://dx.doi.org/10.1111/j.1151-2916.1966.tb13276.x>
- [4] M. Koizumi, "FGM activities in Japan," *Composites Part B*, 28B, 1–4 (1997). [http://dx.doi.org/10.1016/S1359-8368\(96\)00016-9](http://dx.doi.org/10.1016/S1359-8368(96)00016-9)
- [5] H Tsukamoto, "Analytical method of inelastic thermal stresses in a functionally graded material plate by a combination of micro- and macromechanical approaches," *Composites: Part B*, 34, 561–568 (2003). [http://dx.doi.org/10.1016/S1359-8368\(02\)00037-9](http://dx.doi.org/10.1016/S1359-8368(02)00037-9)
- [6] L.D. Teng, F.M. Wang, W.C. Li, "Thermodynamics and microstructure of Ti-ZrO<sub>2</sub> metal-ceramic functionally graded materials," *Mater. Sci. Eng. A* 293, 130–136 (2000). [http://dx.doi.org/10.1016/S0921-5093\(00\)01045-5](http://dx.doi.org/10.1016/S0921-5093(00)01045-5)
- [7] L.D. Teng, W.C. Li, F.M. Wang, "Effect of Ti content on the martensitic transformation in zirconia for Ti-ZrO<sub>2</sub> composites," *J. Alloys Compds.* 319, 228–232 (2001). [http://dx.doi.org/10.1016/S0925-8388\(00\)01272-X](http://dx.doi.org/10.1016/S0925-8388(00)01272-X)
- [8] K.L. Lin, C.C. Lin, "Reaction between titanium and zirconia powders during sintering at 1500°C," *J. Am. Ceram. Soc.* 90, 2220–2225 (2007). <http://dx.doi.org/10.1111/j.1551-2916.2007.01708.x>
- [9] T.A. Schaedler, O. Fabrichnaya, C.G. Levi, "Phase equilibria in the TiO<sub>2</sub>-YO<sub>1.5</sub>-ZrO<sub>2</sub>," *J. Euro. Ceram. Soc.* 28, 2509–2520 (2008). <http://dx.doi.org/10.1016/j.jeurceramsoc.2008.03.011>
- [10] A. Kawasaki, R. Watanabe, "Evaluation of thermomechanical performance for thermal barrier type of sintered functionally graded materials," *Composites Part B* 28, 29–35 (1997). [http://dx.doi.org/10.1016/S1359-8368\(96\)00017-0](http://dx.doi.org/10.1016/S1359-8368(96)00017-0)
- [11] Z.H. Jin, "Effect of thermal property gradients on the edge cracking in a functionally graded coating," *Surface and Coatings Technology*, 179, 2–3, 23, 210–214 (2004). [http://dx.doi.org/10.1016/S0257-8972\(03\)00803-X](http://dx.doi.org/10.1016/S0257-8972(03)00803-X)
- [12] Z.-H., Jin, W.J. Luo, "Thermal shock residual strength of functionally graded ceramics," *Materials Science and Engineering: A*, 435–436, 71–77 (2006). <http://dx.doi.org/10.1016/j.msea.2006.07.011>
- [13] B.L. Wang, Y-W. Mai, X-H. Zhang, "Thermal shock resistance of functionally graded materials," *Acta Materialia*, 52, 4961–4972 (2004). <http://dx.doi.org/10.1016/j.actamat.2004.06.008>
- [14] K. Kokini, J. DeJonge, S. Rangaraj, B. Beardsley, "Thermal shock of functionally graded thermal barrier coatings with similar thermal resistance," *Surface and Coatings Technology*, 154, 223–231 (2002). [http://dx.doi.org/10.1016/S0257-8972\(02\)00031-2](http://dx.doi.org/10.1016/S0257-8972(02)00031-2)
- [15] Z. Han, B. Xu, H. Wang, S. Zhou, "A comparison of thermal shock behavior between currently plasma spray and supersonic plasma spray CeO<sub>2</sub>-Y<sub>2</sub>O<sub>3</sub>-ZrO<sub>2</sub> graded thermal barrier coatings," *Surface and Coatings Technology*, 201, 9–11, 5253–5256 (2007). <http://dx.doi.org/10.1016/j.surfcoat.2006.07.176>
- [16] H. Hamatani, N. Shimoda, S. Kitaguchi, "Effect of the composition profile and density of LPPS sprayed functionally graded coating on the thermal shock resistance," *Science and Technology of Advanced Materials*, 4, 197–203 (2003). [http://dx.doi.org/10.1016/S1468-6996\(03\)00023-8](http://dx.doi.org/10.1016/S1468-6996(03)00023-8)
- [17] H. Tsukamoto, "Design against fracture of functionally graded thermal barrier coatings using transformation toughening," *Mater. Sci. Eng. A* 527, 3217–3226 (2010). <http://dx.doi.org/10.1016/j.msea.2010.01.087>
- [18] H. Tsukamoto, H. Sato, Y. Watanabe, "Design of ZrO<sub>2</sub>/Ti functionally graded thermal barrier coatings based on a nonlinear micromechanical approach," *Applied Mechanics and Materials*, 152–154, 167–170 (2012). <http://dx.doi.org/10.4028/www.scientific.net/AMM.152-154.167>



## Performance Evaluation of Out-of-Autoclave Sandwich Structures with K-COR and Nomex Core

S. ANANDAN<sup>1</sup>, S. NAGARAJAN<sup>1</sup>, V. BHEEMREDDY<sup>1</sup>, K. CHANDRASHEKHARA<sup>1,\*</sup>, D. PFITZINGER<sup>2</sup> and N. PHAN<sup>3</sup>

<sup>1</sup>Department of Mechanical and Aerospace Engineering, Missouri University of Science and Technology, Rolla, MO 65409

<sup>2</sup>GKN Aerospace, St. Louis, MO 63042

<sup>3</sup>NAVAIR Systems Command, Patuxent River, MD 20670

### KEYWORDS

sandwich composites  
Nomex core  
out-of-autoclave  
K-COR  
flatwise tensile strength  
cohesive damage modeling

### ABSTRACT

Composite sandwich structures are being increasingly employed in the aerospace, marine as well as other applications which require high strength, high in-plane and flexural stiffness coupled with a reduction in weight. In the aerospace industry sandwich composites are usually manufactured using the autoclave process which is expensive and time consuming. A viable alternative is the Out-of-Autoclave (OOA) process whose main advantage is the low cost of manufacturing. One of the most dominant failure modes in sandwich composites is the debonding that occurs at the facesheet-to-core interphase. A well-formed adhesive bond at the skin to core interphase and improved adhesion strength are significant factors in preventing bond failure. In this paper honeycomb and K-COR sandwich composites are manufactured using the Out-of-autoclave process. The adhesive bonding strength in each of the manufactured panels is quantified by evaluating the flatwise tensile strength in accordance with ASTM standards. Core-facesheet debonding was observed in K-COR sandwich while core failure was observed in the Nomex sandwich structures. Finite element modeling and simulation of Nomex and K-COR sandwich structures subjected to flatwise tension is conducted using comprehensive three-dimensional finite element models. Cohesive damage modeling approach is used to simulate delamination failure in both Nomex and K-COR sandwich structures. Finite element results are compared with the experimental results for model validation. The ultimate flatwise tensile strength predicted by simulation was found to be in good agreement with the experimental results.

© 2014 DEStech Publications, Inc. All rights reserved.

### 1. INTRODUCTION

Sandwich composites are made of relatively stiff and strong facesheets, which absorb most of the in-plane loading and bending, separated by a thicker flexible core, which absorbs the shear load. These result in improved mechanical performance and reduction in weight compared to conventional composites. Hence, sandwich composites are employed in aerospace and marine industries as well as in other applications that require high strength, high in-plane and flexural stiffness coupled with a reduction in weight [1]. They are especially valued in the aircraft industry where

manufacturers find it expensive to produce complex components from laminates. These laminates were also found to be susceptible to impact damage from dropped tools [2]. Design and application of sandwich composites depends on thorough characterization and understanding of the sandwich constituent materials and also the structure as a whole under quasi-static and dynamic loading [1,3].

Currently, most widely used cores in sandwich structures are honeycomb and foam cores. The honeycomb core is composed of an array of hollow hexagonal or columnar cells separated by thin vertical walls. Since the honeycomb core is composed of up to 98% air, there is a reduction in the amount of material used, which brings down the overall weight and cost. A hexagonal shaped core provides for high in-plane

\*Corresponding author. Email: [chandra@mst.edu](mailto:chandra@mst.edu)

bending stiffness coupled with low density and hence is highly valued in the aerospace industry. Honeycomb cores can be made from thin sheets of metal such as aluminum or from organic materials, such as aramid papers. Honeycomb made from aramid papers exhibit greater design flexibility through low coefficient of thermal expansion, low electrical conductivity and dielectric properties [4]. Honeycomb cores, however, have some disadvantages such as lower surface area of core for bonding, sensitivity to hot and humid environments and susceptibility to moisture absorption.

The foam core is usually composed of “closed cell” type polymeric foam. The main advantages of this foam are the increased surface area of bonding and the resistance to ingress by water [5]. The disadvantage of this core is its stiffness and strength which are lower when compared to that of the honeycomb core. This problem can be overcome by reinforcing the foam with Z-pins. These Z-pins are usually steel, aluminum, glass/epoxy or carbon rods which are embedded in the foam core at specific angles so as to form a truss. Reinforcing the foam core with Z-pins have shown to improve the transverse stiffness and strength properties compared to that of conventional foam cores [2]. High stiffness pin-reinforced sandwich structures find application in the aerospace, naval and automotive applications.

In the aerospace industry sandwich composites are usually manufactured using autoclave processing which produces high quality parts. However this high quality comes at a price due to the high capital investment and operating cost, long cycle time, and low energy efficiency [6]. The other drawback with this process is its inability to manufacture large structural components, an example being NASA's Constellation program Ares V cargo launch vehicle which requires large composite parts of sizes up to 10m in diameter [7]. These would require sufficiently large autoclaves which would in turn increase the infrastructure investment and operating cost.

Several studies have been devoted to developing non autoclave processes that have a lower cost of manufacturing and produce parts whose quality and performance are comparable to autoclaved parts. Among these the “Out-of-Autoclave (OOA) vacuum bag only process” has emerged as a viable option. The OOA technique enables composites to be manufactured using vacuum pressure only which reduces the initial investment, cost of operation and tooling [8]. In addition they offer greater design flexibility to manufacture large structural composites with complex geometries. Prepregs used in the OOA process are specially designed to remove entrapped air or other volatiles from the lay-up when vacuum is applied at the initial stages of the cure cycle. This is achieved due to the partial impregnation of the prepreg which creates a porous medium. These pores help in the evacuation of any entrapped volatiles before they are filled by the resin during cure [9]. The use of these prepregs eliminates the need for high positive pressure as in the case of the

autoclaves. The drawback of the OOA technique however lies in the elimination of porosity and compaction of the lay-up to produce a high resultant fiber volume fraction.

Sandwich composites have several possible failure modes such as tensile/compressive failure, core to facesheet debonding, core failure, indentation failure, wrinkling and global buckling [10]. Among these the most dominant failure mode is local instability of the facesheet resulting in either debonding or buckling from the core. Debonding in sandwich structures is a serious problem leading to severe degradation of its structural properties. They may occur during the fabrication phase of sandwich composites due to the presence of foreign matter at the core to facesheet interphase. They may also be caused by external loading such as impact [11]. When a sandwich structure is subjected to bending, difference in modulus between the core and facesheet results in shear stress at the interphase. This results in peeling of the facesheet from the core [4]. Failure of the structure due to debonding at the core/facesheet interphase has been studied by numerous authors. Some of these studies focused on the effect of debonding on the structural properties of the sandwich composite [11–14]. Several studies focused on the debond fracture toughness [10,15–17]. Some work has also been done on the effect of adhesive fillet formation on interfacial debonding. Studies conducted by Grove *et al.* [18] have shown that higher de-bonding energy can be obtained with larger, regular shaped adhesive fillets between the honeycomb cell walls and the skin. Hayes *et al.* [19] have shown that apart from size, quality of the fillet also plays a role. Rion *et al.* [20] have shown that failure occurs in the adhesive meniscus when low weight adhesive is used. Butukuri *et al.* [3] showed that an increase in the adhesive fillet area corresponds to an increase in the flatwise tensile strength. Kratz *et al.* [8] correlated core pressure measurements with adhesive fillet formation in honeycomb sandwich cores. Authors overall observed that the mechanical performance of sandwich structures is dependent upon the quality of the core-to-facesheet adhesive bond. Properties such as debond fracture toughness, residual strengths after delamination and effect of adhesive fillet formation on sandwich performance have been investigated extensively. The adhesive bond strength is one of the important parameters which influences debonding and can be determined in many ways. The current work focuses on quantifying the adhesive bond strength in K-COR and Nomex sandwich composites. One method involves evaluating the flatwise tensile strength of the sandwich composite.

Finite element modeling and simulations are often used to cost-effectively study delamination failure in composite laminates. Borst [21] has reviewed various computational modeling approaches for localization and failure phenomena in solids. Diehl [22] has developed a penalty based cohesive damage model for simulating the epoxy-bonded aluminum arms being peeled off in a double cantilever beam specimen.

Wimmer *et al.* [23] have investigated delamination growth in laminated composites using the cohesive zone modeling approach. Kozak [24] has worked on prediction of crack growth in brittle and ductile structural materials. The authors have obtained various parameters for modeling the cohesive behavior from experiments. Rahul Kumar *et al.* [25] have proposed a cohesive modeling technique for crack propagation in viscoelastic materials using cohesive elements. The model has been applied to study a model problem of peel testing of polymer adhesives. Finite element modeling and simulation of K-COR sandwich structures has been investigated by few researchers [27–29]. Sharkey *et al.* [27] has developed macro-mechanical models for X-COR and K-COR composite sandwich panels. The microstructural details of these specialty cores have been taken into account. Virakthi [28] has developed finite element models to obtain stiffness and strength of pin reinforced sandwich cores under compressive and shear loading conditions. Geometrically non-linear models for the reinforced pins have been considered. The effect of adhesive layer yielding on the stiffness of structure was analyzed. Marasco [29] has developed local-global finite element modeling approach for Z-pinned sandwich cores and also validated the approach for X-COR and K-COR structures. Most of the available literature regarding damage modeling of sandwich structures is limited to two-dimensional finite element models. Moreover, limited work has been done on finite element modeling of K-COR. The cohesive modeling approach used in this work for failure of Nomex and K-COR based sandwich structures is relatively new.

The first part of this paper deals with manufacturing Nomex honeycomb and K-COR foam core sandwich panels using the OOA process. The panels were then evaluated for flatwise tensile (FWT) strength in accordance with ASTM C297. Three-dimensional models are developed for both Nomex and K-COR sandwich structures. The geometry of honeycomb core is explicitly modeled to simulate the failure behavior efficiently. The developed finite element models are used to simulate failure of sandwich structures under flatwise tensile loading. The flatwise tension simulation results are compared with experimental results to validate the finite element model.

## 2. MATERIALS

Nomex honeycomb (1/8-HRH 10-8pcf from Hexcel) is manufactured using NOMEX aramid fiber sheets dipped in phenolic resin. The Nomex sheets are then bonded at the nodes using a thermosetting adhesive to form a hexagonal shape and dipped again in phenolic resin to maintain the shape [20]. The HRH-10 honeycomb characterized by its low density and resilience is used in exterior aircraft parts such as radomes and fairings. Nomex sandwich panels were

manufactured using MTM45-1/IM7 prepreg and MTA241/PK13 adhesive system, manufactured by ACG. MTM45-1 is a unidirectional prepreg having fiber areal weight of 145 g/m<sup>2</sup> and a nominal resin content of 32%. It contains a high performance toughened epoxy matrix and therefore exhibits a high level of damage tolerance. It also has a low temperature cure which lowers the cost of tooling. MTA241/PK13 adhesive has a nominal density of 0.06 psf (29 g/m<sup>2</sup>) and possesses high service temperature capability.

K-COR is a lightweight, pin-reinforced closed cell foam core in which partially cured reinforcing pins extend beyond the foam surface. The extensions are folded back on to the core under the application of heat and pressure [5]. Such cores, on account of their high resistance to failure are used in aerospace applications such as fuselage, wing, and tail skins. K-COR sandwich panels were manufactured using the Cycom 5320/T40/800B prepreg and FM 309-1M adhesive system, manufactured by Cytec. Cycom 5320 is a unidirectional prepreg having a fiber areal weight of 145 g/m<sup>2</sup> and a nominal resin content of 33%. It contains a toughened epoxy resin system. FM 309-1M adhesive has a nominal density of 0.06 psf (29 g/m<sup>2</sup>) and possesses high service temperature capability.

## 3. METHODOLOGY

### 3.1. Manufacturing

The schematic of the baseline bagging procedure employed for the OOA process is shown in Figure 1. A flat aluminum plate is used as the mold. It is covered by a layer of Ethylene Tetrafluoroethylene (ETFE) release film to ensure easy release of the sandwich panel. Each facesheet in the sandwich structure has two plies of prepreg material laid up in [0°/90°] orientation with 0° ply direction aligned with the L-direction (ribbon direction) of the core. Adhesive layers are placed in between the core and facesheets. Glass tows at the corners of the panel, aid in the removal of entrapped air. A non-porous ETFE release film is placed on the panel followed by an aluminum caul plate. The entire layup is sealed using a vacuum bag and debulked according to the manufacturer recommended debulk cycle.

K-COR panels employing Cycom 5320 prepreps were debulked for duration of 4 hours, following which they were cured in an oven at 121°C (250°F) for 2 hours and post-cured at 177°C (350°F) for 2 hours. For Nomex panels manufactured with the MTM 45-1 prepreps, a debulk cycle is performed for every ply for duration of 30 minutes followed by debulking of the entire part under vacuum for 4 hours. It is then heated in an oven to 82.2°C (180°F) and held for 4.5 hours. The temperature is increased to 121.1°C (250°F) and held for 4.5 hours followed by a post-cure at 176.6°C (350°F) for 2 hours.

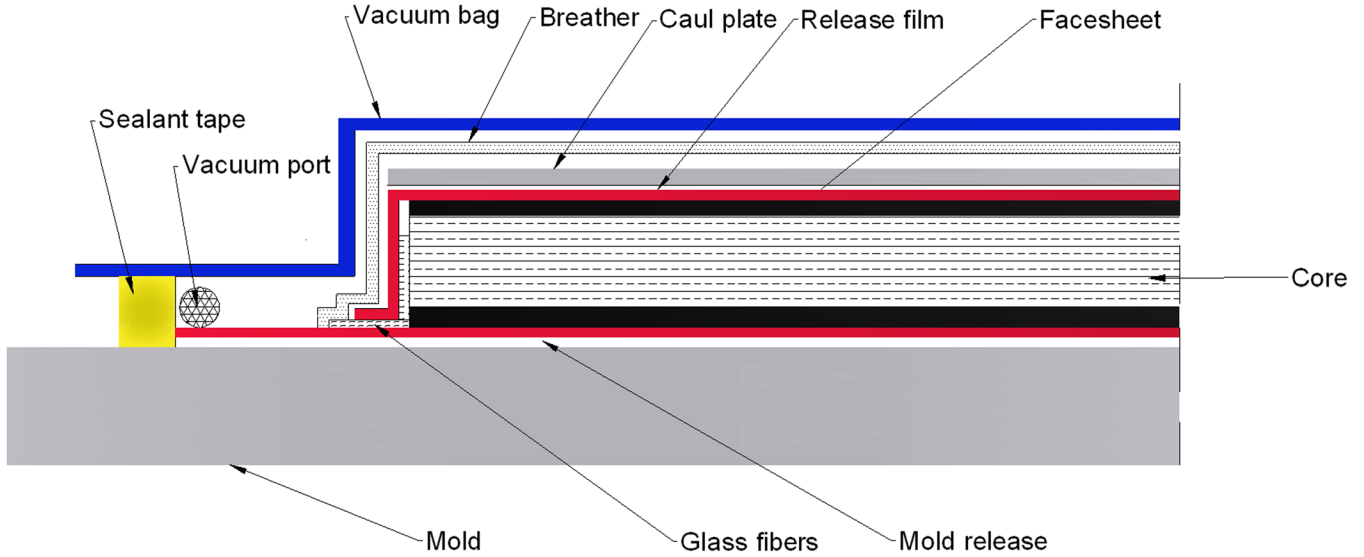


Figure 1. Cross sectional schematic of the OOA Sandwich Composite Manufacturing.

### 3.2. Finite Element Modeling

Finite element models are developed to simulate and analyze the flatwise tensile behavior of both Nomex and K-COR based sandwich structures using cohesive damage modeling technique. Cohesive damage models are alternative to conventional fracture mechanics approaches, simple to implement, and can effectively model crack initiation and propagation. In a cohesive damage modeling approach, the crack initiation and propagation are governed by traction-separation laws across the crack faces and near the crack tip. A schematic of the traction-separation law is shown in Figure 2. The figure depicts a bilinear traction-separation law for Mode-I (normal opening mode) only. The area under the traction-separation curve represents the fracture toughness of the failure interface.

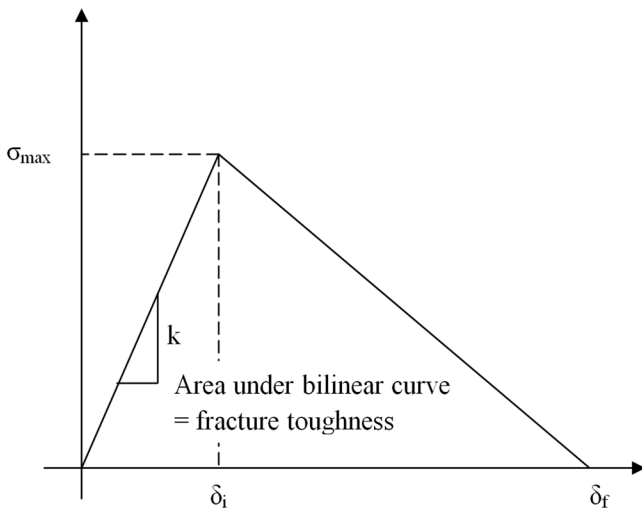


Figure 2. Schematic Representation of Traction-Separation for Normal Crack Opening Mode.

The constitutive relation between traction and separation is given by [30],

$$\{\sigma\} = [k]\{\delta\} \quad (1)$$

where,

- $\{\sigma\}$  = stresses in the cohesive layer
- $[k]$  = stiffness matrix
- $\{\delta\}$  = separation at the cohesive zone

The elastic stiffness matrix parameters can be treated as penalty parameters and can be approximated. When a small stiffness value is used, it adds compliance to the model and affects the solution accuracy. If large stiffness values are used, the solver will have convergence issues. The loading condition is purely normal on the sandwich structure and the shear components of stiffness matrix will have negligible effect on the stresses calculated. As a result, the off-diagonal terms of the stiffness matrix in Equation (1) are assumed to be zero. In order to define an uncoupled traction behavior, reliable data that fully relates normal and shear components of tractions and strains need to be obtained from experiments. The principal diagonal terms are assumed to be equal to each other and initiated to a sufficient large value based on a convergence analysis with various cases considered. To determine suitable parameters for principal diagonal terms an approach proposed by Turon *et al.* [31] was implemented. The elastic stiffness of the interface in normal and tangential directions (principal diagonal terms) can be approximated in terms of elastic modulus and thickness of bonded structures.

$$\begin{Bmatrix} k_n \\ k_t \\ k_t \end{Bmatrix} = \frac{1}{h} \begin{Bmatrix} \alpha E \\ \alpha G \\ \alpha G \end{Bmatrix} \quad (2)$$

**Table 1. Material Properties for Finite Element Simulation.**

Property	Facesheet [34]	Nomex [33]	K-COR Foam [27]	Z-Pin [27]	Adhesive (Cohesive Damage Layer) [32]	Nomex Core (Cohesive Damage Layer) [33]
Young's Modulus	$E_{11} = 151$ GPa $E_{22} = E_{33} = 10.1$ GPa	3.4 GPa	36 MPa	156.5 GPa	1.72 GPa	3.4 GPa
Poisson's Ratio	$\nu_{12} = \nu_{13} = 0.24$ $\nu_{23} = 0.5$	0.3	0.38	0.23	–	–
Shear Modulus	$G_{12} = G_{13} = 5.1$ GPa $G_{23} = 3.14$ GPa	–	–	–	–	–
Interface Strength	–	–	–	–	69.88 MPa	108.5 MPa

where,

- $h$  = characteristic thickness of surrounding structure
- $E$  = young's modulus of bulk material
- $G$  = shear modulus of bulk material
- $\alpha$  = parameter  $\gg 1$

Numerical issues such as spurious oscillations of tractions can occur if the interface stiffness values are assumed to be very high [30,31]. This value needs to be carefully selected as it can affect the overall compliance of structure if it is low, and causes numerical issues if it is very high. As per approach described by Turon *et al.* [31], the value of  $\alpha$  has been selected as 50.

The damage initiation in cohesive zone is controlled by cohesive strength ( $\sigma_{\max}$ ) of the interface, which is the maximum stress that the interface would withstand and above which the damage initiates. The selection of cohesive zone

parameters is important for damage modeling. Conventionally this involves using certain predictive methods of estimating these parameters from fracture toughness of the material undergoing damage. Also, in some cases trial-and-error methods are required if the interface strength is not known [22]. However, in this study, cohesive zone parameters were directly obtained from literature. These parameters are also shown in Table 1. Once the damage is initiated, the damage evolution is described by introducing a stiffness degradation parameter,  $D$ , as shown below [30].

$$\sigma_{\max} = (1 - D)\sigma \quad (3)$$

where,

- $\sigma_{\max}$  = strength of interface
- $D$  = degradation parameter
- $\sigma$  = stress in the interface

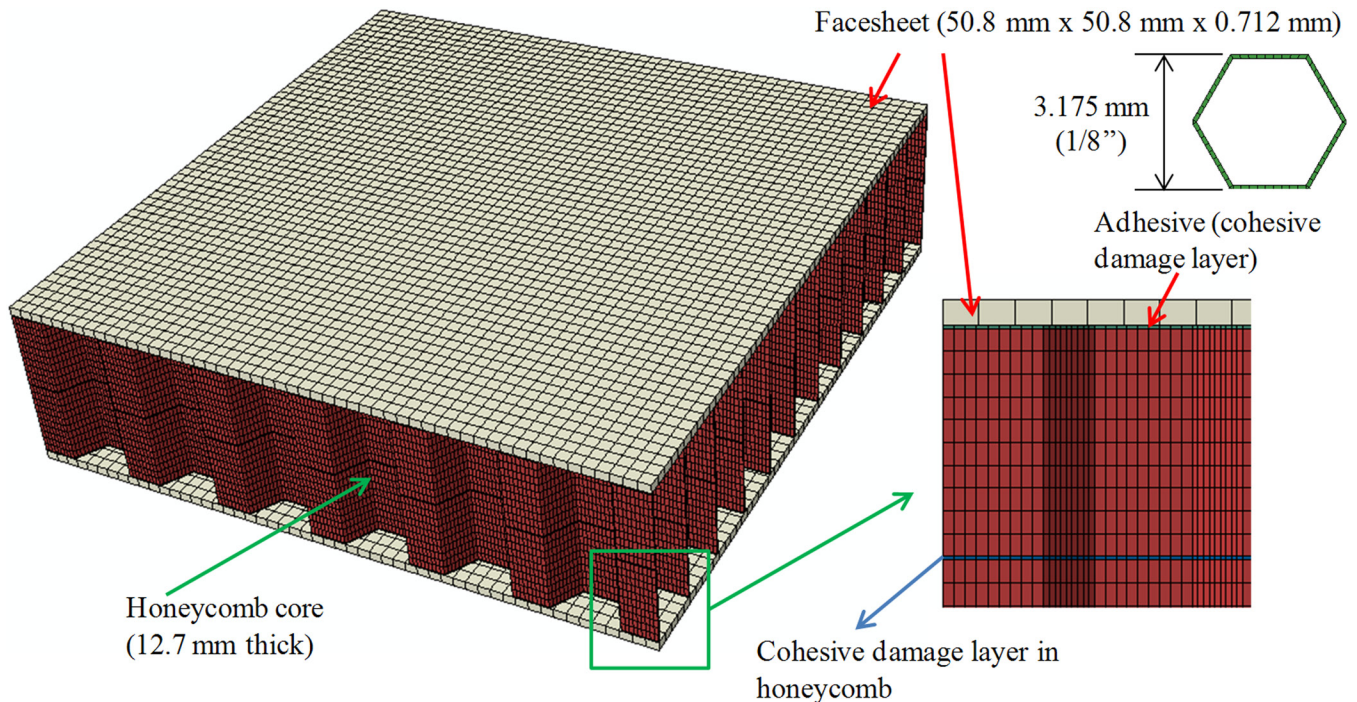


**Figure 3. Finite Element Model of Nomex Honeycomb Core Sandwich Structure.**

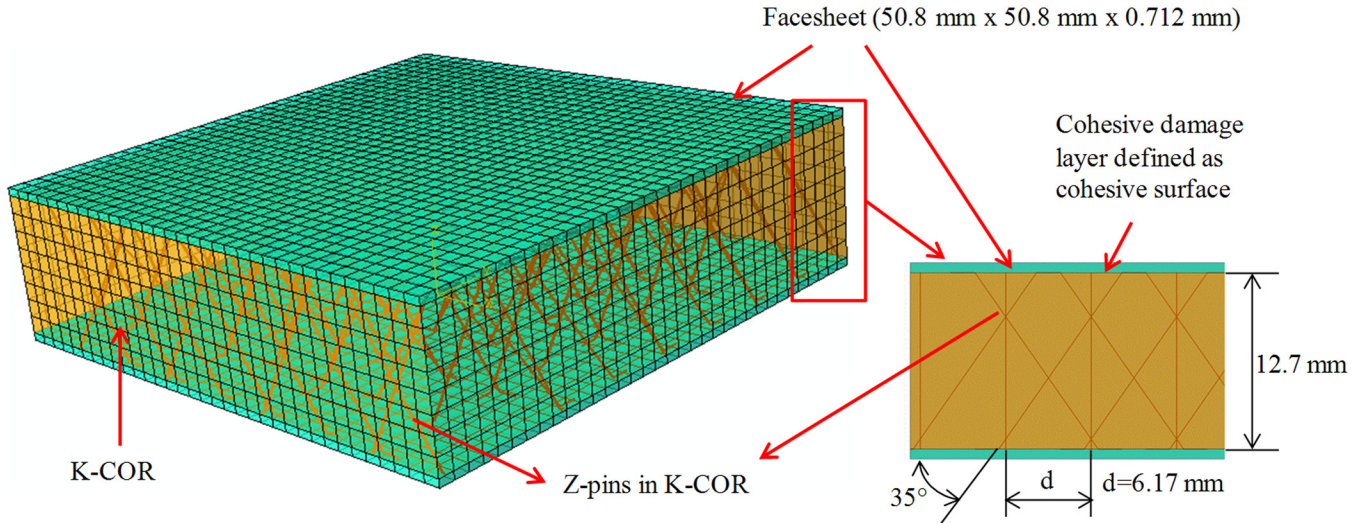


Figure 4. Finite Element Model of K-COR Sandwich Structure.

The damage parameter  $D$ , is equal to zero before damage initiation and increases to 1 after damage is initiated. The damage evolution behavior can be linear, exponential or a user-dependent curve. In this work, a bilinear traction-separation law is used to simulate the failure behavior of Nomex and K-COR sandwich structures under flatwise tension. Comprehensive three-dimensional finite element models are developed for both Nomex and K-COR sandwich structures in ABAQUS v. 6.10 as shown in Figures 3 and 4 respectively.

For the finite element model of Nomex honeycomb core sandwich structure, facesheets and Nomex honeycomb core were meshed using 8-node linear brick elements (C3D8). The adhesive at facesheet/core interface was modeled using 8-node three-dimensional cohesive elements (COH3D8) and a layer of cohesive elements with same formulation was also embedded in Nomex honeycomb core. This allows equal probability of failure in adhesive and honeycomb core based on the stress levels in the material during flatwise tension.

In the finite element model of K-COR sandwich structure, facesheets and K-COR were meshed using 8-node quadrilateral in-plane general purpose continuum shell

(SC8R) elements. A reduced integration scheme with hour-glass control has been implemented in the element formulation. Use of continuum shell elements, unlike conventional three-dimensional solid elements, reduces the computational time drastically. Z-pins were embedded into the core using an 'EMBEDDED ELEMENT' constraint as shown in Figure 4. The Z-pins were modeled using quadratic beam elements (B32). These pins were spaced and angled as per the physical geometry of K-COR. Shear deformation was assumed to be negligible and no friction between the Z-pins and core was considered. Unlike the cohesive elements used in modeling the adhesive failure in Nomex core sandwich structure, a cohesive surface based failure was considered for modeling adhesive in K-COR sandwich structure.

## 4. RESULTS AND DISCUSSION

### 4.1. Flatwise Tensile Testing

Flatwise tensile test serves as a quality control test for bonded sandwich panels [26], as they provide information on the strength and quality of the core to facesheet inter-

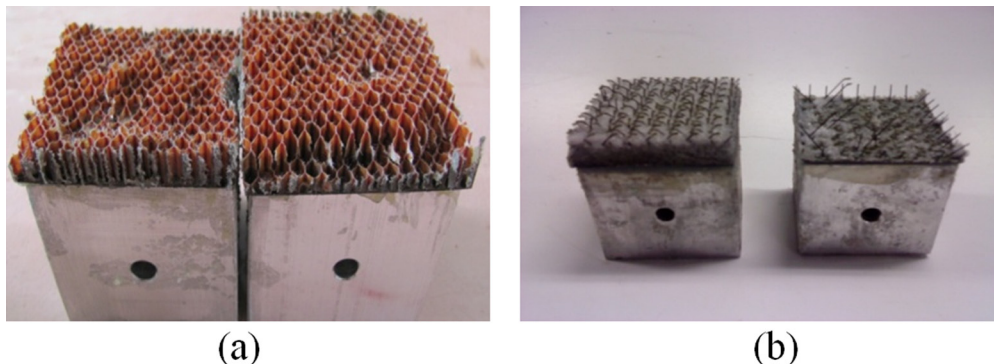


Figure 5. Failure Surface of Panels with (a) Nomex Core (b) K-COR under FWT.

facial bonds. This core-to-facesheet bond integrity is necessary to maintain stability and load transfer between the facesheet and the core. The flatwise tensile test is carried out in accordance with ASTM C 297 test method in which a sandwich specimen is subjected to uniaxial tension normal to the plane of the sandwich. The tensile load is transmitted onto the specimen through thick aluminum loading blocks. The facesheets are bonded to the loading tabs using Loctite Epoxy Plastic Bonder and cured at room temperature for 24 hours. In this test, specimen and fixture alignment is important to keep the bonded facings flat under load. Failure of the epoxy bond holding the specimen and loading tabs is considered invalid [5]. A total of four sandwich panels each of Nomex and K-COR were tested on an Instron 4469 model with 50 kN load cell. A constant crosshead speed of 0.5 mm/min was used. The FWT strength ( $\sigma$ ) values for each panel are shown in Table 2.

$$\sigma = \frac{P}{lw} \quad (4)$$

where,

- $\sigma$  = flatwise tensile strength
- $P$  = ultimate load
- $l$  = length of the specimen (2")
- $w$  = width of the specimen (2")

In the case of Nomex honeycomb sandwich panels failure was observed in the core. This was due to the lower tensile strength of the core compared to the bond strength at the core-to-facesheet interphase. Brittle failure was observed in the center of the sandwich structure with no core-facesheet debonding. In the case of K-COR pinned foam core sandwich panels the failure was observed at the core-to-facesheet interphase. Failure in these panels was also characterized by debonding of the pins from the facesheets resulting in pull out of some pins from the foam core. Similar behavior was observed in a study conducted by Marasco *et al.* [5]. The failure surfaces of FWT test samples for Nomex and K-COR are shown in Figure 5. The load vs extension graphs (Figure 7)

**Table 2. Flatwise Tensile Strength Results.**

Panel No.	Core Type	FWT Strength psi (MPa)
1	Nomex	631.54 (4.35)
2	Nomex	735.9 (5.07)
3	Nomex	788.25 (5.43)
4	Nomex	619.46 (4.27)
5	K-COR	426.845 (2.94)
6	K-COR	458.255 (3.16)
7	K-COR	467.11 (3.22)
8	K-COR	494.96 (3.41)

show plastic behavior in the initial portion. This region was found to be a result of slack present in the testing fixture which can be removed by pre-loading the specimen.

#### 4.2. Finite Element Modeling

Both Nomex and K-COR based finite element models were subjected to flatwise tension by loading the top facesheet and constraining the bottom facesheet. The material properties required for the simulation are shown in Table 1. Figures 6(a) and 6(b) show the failure in Nomex and K-COR sandwich structures as a result of flatwise tensile loading. Similar to the experimental results, the finite element simulation could predict failure of core in Nomex core sandwich structure and adhesive failure in K-COR sandwich structure.

The force vs. extension behavior of both the models were captured and compared with experimental results. The finite element results were similar to the experimental results except that the extension was slightly under-predicted. Figures 7(a) and 7(b) show the comparison of load-extension behavior between finite element results and experimental results, for Nomex and K-COR sandwich structures respectively. The peak loads predicted from the finite element simulation were matching well with experimental results. However, plastic behavior of load vs. extension in both Nomex and

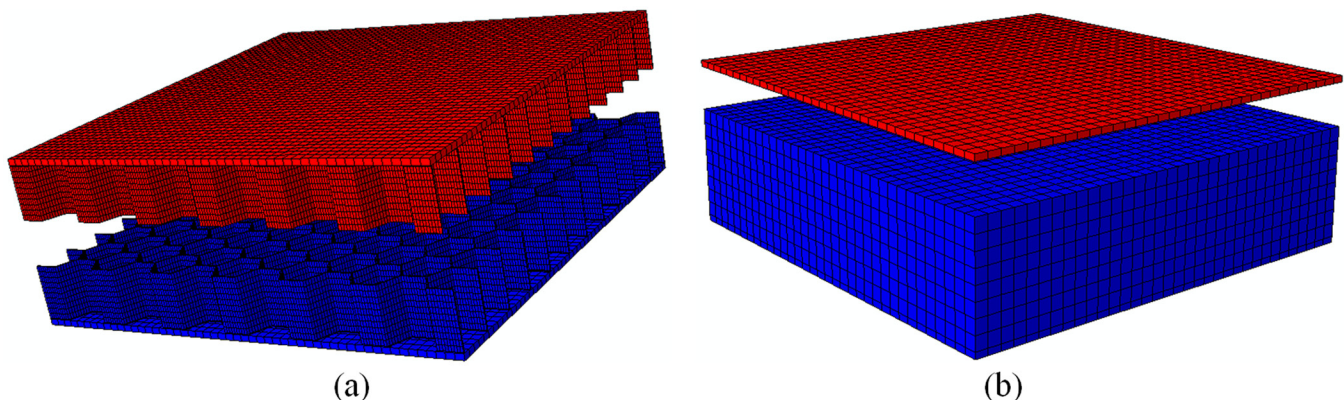


**Figure 6. Flatwise Tensile Failure in (a) Nomex Core, and (b) K-COR Sandwich Structures.**

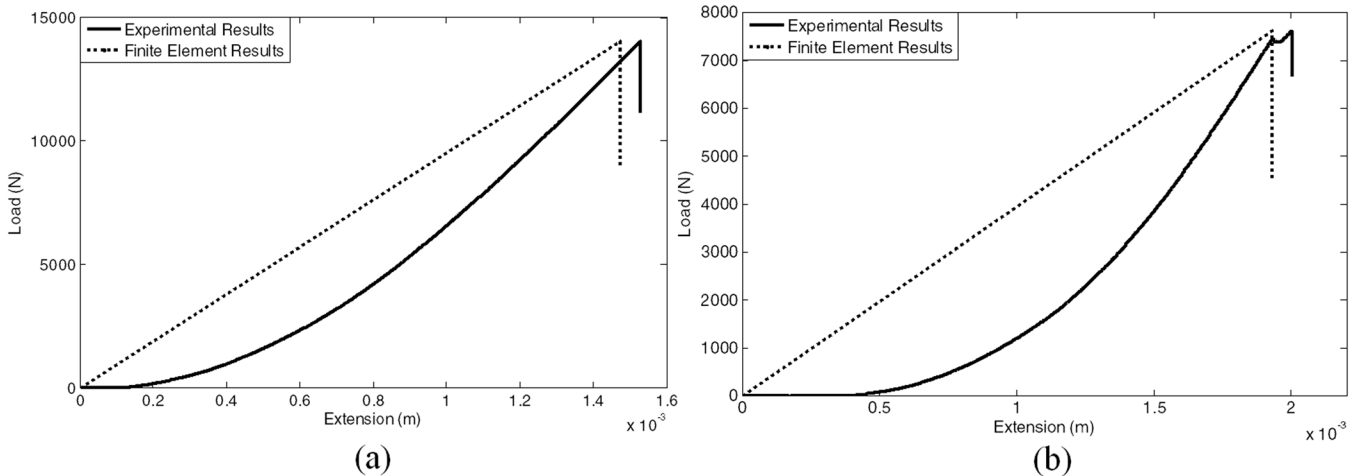


Figure 7. Finite Element Results vs. Experimental Results for (a) Nomex Core, and (b) K-COR Sandwich Structures.

K-COR sandwich structures from experimentation was not observed in simulation.

## 6. CONCLUSIONS

The OOA process was successfully used to manufacture Nomex honeycomb and K-COR foam core sandwich structures. The manufactured panels were evaluated under flatwise tension to determine the interfacial bond strength. It was observed that in the case of Nomex honeycomb sandwich panel, the failure occurs in the core itself, due to the lower tensile strength of the core when compared to interfacial bond strength. In the case of K-COR pinned foam core sandwich panels, failure was observed at the core-to-facesheet interphase. Failure in these panels was also characterized by debonding of the pins from the facesheets resulting in pull out of some of these pins from the foam core. Comprehensive finite element models were developed for both Nomex and K-COR sandwich structures and simulated for delamination failure using cohesive damage modeling approach. The finite element results were compared with experimental results and results were found to be in good agreement.

## REFERENCES

- [1] Schubel, P., Luo, J., and Daniel, I., "Low Velocity Impact Behavior of Composite Sandwich Panels," *Composites Part A: Applied Science and Manufacturing* Vol. 36, pp. 1389–1396, 2005. <http://dx.doi.org/10.1016/j.compositesa.2004.11.014>
- [2] Vaidya, U.K., Palazotto, A.N., and Gummedi, L.N.B., "Low Velocity Impact and Compression-After-Impact Response of Z-Pin Reinforced Core Sandwich Composites," *Journal of Engineering Materials and Technology*, Vol. 122, pp. 434–442, 2000. <http://dx.doi.org/10.1115/1.1289141>
- [3] Butukuri, R., Bheemreddy, V., Chandrashekhara, K., Berkel, T.R., and Rupel, K., "Evaluation of Skin-Core Adhesion Bond of Out-of-Autoclave Honeycomb Sandwich Structures," *Proceedings of the SAMPE Conference, Long Beach, CA, May 23–26*, pp. 1–11, 2011.
- [4] Khan, S., "Bonding of Sandwich Structures—The Facesheet/Honeycomb Interphase—A Phenomenal Study," E.I.DuPont de Nemours Co., Inc.
- [5] Marasco, A.I., Cartie, D.D.R., Partridge, I.K., and Rezai, A., "Mechanical Properties Balance in Novel Z-Pinned Sandwich Panels: Out-of-plane Properties," *Composites Part A: Applied Science and Manufacturing*, Vol. 37, pp. 295–302, 2006. <http://dx.doi.org/10.1016/j.compositesa.2005.03.029>
- [6] Grunenfelder, L., and Nutt, S., "Out-Time Effects on VBO (Vacuum Bag Only) Prepreg and Laminate Properties," *Proceedings of the SAMPE Conference, Long Beach, CA, May 23–26*, pp. 1–12, 2011.
- [7] Hou, T., Baughman, J., Zimmerman, T., Sutter, J., and Gardner, J., "Evaluation of Sandwich Structure Bonding in Out-of-Autoclave (OOA) Processing," *Proceedings of the 42nd International SAMPE Technical Conference, Salt Lake City, UT, October 11–14*, pp. 1–12, 2010.
- [8] Kratz, J., and Hubert, P., "Out-of-Autoclave Manufacturing of Composite Aircraft Sandwich Structures," *Proceedings of the 17th International Conference on Composite Materials, Edinburgh, United Kingdom, July 27–31*, pp. 1–10, 2009. PMID:19185771
- [9] Centea, T., and Hubert, P., "Measuring the Impregnation of Out-of-autoclave Prepreg by Micro-CT," *Composites Science and Technology*, Vol. 71, pp. 593–599, 2011. <http://dx.doi.org/10.1016/j.compscitech.2010.12.009>
- [10] Daniel, I.M., Gdoutos, E.E., Wang, K.A., and Abot, J.L., "Failure Modes of Composite Sandwich Beams," *International Journal of Damage Mechanics*, Vol. 11, pp. 309–334, 2002. <http://dx.doi.org/10.1106/105678902027247>
- [11] Avery, J.L., and Sankar, B.V., "Compressive Failure of Sandwich Beams with Debonded Face-Sheets," *Journal of Composite Materials*, Vol. 34, pp. 1176–1199, 2000. <http://dx.doi.org/10.1177/002199830003401402>
- [12] Mahfuz, H., Islam, S., Saha, M., Carlsson, L., and Jeelani, S., "Buckling of Sandwich Composites: Effects of Core-Skin Debonding and Core Density," *Applied Composite Materials*, Vol. 12, pp. 73–91, 2005. <http://dx.doi.org/10.1007/s10443-004-6138-9>
- [13] Vadakke, V., and Carlsson, L.A., "Experimental Investigation of Compression Failure of Sandwich Specimens with Face/Core Debond," *Composites: Part B*, Vol. 35, pp. 583–590, 2004. <http://dx.doi.org/10.1016/j.compositesb.2003.10.004>
- [14] Burlayenko, V.N., and Sadowski, T., "Influence of Skin/Core Debonding on Free Vibration Behavior of Foam and Honeycomb Cored Sandwich Plates," *International Journal of Non-Linear Mechanics*, Vol. 45, pp. 959–968, 2010. <http://dx.doi.org/10.1016/j.ijnonlinmec.2009.07.002>
- [15] Majumdar, P., Srinivasaguptha, D., Mahfuz, H., Joseph, B., Thomas, M.M., and Christensen, S., "Effect of Processing Conditions and Ma-

- terial Properties on The Debond Fracture Toughness of Foam-Core Sandwich Composites: Experimental Optimization,” *Composites: Part A, Vol. 34*, pp. 1097–1104, 2003. [http://dx.doi.org/10.1016/S1359-835X\(03\)00207-0](http://dx.doi.org/10.1016/S1359-835X(03)00207-0)
- [16] Veazie, D.R., Robinson, K.R., and Shivakumar, K., “Effects of the Marine Environment on the Interfacial Fracture Toughness of PVC Core Sandwich Composites,” *Composites: Part B, Vol. 35*, pp. 461–466, 2004. <http://dx.doi.org/10.1016/j.compositesb.2003.09.004>
- [17] Saha, M.C., Kabir, E., and Jeelani, S., “Study of Debond Fracture Toughness of Sandwich Composites with Nanophased Cores,” *Materials Letters, Vol. 62*, pp. 567–570, 2008. <http://dx.doi.org/10.1016/j.matlet.2007.06.017>
- [18] Grove, S., Popham, E., and Miles, M., “An Investigation of the Skin/Core Bond in Honeycomb Sandwich Structures using Statistical Experimentation Techniques,” *Composites Part A: Applied Science and Manufacturing, Vol. 37*, pp. 804–812, 2006. <http://dx.doi.org/10.1016/j.compositesa.2005.07.005>
- [19] Hayes, B., Seferis, J., and Edwards, R., “Self-adhesive Honeycomb Prepreg Systems for Secondary Structural Applications,” *Polymer Composites, Vol. 19*, pp. 54–64, 1998. <http://dx.doi.org/10.1002/pc.10075>
- [20] Rion, J., Leterrier, Y., and Manson J., “Prediction of the Adhesive Fillet Size for Skin to Honeycomb Core Bonding in Ultra-light Sandwich Structures,” *Composites Part A: Applied Science and Manufacturing, Vol. 29*, pp. 1547–1555, 2008. <http://dx.doi.org/10.1016/j.compositesa.2008.05.022>
- [21] Borst, R., “Some Recent Issues in Computational Failure Mechanics,” *International Journal for Numerical Methods in Engineering, Vol. 52*, pp. 63–95, 2001. <http://dx.doi.org/10.1002/nme.272>
- [22] Diehl, T., “On Using a Penalty-Based Cohesive-Zone Finite Element Approach: Part II: Inelastic Peeling of an Epoxy-Bonded Aluminum Strip,” *International Journal of Adhesion and Adhesives, Vol. 28*, pp. 256–265, 2008. <http://dx.doi.org/10.1016/j.ijadhadh.2007.06.004>
- [23] Wimmer, G., Schuecker, C., and Pettermann, H.E., “Numerical Simulation of Delamination in Laminated Composite Components—A Combination of a Strength Criterion and Fracture Mechanics,” *Composites Part B: Engineering, Vol. 40*, pp. 158–165, 2009. <http://dx.doi.org/10.1016/j.compositesb.2008.10.006>
- [24] Kozak, V., “Cohesive Zone Modeling,” *International Conference on Numerical Analysis and Applied Mathematics*, Psalidi, Kos, Greece, September 16–20, pp. 328–331, 2008.
- [25] Rahul Kumar, P., Jagota, A., Bennison, S., and Saigal, S., “Cohesive Element Modeling of Viscoelastic Fracture: Application to Peel Testing of Polymers,” *International Journal of Solids and Structures, Vol. 37*, pp. 1873–1897, 2000. [http://dx.doi.org/10.1016/S0020-7683\(98\)00339-4](http://dx.doi.org/10.1016/S0020-7683(98)00339-4)
- [26] ASTM C297, “Standard Test Method for Flatwise Tensile Strength of Sandwich Constructions.” *ASTM International 20*, pp. 1–6, 2004.
- [27] Sharkey, C., Kwon, S.W., Lee, S.W., Brunk, H.A., Rahman, A., and Barrett, D., “Mechanical Characterization and Modeling of X- and K-COR Composites,” *Proceedings of the SEM Annual Conference, Indianapolis, Indiana, June 7–10*, pp. 397–404, 2010.
- [28] Virakthi, A., “Stiffness and Strength of K-COR Sandwich Structures under Compression and Shear Loading Conditions,” M.S. Thesis, 2011.
- [29] Marasco, A., “Analysis and Evaluation of Mechanical Performance of Reinforced Sandwich Structures: X-Cor and K-Cor,” Ph.D. Thesis, 2005.
- [30] ABAQUS/Standard User's Manual, Vol. I and II (ver. 6.10), 2010. Hibbit, Karlsson and Sorensen, Inc., Pawtucket, Rhode Island.
- [31] Turon, A., Davila, C., Camanho, P., and Costa, J., “An Engineering Solution for Mesh Size Effects in the Simulation of Delamination using Cohesive Zone Models,” *Engineering Fracture Mechanics, Vol. 74*, pp. 1665–1682, 2007. <http://dx.doi.org/10.1016/j.engfracmech.2006.08.025>
- [32] Yarrington, P., Zhang, J., Collier, C., and Bednarczyk, B., “Failure Analysis of Adhesively Bonded Composite Joints,” *Collection of Technical Papers—AIAA/ASME/ASCE/AHS/ASC Structures, Structural Dynamics and Materials Conference, Vol. 10*, pp. 6972–6994, 2005.
- [33] Mancha, A., “Optimization of Lightweight Sandwich Structures of Commercial Aircraft Interior Parts Subjected to Low-Velocity Impact,” Diploma Thesis, June 2012.
- [34] Agarwal, B., Broutman, L., and Chandrashekhara, K., “Analysis and Performance of Fiber Composites,” Third Edition, John Wiley and Sons, Inc., Hoboken, New Jersey, 2006.



## Damage Investigation in Beam Structures using Fiber Optic Polarimetric Sensors

MUNEESH MAHESHWARI<sup>1,\*</sup>, SWEE CHUAN TJIN<sup>2</sup> and A. K. ASUNDI<sup>1</sup>

<sup>1</sup>Centre for Optical and Laser Engineering, School of Mechanical and Aerospace Engineering, Nanyang Technological University, 50 Nanyang Avenue, Singapore 639798

<sup>2</sup>School of Electrical and Electronic Engineering, Nanyang Technological University, 50 Nanyang Avenue, Singapore 639798

### KEYWORDS

fiber optic polarimetric sensor  
non-destructive testing  
structural health monitoring  
real time  
crack length and location

### ABSTRACT

The Fiber Optic Polarimetric Sensor (FOPS) is an attractive technology for global damage detection of mechanical and civil structures providing real time structural health monitoring (SHM). In this technology the concept of a Dynamic damage factor (DDF) was proposed [3] as a global health indicator of the structure. However, the crack size and location could not be determined. In this paper, the effects of the size and the location of a single crack on the frequency of first fundamental mode of beam structures are further studied. The relation between relative change in the modal frequency and the relative size of a crack has been established theoretically and then verified experimentally. Experimental results confirm that the change in frequency of first mode provides damage information of structure. It is further shown that the size and location of a crack in the beam structures can also be identified.

© 2014 DEStech Publications, Inc. All rights reserved.

## 1. INTRODUCTION

Fiber Optic Sensors (FOSs) have a lot of advantages over the other sensors, for instance, piezo-electric sensors. FOSs are light weight, insensitive to electromagnetic interference and have small footprint. These sensors can be easily embedded into composite and civil structures for structural health monitoring (SHM). Metal structures do not allow fibers to be embedded, so in this case FOSs are surface mounted. Conventional methods do not allow real-time on-line health monitoring as they are time consuming and require a lot of data processing [1]. FOS makes such real-time online structural health monitoring very easy and effective. In most of the cases, structural integrity of the structures is very important without being influenced by other sensors. There are a number of NDT methods, such as acoustic emission (AE), ultrasonic scanning, shearography etc., but these classical NDT techniques are not capable of providing online structural health monitoring, because it is very difficult to get real-time data from them [2].

Different types of fiber optic sensing techniques are available for structural health monitoring methods. Extrinsic Fabry-Perot interferometer (EFPI) and Fiber Bragg Grating (FBG) sensors are used for local measurement. Multiplexing allows these techniques for data capture at multiple points. But additional data analysis is needed to relate these values to the structural health. Fiber Optic Polarimetric Sensors (FOPSs) are the best suited for global and dynamic health monitoring. Using FOPSs, both static and dynamic tests can be performed for the global health monitoring of different engineering structures.

A quantitative study, using FOPS, was performed for structural health monitoring and two factors; Static Damage Factor (SDF) and Dynamic Damage Factor (DDF), were proposed [3]. The DDF was a preferred choice as it allowed for testing *in-situ*. Essentially, structural damage results in a loss of stiffness and hence a change in the modal frequency. The ratio of change in frequency for a damaged structure to an undamaged one is the DDF. However the DDF is not unique and dependent on the damage location, size and number. Thus while indicative and fast, further systematic studies have to be performed to effect practical implemen-

\*Corresponding author. Email: [muneesh29phy@gmail.com](mailto:muneesh29phy@gmail.com)

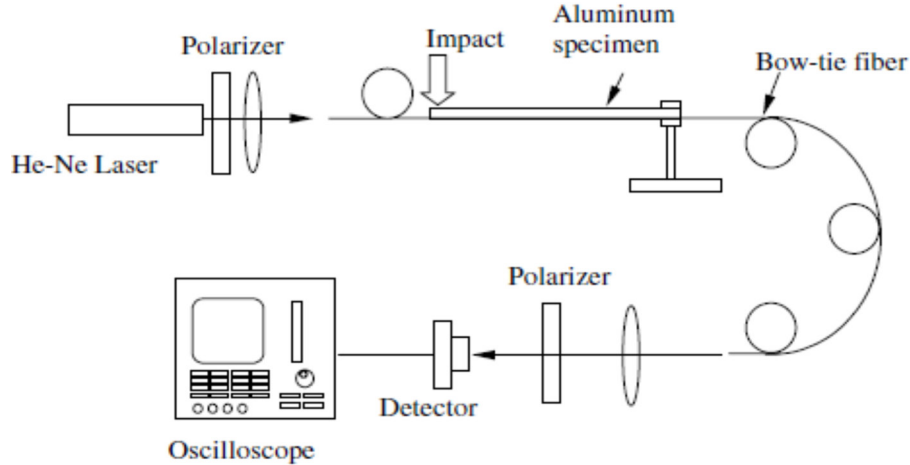


Figure 1. Schematic of FOPS for dynamic testing.

tation. In this paper, a study of the size and location of a single crack on the modal frequencies of beam structures, using FOPS, is presented. A relation between the normalized change in the frequency of the first fundamental mode of different beam structures and relative crack size is established. Some well-designed sets of experiments are performed to verify this relationship.

## 2. PRINCIPLE

### 2.1. Crack Analysis by Dynamic Test Using FOPS

A polarization maintaining fiber (Hi-Bi fiber) is used as the sensing fiber in the FOPS method. The Hi-Bi fiber has two axes—fast and slow axis. If linearly polarized light is launched into the Hi-Bi fiber in such a way that its polarization is either along fast axis or slow axis, the Hi-Bi fiber is insensitive to external perturbations. On the other hand, if polarized light equally populates the two axes, the fiber has maximum sensitivity to external changes. As the light traverses the Hi-Bi fiber, the state of polarization of light changes from linear to circular and back to linear over a short distance (called the beat length) within the fiber. Strain on any portion of the fiber causes the beat length to change and hence changes the output state of polarization. The change can be either due to static or dynamic load on the fiber or other changes in environmental conditions. Indeed the entire fiber is sensing. In case of dynamic studies, the strain changes periodically at a rate dependent on the external stimulus. Hence the state of polarization also cycles at the same frequency. Measuring this frequency allows us to measure the dynamic characteristics of the structure.

The schematic of the FOPS set-up for dynamic test is shown in the Figure 1. A half wave plate (polarizer) is used to change the polarization of laser light such that equally populates the two modes in the Hi-Bi fiber. The Hi-Bi fiber is bonded to an aluminium cantilever beam to follow

the strain in the beam. The state of polarization of the light emerging from the fiber is analysed via a second polarizer and a detector.

The frequency of  $n$ th fundamental mode of a cantilever is given as [3].

$$f_n = \left[ a \frac{(2n-1)\pi}{2} \right]^2 \sqrt{\frac{EI}{A}} \quad (1)$$

From Equation (1), it can be clearly seen that the frequency of fundamental modes depends on the flexural stiffness ( $EI$ ) of the cantilever. If the cantilever is damaged, the stiffness will reduce and hence, the frequency of fundamental mode reduces.

Theoretically, a crack can be modelled as massless linear spring [4] of stiffness  $K_x$  as shown in Equation (2). The change in the frequency of any fundamental mode is given as [5]:

$$\frac{\Delta f_n}{f_n} = \sin^2 \left( \frac{n\pi x}{2L} \right) \frac{EI}{K_x L} \quad (2)$$

where  $EI$  is the stiffness,  $L$  is the length of the cantilever and  $x$  represents a non-dimensional crack location and it is the function of distance ( $l$ ) of the crack from the fixed end. The stiffness  $K_x$  of the spring is given as [6]:

$$K_x = \frac{EI}{(5.346h) \cdot f(a/h)} \quad (3)$$

where  $h$  is the height,  $a$  is the size of the crack and the function  $f(a/h)$  is given by:

$$\begin{aligned} f(a/h) = & 1.8624(a/h)^2 - 3.95(a/h)^3 + 16.375(a/h)^4 \\ & - 37.226(a/h)^5 + 78.81(a/h)^6 - 126.9(a/h)^7 + 172(a/h)^8 \\ & - 143.97(a/h)^9 + 66.56(a/h)^{10} \end{aligned} \quad (4)$$

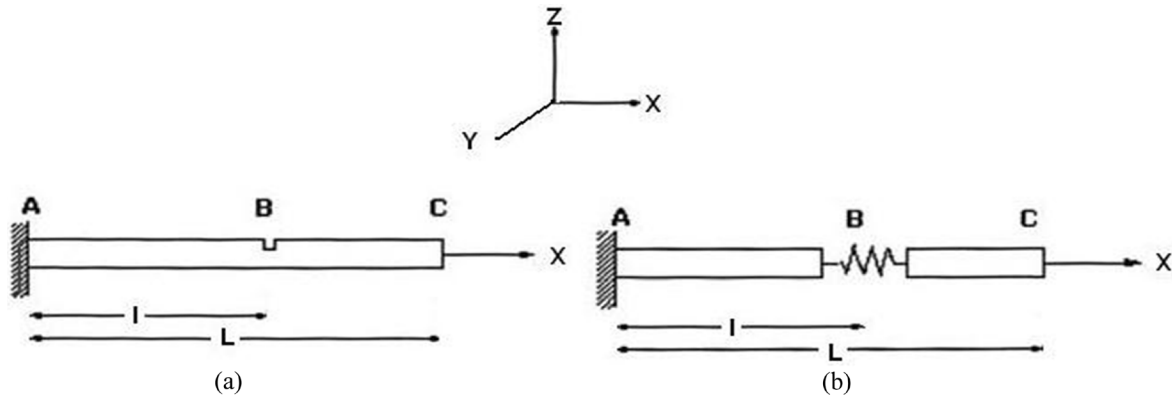


Figure 2. (a) An aluminium cantilever with a single crack and (b) model of cracked cantilever beam.

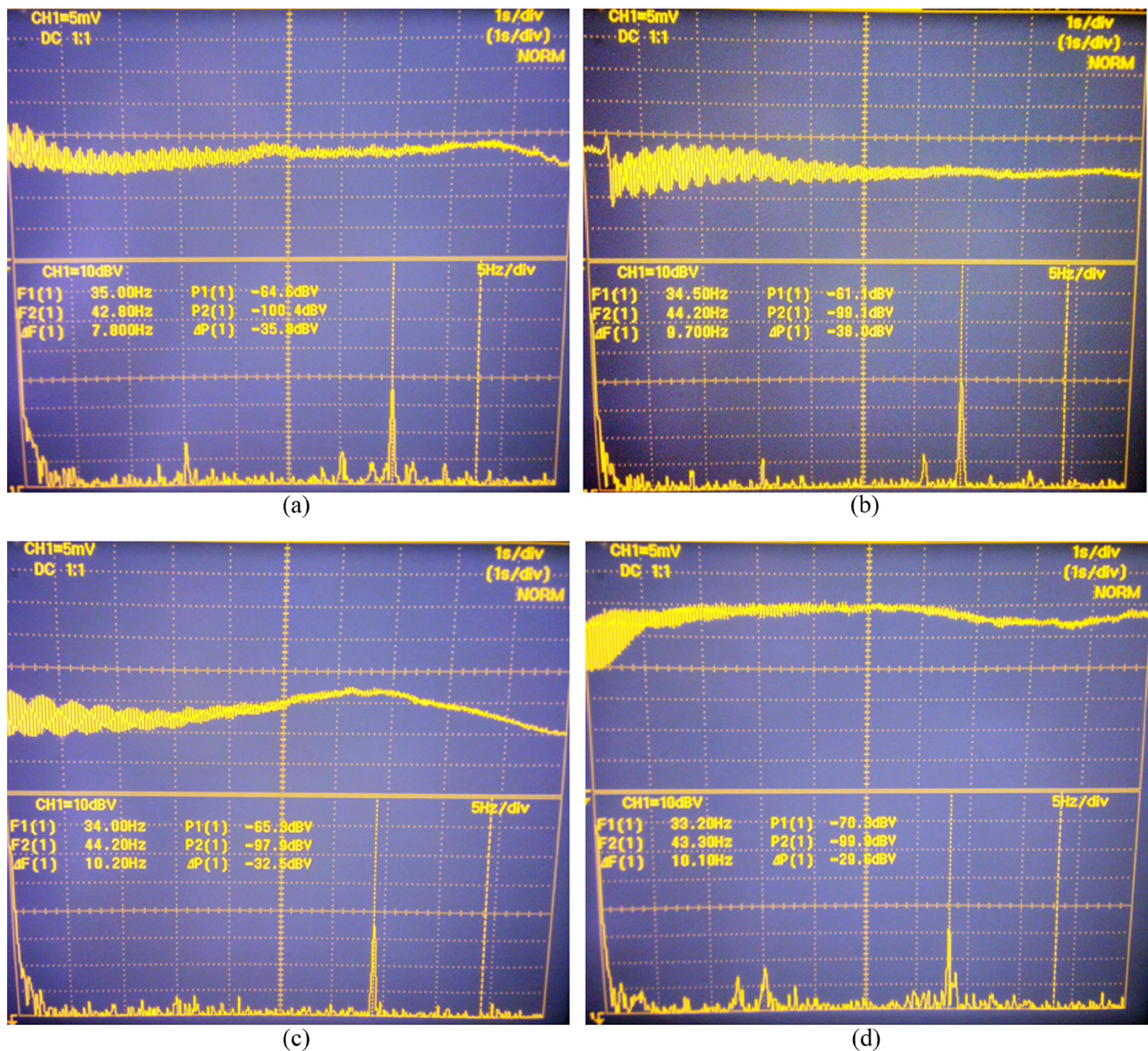


Figure 3. Oscilloscope traces showing the frequencies of first fundamental mode of the cantilever with crack location is 2 cm and crack size is (a) no crack, (b) 3 mm, (c) 6 mm, (d) 8.5 mm.

As the ratio  $a/h$  is small, higher orders of  $a/h$  can be neglected. Hence Equation (4) reduces to:

$$f(a/h) \approx 1.8624(a/h)^2 \quad (5)$$

From Equations (2) and (3) we have:

$$\frac{\Delta f_n}{f_n} = \sin^2\left(\frac{n\pi x}{2L}\right) \frac{5.346 \cdot h \cdot f(a/h)}{L} \quad (6)$$

Equation (6) suggests that the change in natural frequency depends both on the location and size of the crack. Equations (5) and (6) suggest that  $\Delta f_n/f_n$  is a quadratic function of  $a/h$ . For other beam structures the form of  $x$  in Equation (6) changes, but the form of equation remains the same.

### 3. EXPERIMENTAL RESULTS AND DISCUSSION

#### 3.1. Experimental Verification of Single Crack Theory by FOPS

An experiment was performed on an aluminium cantilever, size  $268 \times 19 \times 3.2 \text{ mm}^3$  to test the validity of this approach. A short impact force generates the vibration modes in the specimen which is detected by the fiber, Figure 2. A crack was sawed at different locations with different lengths to simulate various levels and severity of damage. The frequency of first mode was recorded for each test on undam-

aged and damaged specimens. Figure 3 shows the oscilloscope traces showing the first fundamental frequencies (F1 cursor) with a fixed crack location at 2 cm from the fixed end of the cantilever, but with different crack sizes. F2 cursor is not used in this experiment.

Figure 4 shows the relative change in the frequency ( $\Delta f_1/f_1$ ) of first fundamental mode with relative crack size ratio (ratio of the crack size  $a$  to the total height  $h$  of the cantilever beam) at different crack locations. For small ( $a/h$ ) values, Equations (5) and (6) indicate that the quantity  $\Delta f_n/f_n$  is a quadratic function of ( $a/h$ ). From Figure 5, it can be seen that the distribution of the functions  $\Delta f_1/f_1$  is quadratic and has the form  $A(a/h)^2 + B(a/h) + C$ , the coefficient  $B$  and  $C$  are very small in comparison to coefficient  $A$ . Hence, the term ( $a/h$ ) and constant  $C$  can be neglected. The presence of coefficients  $B$  and  $C$  could be because of the experimental errors such as variations in boundary condition, the resolution of oscilloscope. Hence it can be inferred that the function  $\Delta f_1/f_1$  follows the relation established in Equations (5) and (6).

For different crack sizes, the change in the frequency of first fundamental mode ( $\Delta f_1$ ) of a cantilever has been plotted against the relative crack location ( $l/L$ ) from the fixed end of the cantilever in Figure 6. Clearly from Figure 6, the change in the modal frequency ( $\Delta f_1$ ) is larger when crack is closer to the fixed end. This is since the strain is highest at the fixed end and any damage at the fixed end would induce larger changes in stiffness and hence higher changes in the frequency mode.

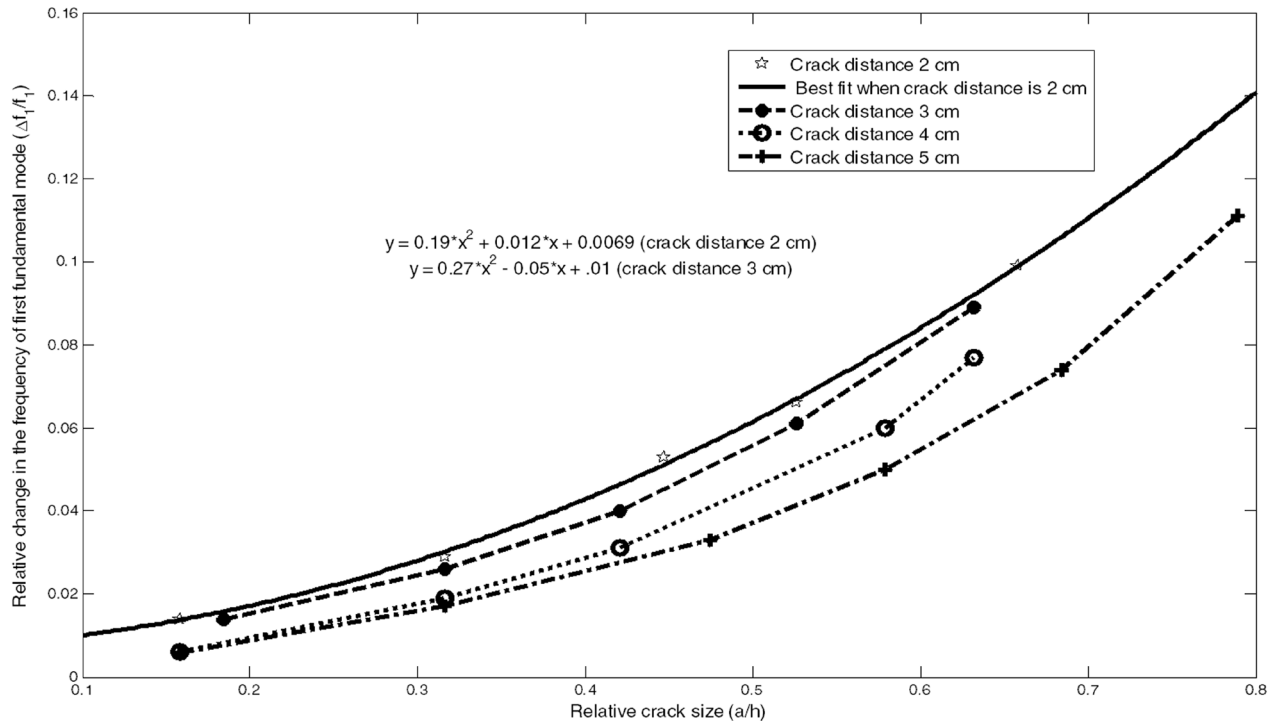


Figure 4. Relative change in the first fundamental frequency ( $\Delta f_1/f_1$ ) with relative crack size ( $a/h$ ) at different crack locations for a cantilever.

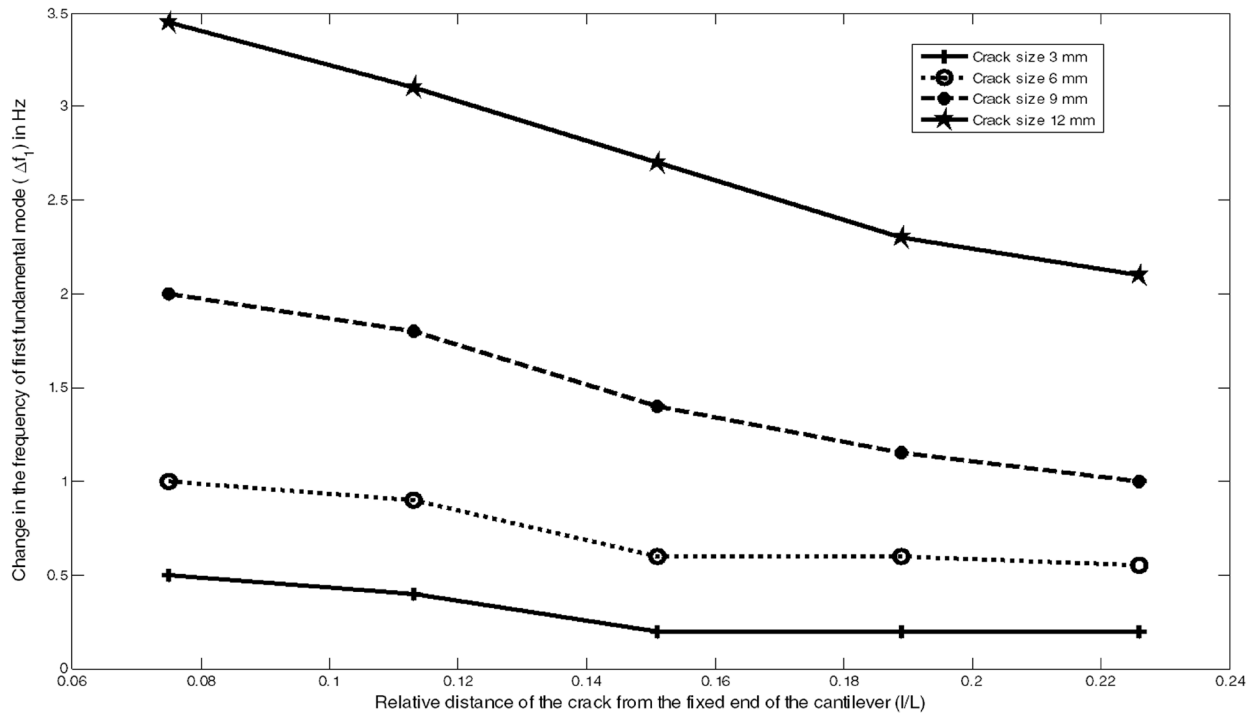


Figure 5. Change in the first fundamental frequency ( $\Delta f_1$ ) with relative position ( $l/L$ ) of a crack with different crack sizes for a cantilever.

One very important observations is that the ranges of values of  $\Delta f_1$  in Figure 6 corresponding to different crack sizes, do not overlap, indicating no crack size discrepancy. A specific value of  $\Delta f_1$  belongs to a particular crack size most of

the times. In other words, the value of  $\Delta f_1$  gives us an indication of the crack size. This information could further be used with Figure 5 to calculate the approximate crack location.

As stated earlier, Equation (6) preserves its form for other

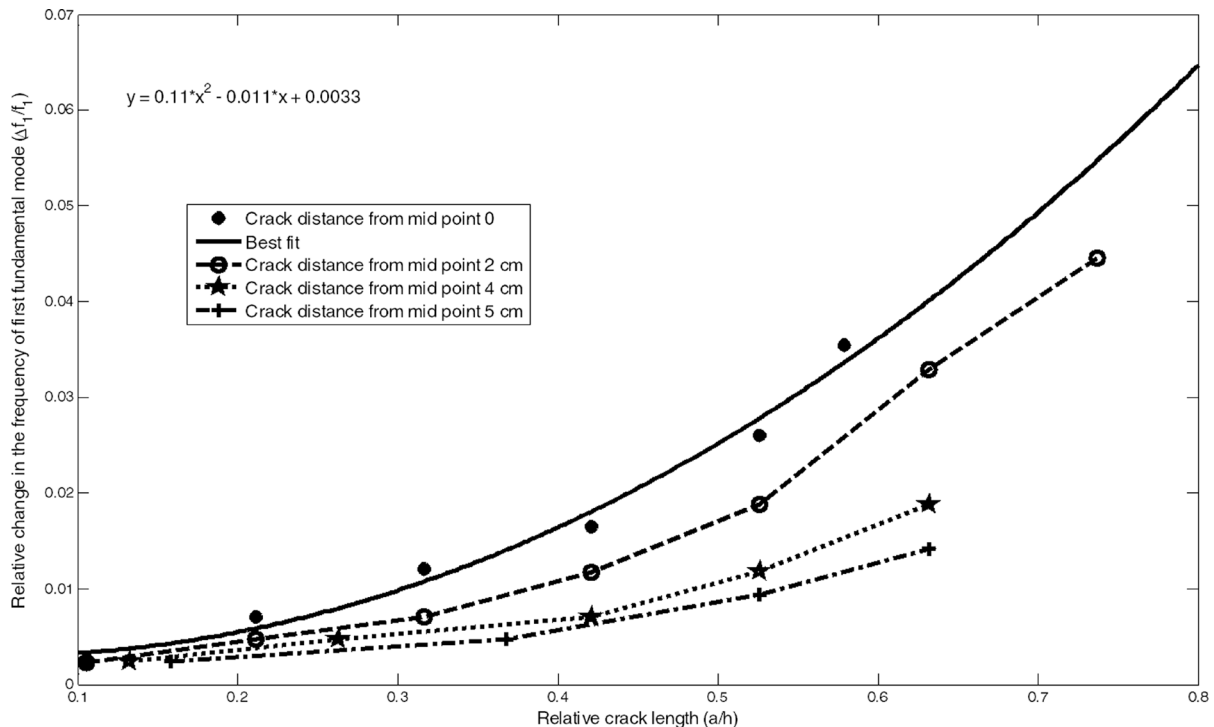
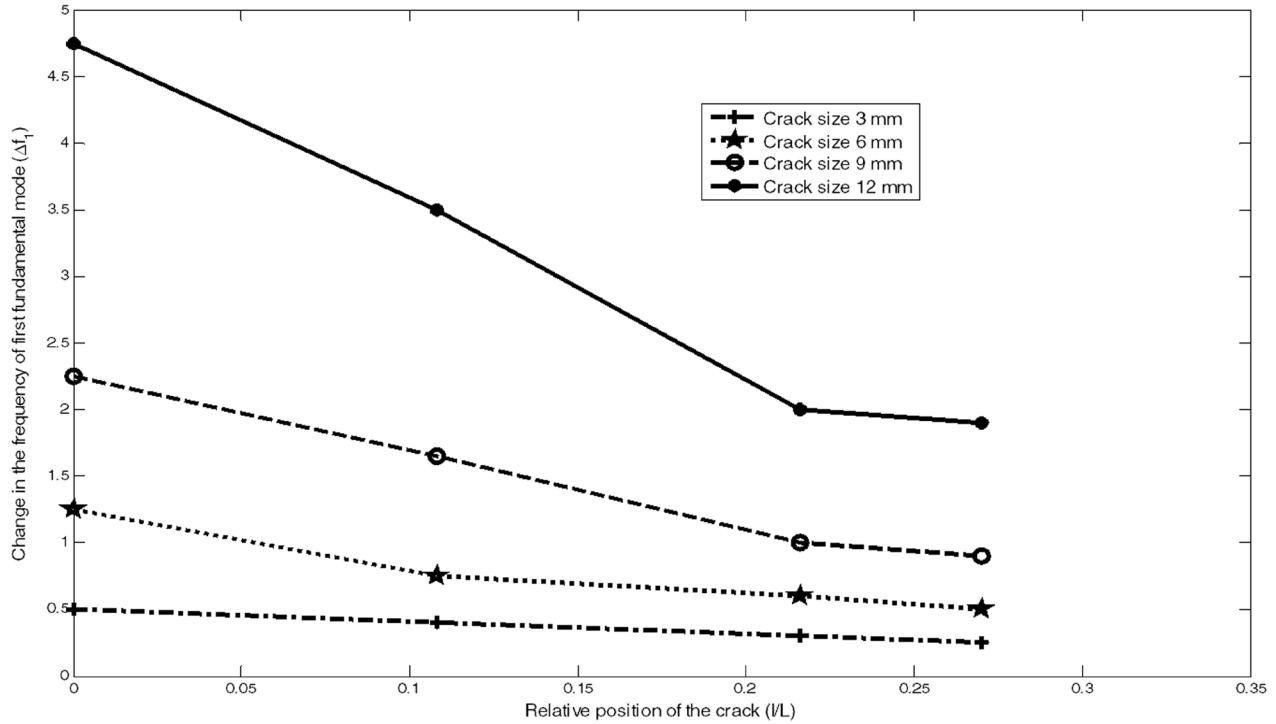


Figure 6. Relative change in the first fundamental frequency of a beam fixed at both ends with relative crack size at different crack locations.



**Figure 7.** Relative change in the first fundamental frequency of a beam fixed at both ends with relative position of a crack with different crack sizes.

beam structures. An experiment was performed for a beam fixed at both the ends. The size of the beam was  $370 \times 19 \times 3.2 \text{ mm}^3$ . The distance of crack was measured from the mid-point of the beam. Again from Figure 6, the relative change in the frequency ( $\Delta f_1/f_1$ ) follows the same relationship with relative crack length.

From Figure 7, the value of  $\Delta f_1$  is higher when the crack is close to the mid-point of the beam and decreases as the crack moves towards the fixed ends of the beam. Once again this suggests that stiffness changes are larger at points with greater strain. In this case, however, the values of  $\Delta f_1$  for different crack sizes overlap indicating some ambiguity in crack location determination.

#### 4. CONCLUSION

Experimental results show that the relative change in the frequency of fundamental mode of beam structures follows a pattern established by spring theory of a single crack. Also, the values of the change in frequency of first mode ( $\Delta f_1$ ) give very important information about the crack size and location. In fact by looking at the values of  $\Delta f_1$ , the size and location of the crack can be determined without ambiguity in

most cases. The study shows that the FOPS method has great potential in the field of SHM.

#### REFERENCES

- [1] Cooper T D, "Specialist comments: applied point of view," Proc. AGARD 462, R1.1–1.6 (1990)
- [2] J S Leng and A Asundi, "Non-destructive evaluation of smart materials by using extrinsic Fabry-Perot interferometric and fiber Bragg grating sensors," *NDT & E International* 35, 273–276 (2002). [http://dx.doi.org/10.1016/S0963-8695\(01\)00060-3](http://dx.doi.org/10.1016/S0963-8695(01)00060-3)
- [3] Jianjun Ma and Anand Asundi, "Structural health monitoring using a fiber optic polarimetric sensor and a fiber optic curvature sensor-static and dynamic test," *Smart Mater. Struct.* 10, 181–188 (2001). <http://dx.doi.org/10.1088/0964-1726/10/2/302>
- [4] T. G. Chondros and A. D. Dimarogonas, "Identification of Cracks in Welded Joints of Complex Structures," *Journal of Sound and Vibration* 69(4), 531–538 (1980). [http://dx.doi.org/10.1016/0022-460X\(80\)90623-9](http://dx.doi.org/10.1016/0022-460X(80)90623-9)
- [5] F. B. Sayyad and Bimlesh Kumar, "Approximate Analytical Method for Damage Detection in Beam," *International Journal of Damage Mechanics* 21, 1064–1075 (2012). <http://dx.doi.org/10.1177/1056789511429142>
- [6] Rizos, P.F. and Aspragathos, N., "Identification of Crack Location and Magnitude in a Cantilever Beam from the Vibration Modes," *Journal of Sound and Vibration*, 138(3), 381–388 (1990). [http://dx.doi.org/10.1016/0022-460X\(90\)90593-0](http://dx.doi.org/10.1016/0022-460X(90)90593-0)



## Effect of Coarse Filler on Shrinkages and Dynamic Mechanical Properties of Epoxy Grouts

MD SHAMSUDDOHA<sup>1,2,\*</sup>, MD MAINUL ISLAM<sup>1</sup>, THIRU ARAVINTHAN<sup>1</sup>, ALLAN MANALO<sup>1,2</sup> and KIN-TAK LAU<sup>1</sup>

<sup>1</sup>Centre of Excellence in Engineered Fibre Composites (CEEFC), Faculty of Engineering and Surveying, University of Southern Queensland, Toowoomba, Queensland 4350, Australia

<sup>2</sup>Cooperative Research Centre for Advanced Composite Structures (CRC-ACS), 1/320 Lorimer Street, Port Melbourne, Victoria 3207, Australia

### KEYWORDS

epoxy grout  
repair  
rehabilitation  
cure shrinkage

### ABSTRACT

Structures are designed and constructed for a certain lifetime based on its constituent materials, level of quality control, surrounding environment and accidental loads experienced during service. Structures that are situated in an adverse environment are susceptible to material loss and cracks over their ageing service life. Often, advanced composite materials offer substantially enhanced mechanical, durability and constructability related properties essential for durable repair of the deteriorated structure. Infill material is used to ensure a supporting bed for a grouted repair. Epoxy grouts are used for repairing and rehabilitating structures, such as foundations, bridges, piers, transportation pipelines, etc., because they are resistant to typical chemicals and possess superior mechanical properties than other grouts. The resin based infill used inside the void or cracked space of the repair is vulnerable to shrinkage. When these filled grouts have high resin content, cracks can develop from residual stresses, which can affect the load transfer performance. As a result, interlayer separation and cracking of infill layer can occur in a grouted repair. In this study, volumetric shrinkage of two epoxy grouts was measured over 28 days using a Pycnometer. The highest volumetric shrinkage measured after 7 days was found to be 2.72%. The results suggest that the volumetric shrinkage can be reduced to 1.1% after 7 days, through the introduction of a coarse aggregate filler; a 2.5 times reduction in shrinkage. About 98% and 92% of the total shrinkage over the 28 day period, of the unfilled and filled grouts respectively, was found to occur within 7 days of mixing. The gel-time shrinkages were calculated, to determine the "post-gel" part of the curing contraction which subsequently produces residual stresses in the hardened grout systems. The dynamic thermal behaviour of the grouts were also characterised to determine the range of in-situ application.

© 2014 DEStech Publications, Inc. All rights reserved.

## 1. INTRODUCTION

Structures can go through harsh environmental adversity and can experience material loss and cracks during their service lives. Hence, repair and rehabilitation are essential to retain these structures under service conditions. In repairing these structures, infill grouts are applied to fill

voids and cracks of the *in situ* materials and seal cracks to restore strength and stability. Cement grouts with or without polymer modifications and epoxy grouts are usually used in construction industry. Sometimes, epoxy grouts are recommended over the cement grouts for application requiring high strength, rapid setting, chemical stability, dynamic load bearing, alignment and handling versatility [1,2]. Epoxy resins are the most widely used polymers in the civil engineering and industrial fields. Conventionally, the epoxy resins

\*Corresponding author. Email: [Md.Shamsuddoha@usq.edu.au](mailto:Md.Shamsuddoha@usq.edu.au)

used in the civil engineering and industrial fields are the products of copolymerisation of Bisphenol A and Epichlorohydrin [3]. Structural grouts derived from epoxy resins, hardeners and fillers serve as protective layer and effective load transfer medium. They are used as infill in-between two layers requiring structural repair, rehabilitation and stabilisation for both existing and newly constructed structures.

It is evident from a number of studies that polymers experience shrinkage during its curing process. Internal stress, volumetric shrinkage and warpage are some of the inevitable issues in polymers during curing process [4–6]. Shrinkage during the curing process may result in uneven finish and separation of the adjoining surfaces, which eventually causes inefficient load transfer. As long as the resin system is liquid, it can accommodate the shrinkage. After a certain time, when polymer has reached a certain degree of polymerisation, it no longer flows to accommodate the shrinkage [7]. This is the “post-gel” part of the curing contraction, when the material is getting stronger to exert forces and thereby stress is being produced [8]. This post-gel shrinkage affects the development of stress in polymers [9–12]. The resin based infill used inside the annulus of the repair is vulnerable to shrinkage. Resin when used in high content can crack from the developed residual stresses and thus affect the load transfer performance. Thus, measures need to be taken to avoid excessive shrinkage that can create inter-layer separation and cracking of infill layer. In addition, an evaluation of the dynamic thermal properties of the grouts is also important, since polymers demonstrate degradation at elevated temperature. Dynamic thermal analysis (DMA) is often used to characterise the thermal range of applicability [13]. Therefore, it is essential to characterise the thermal properties as well as shrinkage properties of epoxy grouts to determine their efficiency in service conditions.

With the important role of epoxy grouts in structural re-

pair, this study was conducted to characterise the volumetric shrinkage of epoxy grouts with and without additional coarse filler and to determine the amount of shrinkage that will contribute to the rigid contraction. The effect of coarse filler in the shrinkage performance is also investigated. Finally, glass transition temperatures ( $T_g$ ) are determined from the mechanical behaviour of the grouts.

## 2. TEST PROGRAMME

### 2.1. Materials

Reduction of shrinkage is achievable possibly by modification of shrinkage properties through introduction of fillers in the resin [14,15]. Thus, a coarse filler was introduced to prepare a second grout system. The first grout consisted of high viscous resin with fine filler and low viscous hardener. This grout was claimed to have resistance against acids, bases and hydrocarbon based fluids thus advantageous for underground and underwater transportation facilities. The second grout was the modification of the first grout, which was mixed with an equal weight of coarse filler. Table 1 shows the proportions of the ingredients of the grouts. Due to commercial confidentiality, the grouts were investigated in this publication were named as grout A and B. The visible components of the grouts are shown in Figure 1.

### 2.2. Preparation of Specimens

The mixing and tests were undertaken at the Centre of Excellence in Engineered Fibre Composites (CEEFC) of University of Southern Queensland (USQ). The obtained bulk grout materials were stored based on suppliers' specifications. Initially, resin and hardeners were mixed volumetrically according to the guidelines stated in the respec-

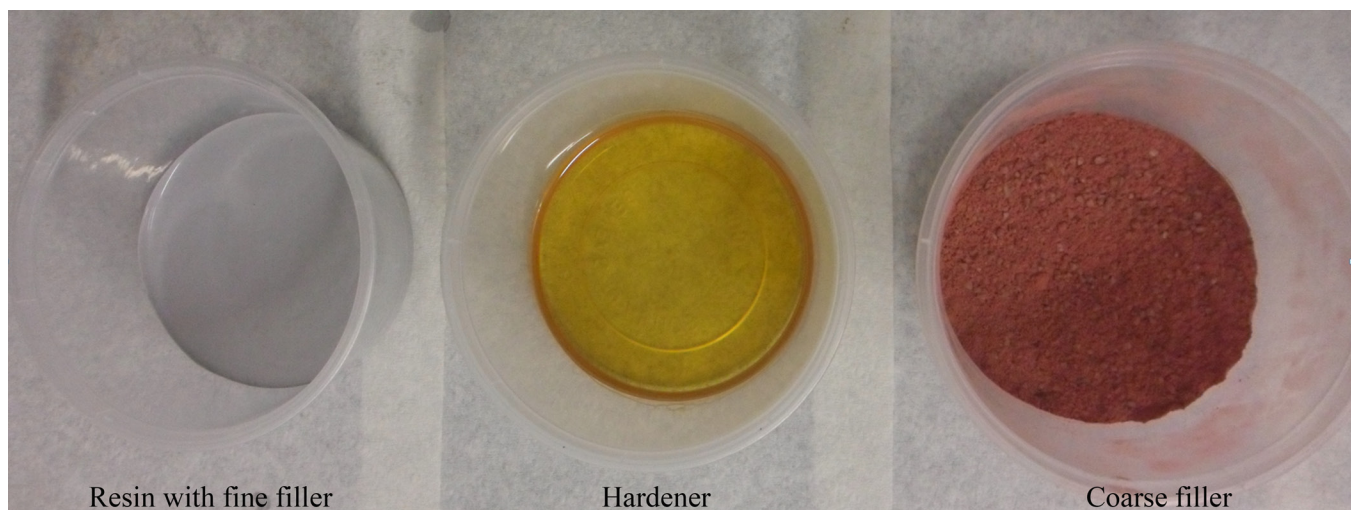


Figure 1. Components of the grouts.

**Table 1. Composition of the Grouts.**

Grouts	Part-components	Mixing Ratio	Primary Constituents <sup>f</sup> (Weight %)			
			Resin <sup>e</sup>	Hardener	Fine Filler	Aggregate Filler
A	Resin with fine filler <sup>a</sup> : Hardener	4.0:1.0 <sup>c</sup>	27.4 (49.3)	9.5 (20)	63.1 (30.7)	–
B	(Resin with fine filler <sup>a</sup> : Hardener): Coarse filler <sup>b</sup>	(4.0:1.0) <sup>c</sup> :1.0 <sup>d</sup>	13.7 (27.6)	4.8 (11.2)	31.6 (17.1)	50.0 (44.1)

<sup>a</sup>0.05–300.0  $\mu\text{m}$ , <sup>b</sup>0.45  $\mu\text{m}$ –2.36 mm, <sup>c</sup>by volume, <sup>d</sup>by weight, <sup>e</sup>DGBEA based epoxy, <sup>f</sup>Values in the parenthesis are volumetric contents

tive Technical Data Sheets (TDS) and Material Safety Data Sheets (MSDS). The coarse filler was added with freshly mixed grout A to obtain the second grout. The mix ratios are given in the Table 1. Figure 2 shows the mixing of initial grout A and then thorough mixing after adding the aggregate filler. Hand held electric drill mixer was used to mix the volumetric batch in a plastic container. Freshly mixed grouts were poured into containers within the required time and temperature limits prescribed in the application instructions. Grout A was found fairly low viscous whereas the coarse filled grout B was moderately viscous to mix, and so Grout A was easier to pour into the moulds during specimen preparation. Grout B with the aggregate filler exhibited more entrapped air bubbles than that without coarse filler.

### 2.3. Test Details

Pycnometer can be used to measure the volumetric shrinkage [16]. A Quantacrome Instruments Multipycnometer was used to measure the volume of the grouts. Freshly mixed grout was poured into a 75  $\text{cm}^3$  plastic containers. The container was filled with 73.5  $\text{cm}^3$  grout as a controlled volume. Density was then calculated from the controlled volume and weight. The shrinkages were calculated based on this initial density. The shrinkage quantification approach, expressed mathematically in Equation (1) as suggested by ISO 3521 [17], was used to determine the shrinkage of the grout, where  $\rho_c$  is the density of grout for a certain time, and  $\rho_o$  is the initial density of grout. The test apparatus and test samples of the shrinkage tests are shown in Figure 3. A minimum of three samples of the grouts were tested. Measurements were taken to determine the curing performance over 1, 3, 7, 14 and 28 days. Volumetric shrinkage was also determined over a 24

hour period along with gel time for each of the grouts. The gel time was determined as per ASTM D247118.

$$\Delta V = \frac{\rho_c - \rho_o}{\rho_c} \quad (1)$$

DMA is considered as the most suitable method to determine  $T_g$  for a filled thermoset matrix [19]. Hence, Dynamic Mechanical Analysis (DMA) was used to determine the glass transition temperatures of the grouts at 7 days. Rectangular specimens with nominal dimensions of 60 mm long, 12 mm wide and 4 mm thick were prepared for the DMA analysis. The specimens were clamped in the three-point bending fixture of the DMA apparatus. The dynamic mechanical analyser used to carry out the dynamic analysis was a calibrated DMA Q800 with Universal Analysis 2000 V5.1 Build 92 manufactured by TA Instruments. Figure 4 shows mounted specimens on the three point bending fixture prior to testing for DMA.

## 3. RESULTS AND DISCUSSION

### 3.1. Total Volumetric Shrinkage of Grouts

Table 2 shows the key summary of the volumetric shrinkage along with gel times. The range of shrinkage found from the literature for epoxy resins is 2–7% [20–22]. Thus, good agreement is found for the obtained values. From the results, it is apparent that the early curing governs the rate of shrinkage in the grouts. Higher exotherm temperature was also observed for grout A. The total shrinkages over 28 days were



**Figure 2.** Mixing of grouts.

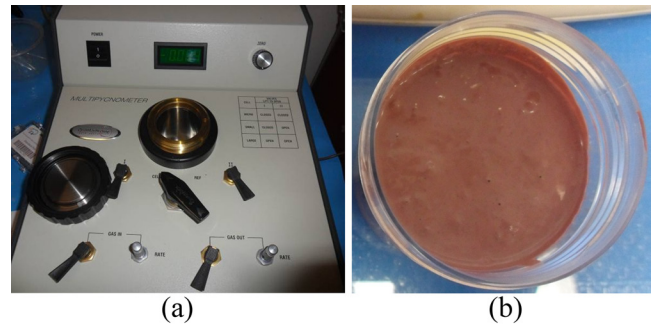


**Figure 3.** Shrinkage test apparatus and grout sample: (a) Pycnometer; (b) shrinkage specimens.

**Table 2. Summary of the Volumetric Shrinkage.**

Grout	Gel Time (min)	Duration				
		1-day	3-day	7-day	14-day	28-day
A	105	2.651 ± 0.337	2.670 ± 0.250	2.716 ± 0.361	2.742 ± 0.238	2.767 ± 0.268
B	165	0.899 ± 0.479	0.927 ± 0.490	1.005 ± 0.452	1.079 ± 0.444	1.091 ± 0.443

found to be 2.77% and 1.09% for grout A and B, respectively. The dominant period contributing to the major shrinkage was found to be 1 day. About 96% and 83% of the 28 day shrinkage of the grouts A and B, respectively, occurred within the first 24 hours of mixing, whereas about 98% and 92% of the 28 day shrinkage of the grouts A and B, respectively, occurred within the first 7 days. The gel times for grout A and B found to be 105 and 165 minutes, respectively.

The Pycnometer is a high precision instrument and determines the volume using Boyle's Law, which assumes the temperature as a constant [21]. Grout B exhibited a higher standard deviation than that of grout A. It is noted that during measurement the samples were still curing. Hence, the temperature can marginally affect the readings.

Another reason for the difference between grouts A and B is that air bubbles that were entrapped in the high viscous paste during mixing in the case of grout B. The bubbles can cause deviation in the obtained volume of the grout from Pycnometer.

### 3.2. Post-gel Shrinkage of Grouts

Figure 4 shows the average shrinkage distribution over the 28 days periods. The gel time shrinkages are also shown as dotted lines. The results suggested that grout A experienced more shrinkage than that of grout B at the early stage of curing. After 24 hours of mixing, the average shrinkages that may contribute to post-gel stress in grout A and B are approximately 2.53% and 0.21%, respectively, whereas the 28 day post-gel shrinkages are about 2.65% and 0.41%, respectively. The shrinkage occurred fastest within the first 3 hours of mixing for both grouts. Although, gel time of grout A is lower than the grout B, grout A experienced higher post-gel shrinkage than

that of grout B. This implies that grout A undergoes shrinkage over a prolonged period compared to grout B.

### 3.3. Effect of Filler on Shrinkage Properties

Inclusion of coarse filler in grout A system in the ratio of 1:1 by weight considerably reduces the volumetric shrinkage. This also results in prolonged gel time for grout B. It implies that grout A exhibits faster curing at the early stage of mixing. It is evident that filled system undergone less shrinkage. The 1 day shrinkage of grout A is about 3 times higher than that without aggregate filler. This ratio between shrinkage of the two grouts is approximately maintained up to 28 days, where shrinkage of grout A is about 2.5 times higher than that of grout B. The reduced shrinkage of grout B compared to A is due to the inclusion of aggregate filler that occupied approximately 44% of its volume (50% by weight). By weight, approximately 37% of grout A is epoxy resin and hardener, which reduces to half when filler is added in the case of grout B. The inclusion of inert coarse filler along with reduction of total resin and hardener content has also resulted in reduction of shrinkable content in grout B. The post-gel shrinkage is also found to be higher in grout A than grout B. This also indicates that grout A goes under higher volumetric shrinkage even after gel time. The post-gel shrinkages of grout A and B reduce to about 96% and 37%, respectively, of their total 28 day shrinkages. Hence, the shrinkage is influenced by inclusion of filler and has considerable effect on the grout system.

### 3.4. Dynamic Mechanical Properties

Figures 6, 7 and 8 illustrate the DMA properties of the grouts. Figure 6 shows the change in the storage modulus according to the changes in the temperature. It can be seen that the transition after the glass state region of grout B occurs slightly earlier than that of grout A. However, the transition temperature range is narrower in grout A than that of grout B. Transition peak temperatures for loss moduli for the grouts are comparable as seen from Figure 7.  $\tan \delta$  signals of Figure 8 suggest a higher glass transition peak in grout B than that of grout A. The glass transition temperatures of the grouts are found to be about 83°C and 90°C for grout A and B, respectively. Hence, inclusion of coarse filler in grout A results in increased thermal applicability for the grout system investigated in this study.

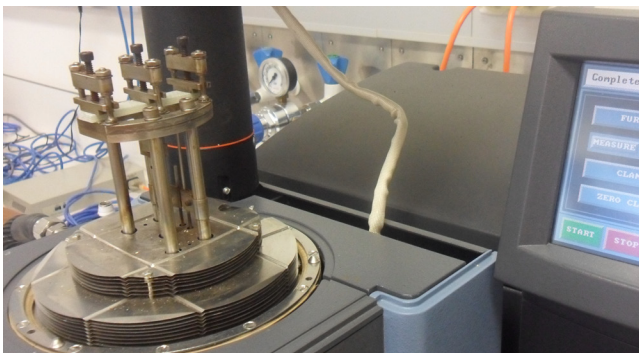


**Figure 4.** DMA specimens mounted on three point bending fixture.

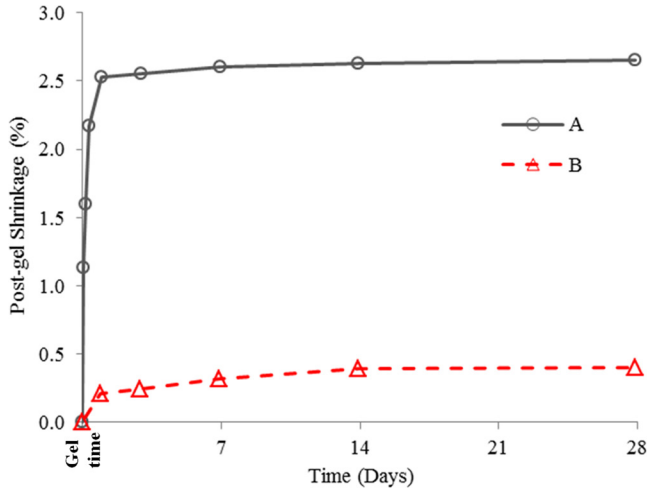


Figure 5. Post-gel shrinkages of grouts.

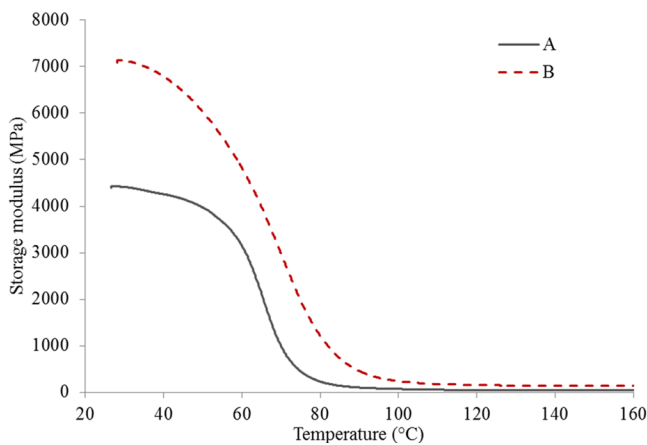


Figure 6. Storage moduli for the grouts.

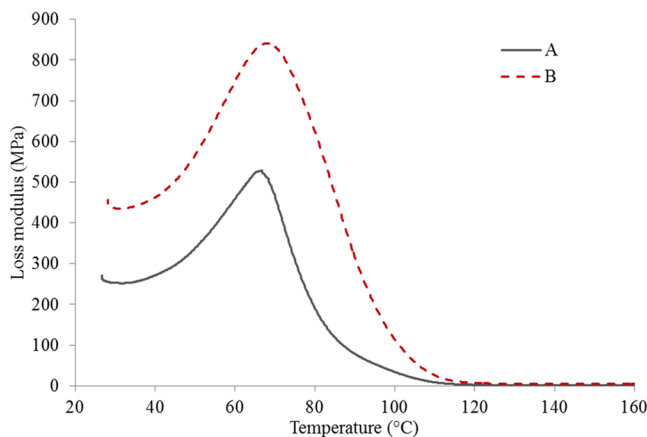


Figure 7. Loss moduli for the grouts.

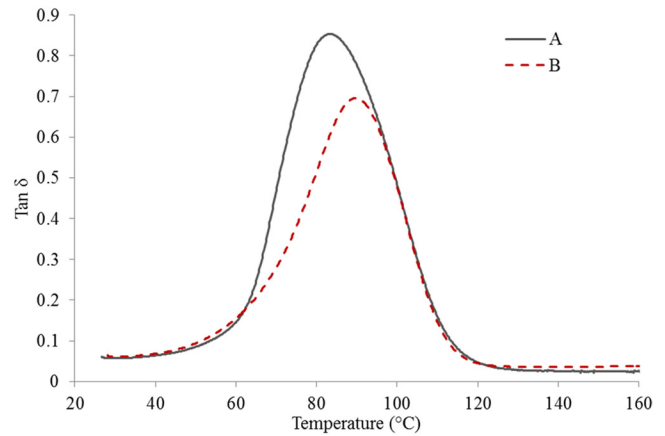


Figure 8.  $\tan \delta$  signals for the grouts.

#### 4. CONCLUSIONS

A fine-filled grout system was modified using a coarse filler. Shrinkage properties of the epoxy grouts were investigated over 28 day period. Dynamic mechanical analysis was also carried out prior to 7 days of curing. The following conclusions can be drawn based on the results of the study:

- Most of the shrinkage occurs within the first 24 hours of mixing. The grouts achieve more than 80% and 90% of the 28-day shrinkage, over 1 and 7 days, respectively. The maximum volumetric shrinkages exhibited by Grouts A and B over 28 day period are about 2.77% and 1.09%, respectively.
- Grout A exhibits shorter gel time than that of grout B. Grout B underwent less volumetric shrinkage after gel time than that of grout A. The filled system exhibits higher reduction in post-gel shrinkage with a value more than 60% when compared to overall shrinkage on 28 days.
- The inclusion of coarse filler at a ratio of 1:1 by weight results in the reduction of the volumetric shrinkage by about 2.5 times over 28 days. The post-gel shrinkage is also reduced due to slow curing rate indicated by longer gel time.
- Grout A exhibits glass transition temperature of 83°C. Filled grout B shows higher thermal applicability than that of grout A by about 8% than that of grout A.

The filled grout experienced less shrinkage and improved glass transition temperature. Hence, it is expected to improve the post cure stress and crack development. However, in case of a mass grout pour in a confined space, gel time can be shorter. Hence, the effect of thickness and surrounding confinement behaviour of epoxy grouts should be considered for in-situ structural applications.

## ACKNOWLEDGEMENT

This study was undertaken as part of the Cooperative Research Centre for Advanced Composite Structures (CRC-ACS) research program, under P1.3 Deepwater Composites, established and supported under the Australian Government's Cooperative Research Centres Program. Support and technical feedback from Mr Bruce Cartwright of Pacific ESI and Dr Luke Djukic of Advanced Composite Structures Australia during this study is also acknowledged.

## REFERENCES

- [1] Kneuer R. L. and Meyers M., "Strengths and limitations of epoxy grouts," *Concrete International March*, 54–56 (1991).
- [2] Prolongo S. G., del Rosario G. and Ure-a A., "Comparative study on the adhesive properties of different epoxy resins," *Int. J. Adhes. Adhes.* 26(3), 125–132 (2006). <http://dx.doi.org/10.1016/j.ijadh.2005.02.004>
- [3] Mendis P., "Commercial applications and property requirements for epoxies in construction," *ACI Special Publication SP(89-7)*, 127–140 (1985).
- [4] Chekanov Y. A., Korotkov V. N., Rozenberg B. A., Dhavadyan E. A. and Bogdanova L. M., "Cure shrinkage defects in epoxy resins," *Polymer* 36(10), 2013–2017 (1995). [http://dx.doi.org/10.1016/0032-3861\(95\)91446-E](http://dx.doi.org/10.1016/0032-3861(95)91446-E)
- [5] Wang X., Wang C., Jia Y., Luo L. and Li P., "Cure-volume-temperature relationships of epoxy resin and graphite/epoxy composites," *Polymer* 53(19), 4152–4156 (2012). <http://dx.doi.org/10.1016/j.polymer.2012.07.039>
- [6] Haider M., Hubert P. and Lessard L., "Cure shrinkage characterization and modeling of a polyester resin containing low profile additives," *Composites Part A: Applied Science and Manufacturing* 38(3), 994–1009 (2007). <http://dx.doi.org/10.1016/j.compositesa.2006.06.020>
- [7] Hossain M., Possart G. and Steinmann P., "A small-strain model to simulate the curing of thermosets," *Computational Mechanics* 43(6), 769–779 (2009). <http://dx.doi.org/10.1007/s00466-008-0344-5>
- [8] Antonucci V., Cusano A., Giordano M., Nasser J. and Nicolais L., "Cure-induced residual strain build-up in a thermoset resin," *Composites Part A: Applied Science and Manufacturing* 37(4), 592–601 (2006). <http://dx.doi.org/10.1016/j.compositesa.2005.05.016>
- [9] Presser M. and Geiss P. L., "Experimental investigation of the influence of residual stress due to curing shrinkage on the interphase formation in adhesively bonded joints," *Procedia Engineering* 10(0), 2743–2748 (2011). <http://dx.doi.org/10.1016/j.proeng.2011.04.457>
- [10] Zarrelli M., Skordos A. A. and Partridge I. K., "Investigation of cure induced shrinkage in unreinforced epoxy resin," *Plastics, Rubber and Composites Processing and Applications* 31(9), 377–384 (2002). <http://dx.doi.org/10.1179/14658010225006350>
- [11] Yu Y., Ashcroft I. A. and Swallowe G., "An experimental investigation of residual stresses in an epoxy–steel laminate," *International Journal of Adhesion and Adhesives* 26(7), 511–519 (2006). <http://dx.doi.org/10.1016/j.ijadh.2005.07.006>
- [12] Magniez K., Vijayan A. and Finn N., "Apparent volumetric shrinkage study of RTM6 resin during the curing process and its effect on the residual stresses in a composite," *Polymer Engineering & Science* 52(2), 346–351 (2012). <http://dx.doi.org/10.1002/pen.22088>
- [13] Lee C-H, Park J-J., "The properties of DSC and DMA for epoxy nano-and-micro mixture composites," *Trans Electr Electron Mater* 11, 69–72 (2010). <http://dx.doi.org/10.4313/TEEM.2010.11.2.069>
- [14] Hamerton I., "Recent developments in epoxy resins," *RAPRA Review Reports* 8(7), Report 91, (1996).
- [15] Boyard N., Vayer M., Sinturel C., Erre R. and Delaunay D., "Modeling PVTX diagrams: Application to various blends based on unsaturated polyester—Influence of thermoplastic additive, fillers, and reinforcements," *Journal of Applied Polymer Science* 92(5), 2976–2988 (2004). <http://dx.doi.org/10.1002/app.20312>
- [16] Nawab Y., Shahid S., Boyard N. and Jacquemin F., "Chemical shrinkage characterization techniques for thermoset resins and associated composites," *Journal of Materials Science (April)*, 1–23 (2013).
- [17] ISO 3521: 1997(E), "Plastics—Unsaturated polyesters and epoxy—Determination of overall volume shrinkage," International Organization for Standardization (1997).
- [18] ASTM D2471, "Standard Test Method for Gel Time and Peak Exothermic Temperature of Reacting Thermosetting Resins," ASTM committee (1999).
- [19] Wolfrum J., Ehrenstein G., and Avondet M., "Dynamical mechanical thermo analysis of high performance composites-influences and problems," *J Compos Mater* 34, 1788–1807 (2000). <http://dx.doi.org/10.1106/PBYT-XY01-HLVP-09UY>
- [20] Khoun L. and Hubert P., "Characterizing the cure shrinkage of an epoxy resin in situ," *Plastics Research Online*, <<http://www.4spepro.org/pdf/002583/002583.pdf>> (18 October 2012).
- [21] Shah D. U. and Schubel P. J., "Evaluation of cure shrinkage measurement techniques for thermosetting resins," *Polymer Testing* 29(6), 629–639 (2010). <http://dx.doi.org/10.1016/j.polymertesting.2010.05.001>
- [22] Schoch Jr K. F., Panackal P. A. and Frank P. P., "Real-time measurement of resin shrinkage during cure," *Thermochimica Acta* 417(1), 115–118 (2004). <http://dx.doi.org/10.1016/j.tca.2003.12.027>



## Structures of Hybrids of DNA and Carbon Nanotubes Observed by Atomic Force Microscopy in Air and in Liquids

KAZUO UMEMURA\*, TAKUYA HAYASHIDA, DAISUKE NII, YUUKI YAMAGUCHI and TAKUYA KAWASHIMA

*Department of Physics, Graduate School of Science, Tokyo University of Science, 1-3 Kagurazaka, Shinjuku-ku, Tokyo 162-8601*

### KEYWORDS

single-walled carbon nanotube  
DNA  
atomic force microscopy

### ABSTRACT

We investigated single-walled carbon nanotubes (SWNT) and DNA-SWNT hybrids by atomic force microscopy (AFM). From the AFM observation of several different types of SWNTs and DNA-SWNT hybrids in air, we found several specific differences in morphology among the samples. First, longer SWNT molecules were observed when the SWNT was dispersed using a bath type sonicator. When a probe type sonicator was employed, much shorter SWNT molecules were observed in all of our experiments using several different SWNTs. The result suggests that effects of the type of sonicator on SWNT length were significant in contrast to that of the type of SWNTs. Second, SWNT functionalized with polyethyleneglycol (PEG SWNT), amino group (NH<sub>2</sub> SWNT), and carboxyl group (COOH SWNT) individually showed specific features in AFM images. Although NH<sub>2</sub> SWNT is typically soluble in organic solvents, uniform distribution was observed when DNA molecules were mixed with NH<sub>2</sub> SWNT. Finally, we observed DNA-SWNT hybrids by AFM in liquids for the first time. DNA-SWNT hybrids were significantly swollen in the aqueous solution even though the sample was dried once. This is helpful information for considering biological applications of the DNA-SWNT hybrids.

© 2014 DEStech Publications, Inc. All rights reserved.

### 1. INTRODUCTION

Techniques of attaching biomolecules onto carbon nanotubes (CNT) surfaces, especially onto single-walled carbon nanotubes (SWNT) have been developed by many research groups since 2003 [1–3]. This technique was originally developed from the viewpoint of material sciences in order to dissolve CNTs in aqueous solutions. After that, interest of biological applications such as nanobiodevices using hybrids of biomolecules and CNTs has been recognized. On the other hand, one of the recent progresses in nanocarbon technology is synthesis of variously functionalized SWNTs [4]. Some of the chemically modified SWNTs can be solved in water without attaching surfactants or biomolecules. The

compounds may be also useful for biological applications of SWNT. Although knowledge of such functionalized SWNTs and hybrids of biomolecules and SWNT has been accumulated, sample preparation conditions and observation conditions were widely in each paper. For example, conditions of hybridization of biomolecules and SWNT are not uniform among the previous papers although the results of hybridization are strongly affected by the conditions, especially by the sonication conditions. Further, observation of the functionalized SWNT and hybrids of SWNT by atomic force microscopy (AFM) have been carried out in air or dried conditions although nanobiodevices are usually worked in aqueous solutions.

In this work, we focused on AFM observation of several types of functionalized SWNTs in air as the first experiments. By this experiment, specific features of each functionalized

\*Corresponding author. Email: [meicun2006@163.com](mailto:meicun2006@163.com)

SWNT on a substrate such as distribution on the substrate can be visualized. Second, we observed hybrids of ssDNA/dsDNA and SWNT in liquids for the first time. Topological differences of the hybrids in air and in TE buffer can be recognized as flexibility of biomolecules on the SWNT.

## 2. EXPERIMENTATION

Single-stranded DNA consisting of 30-mers of thymine ( $T_{30}$ ) was obtained from Life Technologies Japan Ltd. (Tokyo, Japan), and double-stranded DNA from salmon testes (D1626) was obtained from Sigma-Aldrich Co. (MO, USA). SWNTs grown through a high-pressure carbon monoxide decomposition process (bare SWNT) were purchased from Unidym, Inc. (CA, USA). SWNT functionalized with  $NH_2$  group ( $NH_2$  SWNT,  $NH_2$  Single Walled/Double Walled Nanotubes-SW/DWCNTs 99 wt%) was purchased from CheapTubes Inc. (Brattleboro, VT). SWNT functionalized with COOH group (COOH SWNT, Nink-1100) was bought from Nanolab Inc. (Waltham, MA). SWNT functionalized with polyethyleneglycol (PEG SWNT, P7-SWNT) was obtained from Carbon Solutions, Inc., (Riverside, CA).

Hybrids of ssDNA/dsDNA and bare SWNT were prepared as follows. Mixture of DNA and SWNT in TE buffer solution was sonicated (VCX 130, Sonics & Materials, Inc., CT) on ice for 90 min. The sample was then centrifuged at 18500 g for 6 h (himac CR15D, Hitachi Koki Co., Ltd., Tokyo, Japan), and finally the supernatant was collected. PEG SWNT was sonicated by a bath type sonicator (LEO-80, Steady Ultrasonic Sdn. Bhd., Selangor, Malaysia) in TE buffer solution.  $NH_2$  SWNT was mixed with ssDNA in the TE buffer solution, and then sonicated with the bath type sonicator. COOH SWNT solution was used after dilution with pure water.

For AFM observation, the diluted samples were deposited onto a mica substrate that had been treated with 3-aminopropyltriethoxysilane (APTES). The sample was incubated for 10 min, rinsed with ultrapure water, and finally dried in a desiccator. JSPM-5200 Scanning Probe Microscope (JEOL Ltd., Tokyo, Japan) and MFP-3D (Asylum Research, Santa Barbara, CA) were performed with a Si cantilever under nitrogen-injected air, and with a  $Si_3N_4$  cantilever under the TE buffer. The height distribution of the hybrids was established from cross sections of the AFM images.

## 3. RESULTS AND DISCUSSIONS

Figure 1 shows AFM images of various SWNT molecules and DNA-SWNT hybrids that were observed in air. Bare SWNT molecules showed thick rods that had varied heights [Figure 1(a)]. It suggests the SWNT molecules tended to form bundles although it could be dispersed in the organic solvent (1,2-dichloroethane (DCE)). Contrarily, when the same SWNT molecules were hybridized with ssDNA or

dsDNA as previously reported, rather uniform dispersion was obtained in an aqueous solution.

As to the length of the SWNT molecules, longer SWNT molecules ( $>1 \mu m$ ) were observed only in Figure 1(a) among Figure 1(a) to 1(c) although the same SWNT was used in the experiments. The major factor to affect length of the SWNT molecules is probably sonication condition. In the case of Figure 1(a), the bath type sonicator was employed because the solvent was DCE. When the sample was sonicated by the probe type sonicator, the solvent was easily evaporated. In the case of Figure 1(b) and 1(c), the probe type sonicator was used. Because the power of the probe type sonicator is stronger than that of the bath type sonicator, SWNT molecules were probably cut during the sonication. It suggests that DNA molecules were also damaged by the process.

Variouly functionalized SWNTs were characterized in Figure 1(d) to 1(f). PEG SWNT and COOH SWNT were well distributed on an AP-mica substrate without DNA molecules. In these samples, Figure 1(d) and 1(e) showed longer SWNT molecules ( $>1 \mu m$ ). Although PEG SWNT is basically water-soluble compound, in order to obtain good dispersion, the PEG SWNT was sonicated by the bath type sonicator without mixing DNA molecules. As a result, long PEG SWNT molecules were distributed on an AP-mica surface without attaching DNA molecules. In the case of  $NH_2$  SWNT, it is known that the compound is soluble to organic solvents. For this reason,  $NH_2$  SWNT was sonicated with DNA molecules using the bath type sonicator when it was solved in the TE buffer solution. In the case of COOH SWNT, dispersed solution was bought from the manufacture, so it is out of this discussion. In all the cases examined in Figure 1, the samples that were treated by the bath type sonicator showed longer structures. For biological applications, it is obvious that sonication-free procedure is suitable for keeping structures of biomolecules. In our previous paper, we proposed the sonication-free procedure using PEG SWNT [5]. Comparison of several types of SWNTs suggested that the selection of PEG SWNT is one of the reasonable ways.

Discussion of diameters of SWNT and DNA-SWNT hybrids is not simple in general because the SWNTs show wide distribution of diameters [6]. However, the functionalized SWNT molecules that were observed in this study showed significant differences in diameters. COOH SWNT was typically larger than 5 nm in heights from the cross section of AFM images. In the case of PEG SWNT and DNA- $NH_2$  SWNT, the typical heights were 2 to 3 nm. On the other hand, bare SWNT was less than 2 nm even with DNA molecules when it was mono-dispersed. In 1999, Balavoine *et al.* demonstrated crystallization of proteins on multi-walled CNT (MWNT) [7]. They revealed that there is the suitable CNT diameter to form helical structures of protein molecules on the CNT. To examine various diameters, they employed

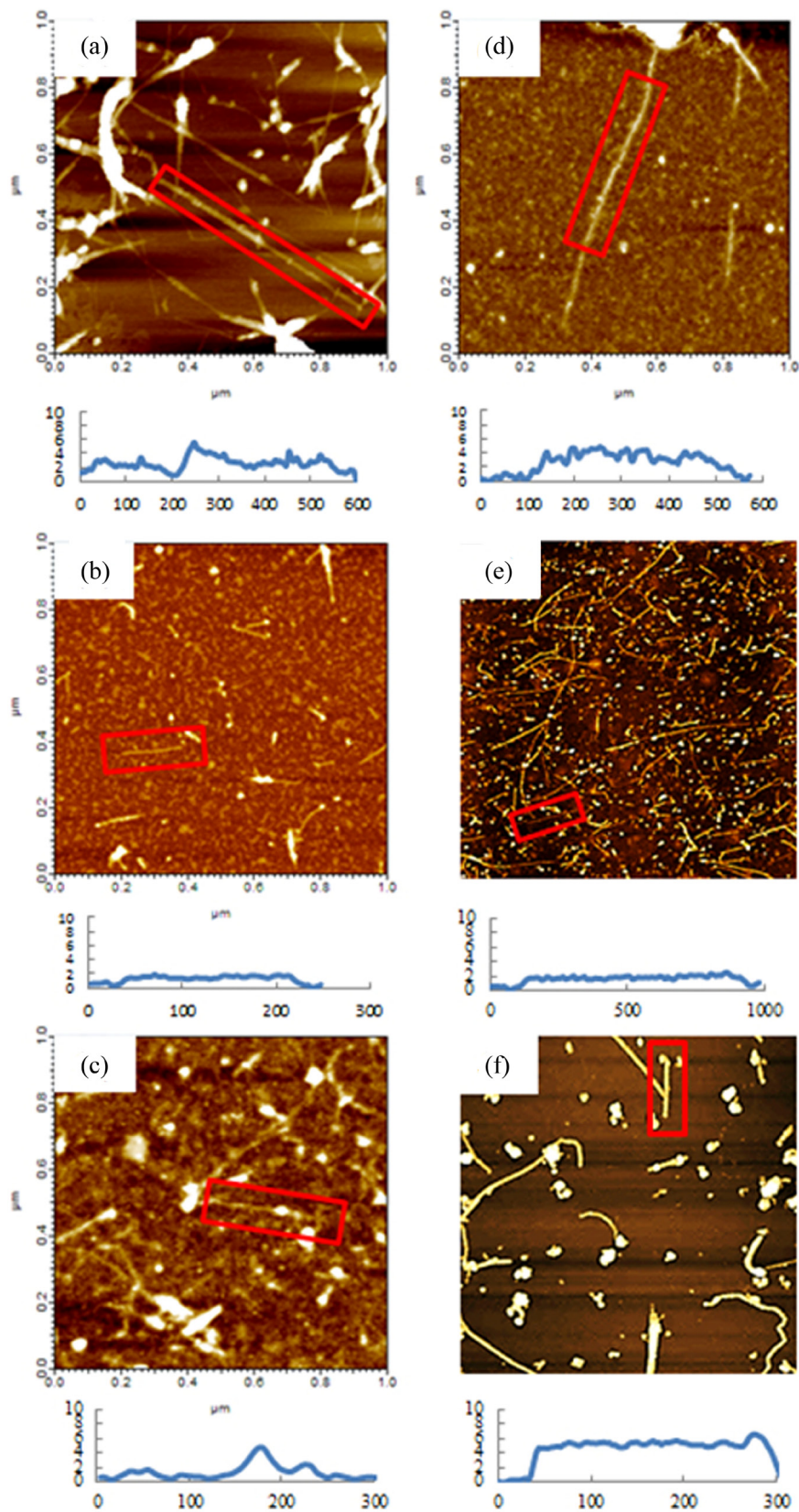


**Figure 1.** AFM images SWNT and DNA-SWNT hybrids observed in air: (a) Bare SWNT; (b) ssDNA-SWNT hybrids; (c) dsDNA-SWNT hybrids; (d) PEG SWNT; (e) ssDNA-NH<sub>2</sub> SWNT hybrids; (f) COOH SWNT. Bottom graphs are cross section of a SWNT or a DNA-SWNT hybrid enclosed by a red square. Scan size are 1  $\mu\text{m} \times 1 \mu\text{m}$  ((a) to (d)), 3  $\mu\text{m} \times 3 \mu\text{m}$  (e), and 1.5  $\mu\text{m} \times 1.5 \mu\text{m}$  (f).

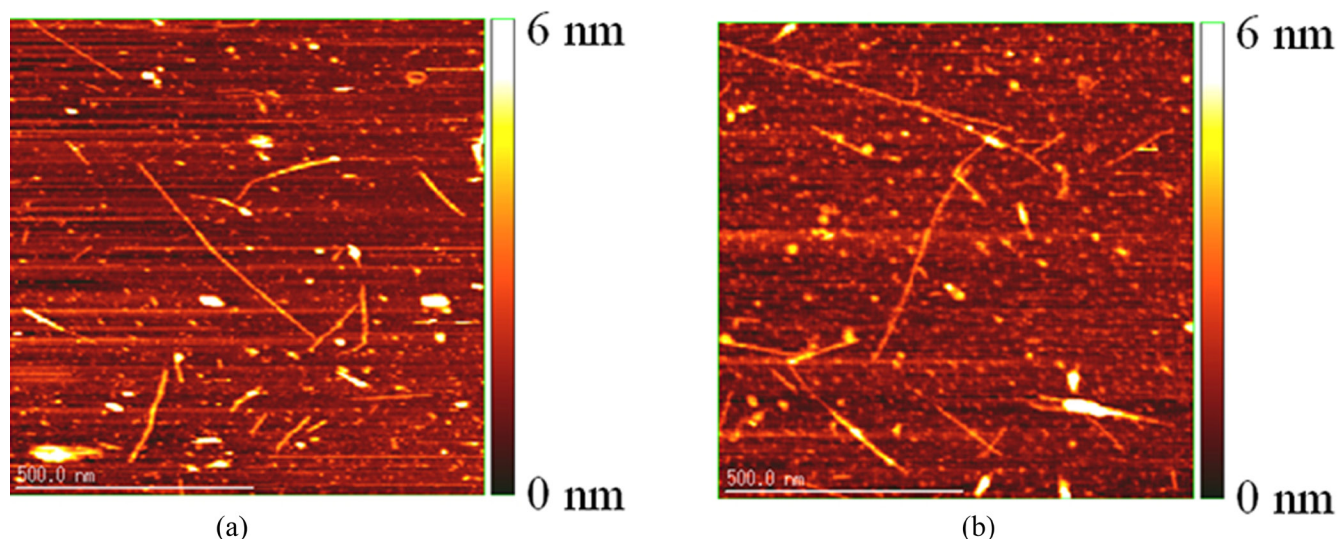


**Figure 2.** AFM images of DNA-SWNT hybrids observed in TE buffer solution. (a) ssDNA-SWNT hybrids. (b) dsDNA-SWNT hybrids. Scan size is  $1\ \mu\text{m} \times 1\ \mu\text{m}$ .

MWNT not SWNT. In this sense, variously different diameters of the functionalized SWNT molecules look attractive for crystallization study of proteins.

Figure 2(a) and 2(b) show AFM images of ssDNA-SWNT and dsDNA images obtained in the TE buffer solution, respectively. Rod-like features were observed clearly in the wet condition. To our knowledge, this is the first demonstration of the fluid AFM of DNA-SWNTs. In liquids, the typical heights of the ssDNA-SWNT and dsDNA-SWNT were both larger than 2 nm. The value is significantly larger than that in air. It suggests that DNA molecules adsorbed on the SWNT surface were swollen in liquids although the sample was dried once. Detailed analysis of AFM images in liquids is in progress, it will be reported in near future.

#### 4. CONCLUSIONS

We investigated several different types of SWNTs including chemically functionalized SWNTs by AFM in air and in liquid. Comparison in air gave detailed information of each SWNT and DNA-SWNT hybrid. Further, AFM images in liquid clearly indicated that the DNA molecules were swollen in liquid. We believe that this information is useful to develop nanobiodevices using DNA and SWNTs.

#### ACKNOWLEDGEMENTS

This work was supported by a Grant-in-Aid for Scientific Research (23540479) of the Japan Society for the Promotion

of Science (JSPS). The authors thank the Division of Nano-carbon Research, Tokyo University of Science, for valuable discussions.

#### REFERENCES

- [1] Huang, W., Taylor, S., Fu, K., Lin, Y., Zhang, D., Hanks, T. W., Rao, A. M., Sun, Y. -P., "Attaching proteins to carbon nanotubes via diimide-activated amidation," *Nano Lett.* 2(4), 311–314(2002). <http://dx.doi.org/10.1021/nl010095i>
- [2] Karajanagi, S. S., Yang, H., Asuri, P., Sellitto, E., Dordick, J. S., Kane, R. S., "Protein-assisted Solubilization of Single-Walled Carbon Nanotubes," *Langmuir* 22(4), 1392–1395(2006). <http://dx.doi.org/10.1021/la0528201>, PMID:16460050
- [3] Kojima, M., Chiba, T., Niishima, J., Higashi, T., Fukuda, T., Nakajima, Y., Kurosu, S., Hanajiri, T., Ishii, K., Maekawa, T., Inoue, A., "Dispersion of single-walled carbon nanotubes modified with poly-l-tyrosine in water," *Nanoscale Res. Lett.* 6, 128 (2011). <http://dx.doi.org/10.1186/1556-276X-6-128>, PMID:21711636 PMID:PMC3211174
- [4] Zhao, B., Hu, H., Yu, A., Perea, D., Haddon Jones, R. C., Director, C. J., "Synthesis and Characterization of Water Soluble Single-Walled Carbon Nanotube Graft Copolymers," *JACS* 127, 8197–8203(2005). <http://dx.doi.org/10.1021/ja042924i>, PMID:15926849
- [5] Nii, D., Hayashida, T., Umemura K., "Controlling the adsorption and desorption of double-stranded DNA on functionalized carbon nanotube surface," *Colloids Surf. B* 106, 234–239(2013). <http://dx.doi.org/10.1016/j.colsurfb.2013.01.054>, PMID:23434717
- [6] Hayashida, T., Umemura, K., "Surface morphology of hybrids of double-stranded DNA and single-walled carbon nanotubes studied by atomic force microscopy," *Colloids Surf. B* 101, 49–54(2013). <http://dx.doi.org/10.1016/j.colsurfb.2012.06.018>, PMID:22796771
- [7] Balavoine, F., Schultz, P., Richard, C., Mallouh, V., Ebbesen, T. W., Mioskowski C., "Helical Crystallization of Proteins on Carbon Nanotubes: A First Step towards the Development of New Biosensors," *Angew. Chem. Int. Ed.* 1999, 38, No.13–14, 1912–1915(1999).